



A University of Sussex PhD thesis

Available online via Sussex Research Online:

<http://sro.sussex.ac.uk/>

This thesis is protected by copyright which belongs to the author.

This thesis cannot be reproduced or quoted extensively from without first obtaining permission in writing from the Author

The content must not be changed in any way or sold commercially in any format or medium without the formal permission of the Author

When referring to this work, full bibliographic details including the author, title, awarding institution and date of the thesis must be given

Please visit Sussex Research Online for more information and further details



**The Formation and Evolution of Dust in
Semi-Analytic Models of Galaxy
Formation**

Scott Jonathan Clay

Submitted for the degree of Doctor of Philosophy

University of Sussex

May 2017

UNIVERSITY OF SUSSEX

SCOTT JONATHAN CLAY, DOCTOR OF PHILOSOPHY

THE FORMATION AND EVOLUTION OF DUST IN SEMI-ANALYTIC MODELS OF
GALAXY FORMATIONSUMMARY

The formation and evolution of galaxies is an interesting subject to study because it incorporates astrophysics from all scales, from the initial perturbations in the early universe creating the large scale structures that produce galaxies, right down to the evolution of stellar populations and their manipulation of the host galaxy. Simulations of galaxy formation allow us to test the various physical recipes against that which is observed in order to build a true and proper picture of what is happening in the real universe.

L-Galaxies is a semi-analytic model of galaxy formation built on top of the merger trees from the Millennium dark matter simulation, and is constrained to match certain key observations at low redshift by applying a Monte Carlo Markov Chain (MCMC) method to constrain the free parameters. In using the model to make high redshift predictions of the stellar mass function, UV luminosity function and star formation rate distribution function we found that the model starts to deviate from observational constraints at the highest redshifts, particularly in high mass galaxies. In the case of the UV luminosity function, this is because the current dust model is calibrated at low redshift and lacks sophistication in that it only depends on the cold gas mass and the density of metals.

To improve on this we implement a physically motivated dust model that traces the formation of dust from stellar sources, such as in the stellar winds of AGB stars and in the supernovae remnants of massive stars, the growth of dust inside molecular clouds, and the destruction of dust due to supernovae explosions. The model is fully integrated into L-Galaxies such that the evolution of dust is included in all the recipes relevant to the formation and evolution of galaxies, including: star formation; radiative feedback; cooling and reheating; and both major and minor mergers.

Our results show a good fit to observations of the dust mass in galaxies both in the local universe and out to high redshift and we note a similar conclusion as in the literature that dust growth inside molecular clouds is not only necessary but the dominant source of the dust mass in these galaxies. However, stellar sources of dust can not be neglected as molecular clouds must first be seeded by dust grains in order for accretion to occur. This could be important in the very early universe, perhaps for the first galaxies that will hopefully be observed by JWST in the future, because these galaxies may not have had sufficient time to seed their molecular clouds and as such the dust produced by these stellar sources would be important for calculating the galaxies true observed luminosity.

We finish by discussing the limitations of the model and discuss areas for possible improvement as well as the next steps in using this to better predict the luminosity of galaxies in future models.

Acknowledgements

What a long journey this has been! I would like to start by thanking my two supervisors, Peter Thomas and Stephen Wilkins. They have both gone far beyond what anyone expects of a supervisor and I owe them both a debt of gratitude. Without them, this thesis would very much not exist. I would also like to thank my two main collaborators, Bruno Henriques and Rob Yates, for answering any stupid questions I've had over the years, as well as making my research environment a much more fun and enjoyable place to work. Thank you also to Simon White and the Max Planck Institute for Astrophysics for hosting me for several months in 2015, where much of the foundations for the latter part of this thesis were laid down. Finally, thanks to both the University of Sussex, and the Science and Technologies Facilities Council (STFC) for hosting me and of course for funding me during my PhD.

I would be remiss if I didn't also mention the people responsible for where I am today. It was my high school physics teacher, Laurence Wilkinson, and his tolerance for my non-stop questions on space (when I really should have been doing class work) that gave me that initial interest in astronomy. I would like to also thank the academic staff at the University of Leeds, particularly Melvin Hoare and Stuart Lumsden, for nurturing me during my undergraduate studies. And of course, my family, whom provided emotional (and economical!) support throughout my entire life. Yorkshire would have felt so much further away had it not been for the care packages from my Mum, and the rugby banter texts from my Dad and brother.

I have had an amazing time in Brighton, and I will remember my time here as some of the best years of my life. Craig Perl, you were the first person I met on my very first night here. We argued about how the beer prices seemed expensive from my northern point of view, and cheap from your London background. Thanks for all the Sunday lunches. David Sullivan, I think I've shared too much with you. But on the flip side, keeping you around seems to have transferred all my bad luck to you, so thanks for that. I came to Brighton with four brothers, but I leave with six. I would also like to mention some of the other people I've met over the years here, we've had a lot of fun! In roughly chronological order:

Tim, Katy, Alice, Mikey, Aaron, Mark, Heather, Steph, Joe T, the other Joe T, Rob H, Dave T, Dani, Rob S, Caroline, Daire, Helen, Joanne and Andrea!

Equally as important to me are all the people in the Astronomy Centre, who have had to put up with me on a daily basis for almost four years, and they deserve recognition for that. Thanks to Benoît, Dániel, Hannah, Steven and Azizah for all the Friday nights in the pub (or Revenge). We had many laughs (mainly at Dániel's dancing), and many more beers! A special mention for Luciá, one of the most kindhearted people I've had the good pleasure of knowing and someone who looked after me for the better part of two years. I can't mention Luciá without a shout out to her sister, Cuchi, a girl who could always put a smile on my face! Also thanks to our resident undergraduate, Jessie, who sat with me in my office while I put the finishing touches on this thesis and helped to preserve my sanity (even if I did have to buy her friendship with chocolate buttons). There's too many stories to tell, but I'd like to also give a mention to the following people, in roughly chronological order: Boyd, Mateja, Will, Leon, Phil, Pete, Charlotte, Donough, Tik, Antonio, Ze, Alex, Ridwan, Micheala, Chris, Ciarian, Pippa and Sunynana.

And last but certainly not least, thank you to my viva examiners, Carlton Baugh and Seb Oliver. You both settled me in to the viva gently and I ended up finding our discussions both enlightening and enjoyable. Your comments helped to improve the final version of this thesis.

“They paint the world full of shadows... and then tell their children to stay close to the light. Their light. Their reasons, their judgments. Because in the darkness, there be dragons. But it isn’t true. We can prove that it isn’t true. In the dark, there is discovery, there is possibility, there is freedom in the dark once someone has illuminated it. And who has been so close to doing it as we are right now?”

Captain James Flint (Black Sails)

Contents

List of Tables	xi
List of Figures	xx
I Introduction	1
1 Introduction	2
1.1 Simulations of galaxy formation	5
1.2 Semi-Analytics	6
1.2.1 Thesis outline	8
2 Overview of Physics	9
2.1 L-GALAXIES	9
2.1.1 Millennium simulations	11
2.2 Infall and cooling	12
2.3 Star formation	14
2.3.1 Quiescent Star Formation	14
2.3.2 Merger Driven Star Formation	15
2.3.3 Star formation histories	15
2.4 Chemical enrichment	16
2.4.1 Stellar Lifetimes	17
2.4.2 Stellar Yields	17
2.5 Feedback	20
2.5.1 Reionization	20
2.5.2 Supernovae	21
2.5.3 AGN	22
2.6 Reintegration	24

2.7	Mergers	25
2.7.1	Bulge Formation	26
2.8	Calculating Observables	27
2.8.1	IMF	28
2.8.2	Stellar Population Synthesis	28
2.8.3	Dust Extinction	29
2.9	MCMC Parameterisation	31
II Exploring the High-Redshift Universe with the L-Galaxies Semi-Analytic Model		34
3	High-redshift predictions	35
3.1	Millennium vs. Millennium II	35
3.2	Star formation	36
3.3	Stellar mass	37
3.4	sSFR - SM relation	40
3.5	Metals	42
3.6	Varying the model of dust extinction	42
3.7	UV Luminosity	44
3.8	Intrinsic UV continuum slope	48
3.8.1	Redshift	49
3.8.2	Star Formation Rate	49
3.8.3	Stellar Mass	51
3.9	Evolution of high-redshift quantities	52
3.10	Conclusions	54
III Detailed Dust Modelling with the L-Galaxies Semi-Analytic Model		56
4	The Physics of Detailed Dust Modelling	57
4.1	Introduction	57
4.2	Stellar sources of dust production	62
4.2.1	AGB yields	62
4.2.2	Supernovae yields	63
4.3	Dust destruction	64

4.4	Dust growth	64
4.5	Converting observations into physical quantities	68
5	The testing and implementation of a physically motivated dust model	71
5.1	General considerations	71
5.2	Other changes to the model	73
5.3	Main Equation	74
5.4	Stellar Yields	75
5.4.1	Supernovae	77
5.5	Dust growth	78
5.6	Dust destruction	80
5.7	Changes to existing functions in L-GALAXIES	81
5.8	A simple test model	82
5.8.1	Dust growth	83
5.9	Dust destruction	85
5.9.1	Additional test: Dust growth and destruction in a steady state	86
5.10	Testing the model	87
5.10.1	Variation in observations	88
5.10.2	Convergence of MR and MRII	89
5.11	Different production mechanisms	91
5.12	Varying model parameters	94
5.12.1	Varying the rate of grain growth in molecular clouds	94
5.12.2	Varying the mass of dust destroyed	96
5.12.3	Varying dust growth and destruction at higher redshift	99
5.13	Conclusion	99
6	The dust properties of galaxies in the L-GALAXIES SAM	103
6.1	Stellar-Dust Mass relation	103
6.2	Dust to gas and dust to metal ratios	104
6.2.1	Dust to gas ratios	104
6.2.2	Dust to metal ratios	106
6.3	Dust formation rates	110
6.4	Evolution	113
6.5	Dust mass function	115
6.6	Comparison with other work	117

6.7	The first galaxies	117
6.8	Conclusions	119
IV	Conclusions	122
7	Conclusions	123
7.1	Future Work	125
	Bibliography	127

List of Tables

2.1	The free parameters that are constrained in the model using MCMC.	32
5.1	This table describes the different dust species considered in this work, and the average mass by element of each dust species. Where we have a dust species mass, such as from the low mass dust return tables, we then convert this to its individual elements based on the mass breakdown listed here. . .	74
5.2	The conversion efficiencies used for the production of dust grains in supernovae remnants based on the mass return of key metals.	78

List of Figures

- 2.1 A schematic showing the main physical processes that occur inside the model inside each galaxy at every time step. Solid lines represent the transfer of mass, and dashed lines the transfer of energy. This schematic was provided by Rob Yates. 11
- 2.2 Stamps of 15 Mpc/h thick slices from the Millennium simulation at a resolution of 500 Mpc/h (left), 125 Mpc/h (centre) and 31.25 Mpc/h (left). Images taken from the Millennium Simulation Project website (<https://wwwmpa.mpa-garching.mpg.de/galform/virgo/millennium/>). 13
- 2.3 Schematic to show the evolution of the first 5 star formation history bins (shown as rows), for an isolated galaxy. The numbers represent the time width of a bin in units of one time step. At every time step in the code (shown as columns), a new bin is activated. Active bins are coloured in this schematic, with grey representing single-width bins, red for double width bins and green for quadruple-width bins. When three or more active bins have the same length, two of the bins are immediately merged, as shown. In the double merge example, two of the single-width bins (grey) are merged into a double-width bin, which makes three, merging two of them together produces the quadruple-width bin. This figure is taken from Yates et al. (2013). 16
- 2.4 The relationship between the initial mass of a star, M_{init} , and its lifetime, τ . The different colours represent the relation for different metallicities. This plot uses the metallicity dependent lifetime tables from Portinari et al. (1998). 18

2.5	Mass released by AGB winds from the Marigo (2001) yield tables (left), type II supernovae from Portinari et al. (1998) yield tables (centre) and type Ia supernovae from Thielemann et al. (2003) yield tables (right). Points indicate the values from the yield tables, and lines the interpolation between those points. Dashed lines show the extrapolation beyond the masses originally modelled. Plots are taken from Yates et al. (2013)	19
2.6	The $M_* - Z_{cold}$ relation for L-GALAXIES at $z=0$, showing the new detailed chemical enrichment model (black lines), the old simple model (red lines), compared against observations of emission line galaxies from SDSS (Yates et al., 2012). Plot taken from Yates et al. (2013).	20
2.7	The role of feedback in modifying the galaxy luminosity function. Figure taken from Silk and Mamon (2012)	21
2.8	A schematic showing the different ‘types’ of galaxies of galaxy considered inside the model. The dark matter halos are also shown by black circles. This figure was provided by Rob Yates.	25
2.9	Predicted stellar mass functions at redshift $z \approx 0$ (top left); $z \approx 1$ (top right); $z \approx 2$ (lower left) and $z \approx 3$ (lower right). Solid black lines show the stellar mass functions predicted by the model. Observations are taken from several surveys; SDSS (Baldry et al., 2008; Li and White, 2009) and GAMA (Baldry et al., 2012) at $z=0$; and Marchesini et al. (2009), Spitzer-COSMOS (Ilbert et al., 2010), NEWFIRM (Marchesini et al., 2010), COSMOS (Domínguez Sánchez et al., 2011), ULTRAVISTA (Muzzin et al., 2013; Ilbert et al., 2013) and ZFOURGE (Tomczak et al., 2014) at higher redshifts.	33
3.1	Predicted stellar mass (left) and UV luminosity functions (right) at redshift $z \approx 4$. The black lines show the predictions from the Millennium (MR) simulation, and the red line shows the predictions from the Millennium-II (MR-II) simulation. The y-axis presents the number density, Φ , in units of $h^3 Mpc^{-3} dex^{-1}$ for the stellar mass function, and units of $h^3 Mpc^{-3} mag^{-1}$ for the luminosity function.	36

- 3.2 Predicted star formation rate distribution functions at redshift $z \approx 4$ (top left); $z \approx 5$ (top right); $z \approx 6$ (lower left) and $z \approx 7$ (lower right). In each instance we use the closest available snapshot from our L-GALAXIES run of $z=3.95, 5.03, 5.82$ and 6.97 respectively. Solid black lines show the star formation rate distribution function predicted by the model. Our $z = 4$ star formation rate distribution function is repeated at higher redshifts as a grey dot-dash line for comparison. Observations are taken from Smit et al. (2012), converted to a Chabrier IMF, and Duncan et al. (2014). 38
- 3.3 Predicted stellar mass functions at redshift $z \approx 4$ (top left); $z \approx 5$ (top right); $z \approx 6$ (lower left) and $z \approx 7$ (lower right). In each instance we use the closest snapshot available to use from our L-GALAXIES run of $z=3.95, 5.03, 5.82$ and 6.97 respectively. Solid black lines show the stellar mass functions predicted by the model. To indicate the possible effect of uncertainties in the observational stellar mass determinations, we also show as a red dot-dash line the stellar mass function convolved with a Gaussian of standard deviation 0.3 dex . Our $z = 4$ stellar mass function is repeated at higher redshifts as a grey dot-dash line for comparison. Observations are taken from González et al. (2011), converted to a Chabrier IMF, and Duncan et al. (2014). 39
- 3.4 Predicted specific star formation rates ($sSFR = SFR/M_*$) at redshift $z \approx 4$ (top left); $z \approx 5$ (top right); $z \approx 6$ (lower left) and $z \approx 7$ (lower right). In each instance we use the closest snapshot available to use from our L-GALAXIES run of $z=3.95, 5.03, 5.82$ and 6.97 respectively. The histogram density plot represents the L-GALAXIES galaxy population, with white representing the highest density, and blue representing the least. The solid line shows the L-GALAXIES median values, and the dashed lines show the 0.16 and 0.84 percentiles. The observations are taken from Salmon et al. (2015), with the points denoting the median value while the error bars reflect the scatter in the observations, rather than the uncertainty in the median. . . . 41
- 3.5 Plot to show the median metallicity of the cold gas (top) and the median metallicity of the stars (bottom), plotted against stellar mass. The coloured lines show the relation for different redshifts in the range $z \in \{0, 1, 2, 3, 4, 5, 6, 7\}$ 43

- 3.6 The UV luminosity function using various different dust extinction models. The dashed line shows the intrinsic luminosity function. The blue line shows a version of the model where we have replaced our model metallicities with observed values. The blue and green lines show variations on the redshift dependence for the dust extinction model currently used by the model. The black points show observational data from a number of sources (Bouwens et al. (2015), Duncan et al. (2014), Finkelstein et al. (2015), Bowler et al. (2015), Bowler et al. (2014)). 45
- 3.7 Predicted rest-frame (1500 \AA) UV luminosity functions at redshift $z \approx 4$ (top left); $z \approx 5$ (top right); $z \approx 6$ (lower left) and $z \approx 7$ (lower right). In each instance we use the closest snapshot available to use from our L-GALAXIES run of $z=3.95, 5.03, 5.82$ and 6.97 respectively. Solid black lines shows the L-GALAXIES prediction for the attenuated UV luminosity function using the dust extinction model outlined in Section 2.8.3. The dashed black line is the L-GALAXIES prediction of the intrinsic UV luminosity function, with no dust model applied. Our $z = 4$ attenuated UV luminosity function is repeated at higher redshifts as a grey dot-dash line for comparison. Observations are taken from Bouwens et al. (2015), Duncan et al. (2014) and Finkelstein et al. (2015), and at high mass from Bowler et al. (2015) ($z = 6$) and Bowler et al. (2014) ($z = 7$). 46
- 3.8 This figure shows the amount of dust attenuation required to move our intrinsic UV luminosity function (the dashed, black lines in Figure 3.7) to match different observational data sets (Bouwens et al., 2015; Duncan et al., 2014; Finkelstein et al., 2015), as a function of unattenuated absolute UV magnitude. The solid, black line shows the attenuation built into the L-GALAXIES model as described in Section 2.8.3. 47

- 3.9 The redshift evolution of the median intrinsic UV continuum slope for model galaxies with $\log_{10}(\text{SFR}/M_{\odot} \text{ yr}^{-1}) > 0.0$ (solid black line) and $\log_{10}(\text{SFR}/M_{\odot} \text{ yr}^{-1}) > 1.0$ (dashed line). The coloured points with error bars show the observational constraints from Meurer et al. (1999), Heinis et al. (2013), Casey et al. (2014), Álvarez-Márquez et al. (2016) and Castellano et al. (2014). Two data points are shown from Smit et al. (2015), the open circle shows the results from photometrically derived redshift values, and the closed circle shows galaxy values with spectroscopically confirmed redshifts. We also compare our results with the GALFORM SAM (Wilkins et al., 2013a) and the MASSIVEBLACKII simulation (Wilkins et al., 2013b). 50
- 3.10 The relationship between the intrinsic UV continuum slope and the star formation rate of galaxies in our model at $z \in \{0.1, 2.0, 6.0\}$. The solid black line shows the median value (as a function of star formation rate) while the dashed lines denote the 16th – 84th centile range. The shaded region shows a 2D histogram representing the number density of galaxies. 51
- 3.11 The relationship between the intrinsic UV continuum slope and the stellar mass of galaxies in our model at $z \in \{0.1, 2.0, 6.0\}$. The solid black line shows the median value (as a function of stellar mass) while the dashed lines denote the 16th – 84th centile range. The shaded region shows a 2D histogram representing the number density of galaxies. 52
- 3.12 Plot to show the evolution of the stellar mass (top left); star formation rate (top right); UV luminosity function (lower left); and specific star formation rate (lower right) in the redshift range $z = 4 - 7$. The lines show the median values for each property at each redshift. In each instance we use the closest snapshot available to use from our L-GALAXIES run of $z=3.95, 5.03, 5.82$ and 6.97 respectively. 53

5.1	Schematic to show how the production of metals and dust is dealt with inside the model. This simple schematic shows the stellar disk component of a galaxy in our model, as well as the cold gas (ISM) component. The ISM is further split into the metal and dust components that we treat separately from one another. The red arrows show the enrichment of metals from the death of stars. The green lines show the enrichment of dust when stars die, as well as dust growth within molecular clouds (converting metals into dust), and grain destruction (converting dust into metals). Also shown is the star formation process, which removes both metals and dust (and cold gas) from the ISM into newly formed stars.	73
5.2	The mass of dust species (silicates, carbon, silicon carbide and iron) returned for a star based on the star's initial mass. The left panel shows the relation for a metallicity of $Z = 0.004$, and the right panel for $Z = 0.02$ ($\sim Z_{\odot}$)	76
5.3	A plot showing how the cold gas, stellar mass, metal mass and dust mass evolve through time in our simple test model.	83
5.4	A simple model testing the implementation of the dust growth equations with the analytic solution.	84
5.5	A simple model testing the implementation of the dust destruction equations with the analytic solution.	85
5.6	A simple model testing the implementation of both the dust growth and destruction equations with the analytic solution.	87
5.7	The stellar-dust mass relation at $z=0$. The black line shows the median result of our model, with the 2D histogram underneath representing individual galaxies. The model was only run on 1/512 of the total Millennium simulation, though on a tree thought to be representative. The observations are shown by coloured points.	88
5.8	The stellar-dust mass relation at $z=0$. The black line shows the median result of our model, with the 2D histogram underneath representing individual galaxies in purple. The model was only run on 1/512 of the Millennium simulation, though on trees thought to be representative. Each panel represents a different set of observations, Rémy-Ruyer et al. (2015) in the top left, Bourne et al. (2012) top right, Ciesla et al. (2014) bottom left and Santini et al. (2014) bottom right.	90

5.9	The stellar-dust mass relation for redshifts $z=0-8$. The black line shows the results from the Millennium simulation, where as the red line shows the results from the Millennium-II simulation. A line is drawn at $10^9 M_{\odot}$ (roughly the convergence point) to guide the eye.	92
5.10	The stellar-dust mass relation at $z=0$ when running different variations of the dust model. These include: AGB dust production only (top left); supernovae type II production only (top right); supernovae type Ia production only (centre left); grain growth production only (centre right); no dust destruction (bottom left); and the idealised model with all production and destruction mechanisms (bottom right). The purple points show individual galaxies in our model and the black line shows the median. Red, green, orange and blue points show the observational constraints.	93
5.11	The stellar-dust mass relation at $z=0-7$ when running different variations of the dust model. These include: AGB only; SNII only; SNIa only; grain growth in molecular clouds only; no destruction; and a fiducial model with all production mechanisms switched on with destruction. The black points show observations from a number of different sources as described in the text.	95
5.12	Stellar-dust mass relation at $z=0$ with the dust accretion timescale set as a free parameter. It takes a value of 0.2Myr in the top panel, 2.0Myr in the central panel and 20Myr in the bottom panel.	97
5.13	Stellar-dust mass relation at $z=0$ while varying the amount of dust destroyed in the model. The top panel shows a model where we have reduced dust destruction by a factor of 10, the central panel shows the ‘normal’ destruction, and the bottom panel shows increased destruction by a factor of 10.	98
5.14	Variations of the stellar-dust relation at different redshifts ($z=0-7$) for variations of the dust growth and dust destruction efficiencies in the model.	100
6.1	The stellar-dust mass relation for redshifts $z=0-8$. The purple points show a 2D histogram of individual galaxies in our model and the black line shows the median. Red, green, orange and blue points show the observational constraints from Ciesla et al. (2014), Rémy-Ruyer et al. (2015), Bourne et al. (2012) and Santini et al. (2014) respectively.	105

6.2	The dust-to-gas ratio as a function of stellar mass. The purple points show a 2D histogram of individual galaxies in our model and the black line shows the median. Green points show the observational constraints from Rémy-Ruyer et al. (2015).	107
6.3	The dust-to-gas ratio as a function of oxygen abundance. The purple points show a 2D histogram of individual galaxies in our model and the black line shows the median. Green points show the observational constraints from Rémy-Ruyer et al. (2015).	108
6.4	The dust-to-metal ratio as a function of stellar mass. The purple points show a 2D histogram of individual galaxies in our model and the black line shows the median. Green points show the observational constraints from Rémy-Ruyer et al. (2015).	109
6.5	The dust-to-metal ratio as a function of oxygen abundance. The purple points show a 2D histogram of individual galaxies in our model and the black line shows the median. Green points show the observational constraints from Rémy-Ruyer et al. (2015).	111
6.6	The production rate of dust through different mechanisms as a function of redshift. Red, blue and yellow lines show the contribution from stellar sources of dust production, type II supernovae, AGB stars and type Ia supernovae respectively. The green line shows the contribution from grain growth inside molecular clouds. The black line shows the dust destruction rate. The orange line shows the sum of all production processes and takes into account the destruction, and is thus the total dust production rate. We also plot the star formation rate density as a dashed cyan line for comparison.	112
6.7	The production rate of different dust mechanisms as a function of stellar mass, shown at different redshifts $z=0-8$. Red, blue and yellow lines show the contribution from stellar sources of dust production, type II supernovae, AGB stars and type Ia supernovae respectively. The green line shows the contribution from grain growth inside molecular clouds. The black line shows the dust destruction rate.	114
6.8	The evolution of the stellar-dust relation (top), DTG ratio (central) and DTM ratio (bottom) over a redshift range of $z=0-8$. This plot combines the different redshift results from Figures 6.1, 6.2 and 6.4 for comparison.	116

6.9	The Dust Mass Function (DMF) for redshifts $z=0-8$. The black line shows the prediction of our model using the underlying dark matter Millennium simulation, and the red line for Millennium-II. Observations are taken from Vlahakis et al. (2005) and Clemens et al. (2013) at $z=0$	118
6.10	The stellar-dust relation (top panel) and the dust production rates (lower panel) for $z=15$ to $z=8$, the redshift range where we may potentially find the first galaxies using JWST.	120

Part I

Introduction

Chapter 1

Introduction

With the installation of Wide Field Camera 3 (WFC3) on the *Hubble Space Telescope* (*HST*) in 2009 it is now possible to identify statistically useful and robust samples of star forming galaxies in the early Universe ($z > 4$, Oesch et al., 2010; Bouwens et al., 2010a; Bunker et al., 2010; Wilkins et al., 2010; Finkelstein et al., 2010; McLure et al., 2010; Wilkins et al., 2011a; Lorenzoni et al., 2011; Bouwens et al., 2011; McLure et al., 2011; Finkelstein et al., 2012a; Lorenzoni et al., 2013; McLure et al., 2013; Duncan et al., 2014; Finkelstein et al., 2015). In recent years a tremendous effort has been dedicated to quantifying the photometric and physical properties, such as star formation rates and stellar masses, of these galaxies. As we continue to dig deeper, with the first sources now identified at $z \approx 10$ (e.g. Oesch et al., 2012; Ellis et al., 2013), and with the launch of the *James Webb Space Telescope* (*JWST*) in the next few years, we will further be able to constrain the physics of galaxy formation and evolution in this critical epoch of the Universe's history.

Although it lasts less than 0.8 Gyr, the period of the Universe between $z = 7$ and $z = 4$ is important to study because it defines an epoch of interesting galaxy formation and evolution activity. The start of this period marks the end of the epoch of reionization; galaxies are starting to ramp up their metal and dust production; and we are finding evidence of the first quasars. While astronomy is unique in allowing us to observe the Universe at these early times, theoretical modelling is required to interpret those observations in terms of an evolving galaxy population. The rapidly advancing observational constraints on the physical properties of galaxies in the early Universe provide an opportunity to further test and refine these galaxy formation models.

The most well studied property of the galaxy population at high-redshift (in part due to its accessibility) is the rest-frame ultraviolet (UV) luminosity function (LF). Because of

the link between the UV luminosity of galaxies and their star-formation rates, the observed UV LF provides an important constraint on star-formation activity in the early Universe. While early observational results were based on only small samples (Bouwens et al., 2008; Bouwens et al., 2010b,a; Bunker et al., 2010; Oesch et al., 2009; Oesch et al., 2010; Ouchi et al., 2009; Wilkins et al., 2011b; Robertson et al., 2010; Dunlop et al., 2010; Lorenzoni et al., 2011), we have slowly begun building larger catalogues, first with 200 – 500 galaxies (Finkelstein et al., 2010; Bouwens et al., 2011; McLure et al., 2013), with the most recent observations having almost 1000 galaxies at $z \geq 7$ (Bouwens et al., 2015; Finkelstein et al., 2015). Consistent with a hierarchical build up of the most massive galaxies, the bright end of the UV LF is shown to build up substantially with time (Bouwens et al., 2007), and the faint-end slope is found to be very steep at redshifts $z > 3$ (Bouwens et al., 2011).

While the intrinsic UV luminosity is known to be a useful diagnostic of star-formation activity (e.g. Wilkins et al., 2012), it is susceptible to even small amounts of dust ($A_{UV} \approx 10 \times E(B-V)$). Direct comparison of the observed UV luminosity function with predictions from galaxy formation models is then sensitive to the reliability of the dust model (which has to account for the creation and destruction of dust, and its effect on the intrinsic spectral energy distribution).

Whilst challenging, it is observationally possible to constrain the dust obscuration and thus determine the true (or intrinsic) star formation activity, even in distant galaxies. Starlight that is absorbed by dust is reprocessed and emitted in the rest-frame mid/far-IR. Combining the star-formation rate inferred from the observed UV with that inferred from the mid/far-IR emission then provides a robust constraint on the total (or intrinsic) star-formation activity. Observational constraints on the rest-frame mid/far-IR emission in high-redshift galaxies are, however, challenging due to the significantly lower flux sensitivity and poorer spatial resolution of facilities operating at these wavelengths. With that said, in recent years the *Herschel Space Observatory* has made great strides in quantifying the intermediate to high ($z=2-5$) galaxy population (e.g. Dowell et al. (2014), Shu et al. (2016)). Thus far there is only a single galaxy individually detected in the far-IR at $z > 6$ (Riechers et al., 2013). This is, however, likely to rapidly improve now that the *Atacama Large Millimetre Array (ALMA)* is fully operational. The contribution of ALMA observations to the literature has, so far, varied in size quite dramatically. From the detection of a smaller number of galaxies, such as the six luminous quasars observed at $z=5$ (Trakhtenbrot et al., 2017) or the 3 intense star bursting galaxies at $z=5-6$ (Pavesi et al., 2016), to larger statistical surveys, such as the ~ 100 galaxies observed at the high mass

end of the main sequence at $z=4$ (Schreiber, 2017) to the probing of the dust enshrouded star formation of 330 galaxies (Bouwens et al., 2016). ALMA has also detected the most luminous star bursting system known at $z>4$ with an observed SFR of $\sim 4300 M_{\odot} \text{ yr}^{-1}$ (Oteo et al., 2016).

Galaxies have been identified at higher redshifts using photometric methods, but without a spectroscopic measurement this can lead to large errors in the measurement of the redshift. To find the redshift of galaxies we require a distinguishing feature in the spectrum, such as the Lyman-break or Lyman-alpha emission. These techniques were originally intended to work at redshifts $z=3-4$, but with the use of new infrared cameras from the likes of *Herschel* and *ALMA*, this method has been made use of at higher redshifts too.

One alternative to using far-IR/sub-mm observations is to take advantage of the relationship between the rest-frame UV continuum slope, β , which is easily accessible even at $z \sim 10$ (Wilkins et al., 2016) and the UV attenuation (first applied by Meurer et al., 1999). This is particularly useful at very high-redshifts, where the far-infrared is generally inaccessible and the measurement of the UV continuum is needed in order to determine the amount of dust in these galaxies. The measurement of β in high-redshift galaxies has, in recent years, been the focus of intense study (e.g. Stanway et al., 2005; Bouwens et al., 2009; Bunker et al., 2010; Bouwens et al., 2010b; Wilkins et al., 2011b; Dunlop et al., 2012; Bouwens et al., 2012; Finkelstein et al., 2012b; Rogers et al., 2013; Wilkins et al., 2013a; Bouwens et al., 2014). Measurements of the UV continuum slope have been used to effectively correct the observed UV luminosity function and thus determine the star-formation-rate distribution function (e.g. Smit et al., 2012). It is important to note, however, that this relation is sensitive to a number of assumptions (Wilkins et al., 2012, 2013a) which introduce both systematic biases and increase the scatter in individual observations.

The *Hubble Space Telescope* and *Wide Field Camera 3* have also been vital in our understanding of the very early universe. The *Hubble Ultra-Deep Field*, despite being such a small area on the sky, has been home to a number of very high-redshift detections, and the combination of *Hubble*, *Spitzer* and *Chandra* observations in the *Great Observations Origins Deep Survey (GOODS)* led to the discovery of the highest redshift object ever detected, with a spectroscopic confirmed redshift of $z=11.1$, when the universe was only 400,000 years old (Oesch et al., 2016).

By combining space (from *Hubble*) and ground-based near-IR observations ($< 2\mu\text{m}$)

from the *Infra-red Array Camera (IRAC)* aboard the *Spitzer Space Telescope* it is possible to probe the rest-frame UV to optical spectral energy distributions (SEDs) of galaxies at high redshift. This is critical to deriving robust stellar masses and thus the galaxy stellar mass function (GSMF). The measurement of stellar masses at high-redshift is, unfortunately, affected by various issues, including: the low sensitivity of the *IRAC* observations; assumptions regarding the star formation and metal enrichment history of these galaxies; and the effects of strong nebular emission (e.g. [Wilkins et al., 2013a](#)). Despite these obstacles, several groups have now attempted to measure the galaxy SMF in the high-redshift Universe (e.g. [Stark et al., 2009](#); [Labbé et al., 2010](#); [González et al., 2011](#); [Yan et al., 2012](#); [Duncan et al., 2014](#)) permitting a direct comparison with galaxy formation models.

To summarise, dust is the key to solving problems in many parts of astronomy. From an observational stand point, understanding the dust content is vital to understanding many physical properties derived from both UV and FIR emission. The UV emission of galaxies in-particular is highly susceptible to even a small amount of dust. Despite the successes of *Herschel* and *ALMA* in probing dust obscured star formation, and the use of the UV continuum slope at higher redshifts, more work needs to be done. In galaxy formation models for example, the luminosity function is extremely sensitive to the choice of dust model. Understanding the dust content of galaxies at all times is vital to reconciling observations and simulations.

1.1 Simulations of galaxy formation

Observations are a vital piece of the puzzle in figuring out how the stars and galaxies in our universe evolved, but they are not always sufficient in allowing us to determine and understand the physical processes involved. Computer simulations help fill in the missing piece by allowing us to test the underlying physics and processes involved, and complete the picture by then comparing with observations to see what changes need to be made. Indeed, some of the most impressive and computationally expensive simulations ever run have been astrophysical in nature. There are three types of simulation commonly used in astronomy: N-body dark matter only simulations which follow the dark matter particles as they form structure on the largest scales; Hydrodynamical simulations which follow both dark and baryonic matter; and finally semi-analytical modelling which uses analytical prescriptions for baryonic physics built on top of the large scale structures of an external dark matter only simulation.

In a world of finite computing power, the choice of simulation is often determined by the question we are trying to answer. Hydrodynamical simulations can provide a ‘complete’ picture as they follow both the dark and baryonic matter, but extending this to large cosmological volumes can be very expensive. Since dark matter is only expected to interact gravitationally, we can push simulations to larger volumes by considering dark matter only models, but this of course lacks baryonic physics, vital to understanding the field of galaxy formation and evolution. Semi-analytical models provide a bridge between the two, allowing us to have large cosmological volumes including all the relevant physics. As they are cheap to run, you are also able to test many different physical models. Each type of model has its advantages and disadvantages but semi-analytic models have had more success in predicting galaxy populations consistent with observations in the local universe.

The dark matter only MILLENNIUM simulation (Springel et al., 2005) was the largest cosmological N-body simulation of its kind when it was run in 2005. MILLENNIUM used a box length of $500h^{-1}Mpc$ and point particle mass of $\sim 10^9M_{\odot}$, providing a huge cosmological volume to study the formation of cold dark matter structures.

Two recent highlights in Hydrodynamical simulations are EAGLE (Schaye et al., 2015) and ILLUSTRIS (Vogelsberger et al., 2014). There are a number of EAGLE simulations, but the fiducial model uses a box length of $100h^{-1}Mpc$ and a baryonic and dark matter particle size of $\sim 10^6M_{\odot}$ and $\sim 10^7M_{\odot}$ respectively. EAGLE has shown that it is able to reproduce the local universe galaxy population, particularly the $z=0$ Galaxy Stellar Mass Function (GSMF) which is in very good agreement with observations, unprecedented for hydrodynamical simulations and comparable to semi-analytical models. They also find fairly good agreement for evolution of galaxy and AGN properties at higher redshifts (Furlong et al., 2015). ILLUSTRIS uses a slightly smaller box size of $75h^{-1}Mpc$ but similar particle masses of $\sim 10^6M_{\odot}$ and $\sim 10^7M_{\odot}$ for baryonic and dark matter respectively, and also finds success in reproducing the GSMF.

1.2 Semi-Analytics

Semi-analytic models (SAMs) provide a relatively inexpensive method of self-consistently evolving the baryonic components associated with dark matter merger trees, derived from N -body simulations or Press-Schechter (Press and Schechter, 1974) calculations. The term semi-analytic comes from the use of coupled differential equations (rather than numerical calculations), to follow the evolution of galaxy formation physics determining the prop-

erties of gas and stars. Physics commonly found in most SAMs to model the transfer of mass and energy include descriptions of: (1) primordial infall and the impact of an ionizing UV background; (2) Radiative cooling of the gas; (3) Star Formation recipes; (4) Metal enrichment; (5) Super-massive black hole growth; (6) Supernovae and AGN feedback processes; (7) The impact of environment and mergers including galaxy morphologies and quenching. An overview of SAMs including descriptions of all the physics typically used in them can be found in the review by [Baugh \(2006\)](#).

One of the biggest benefits of using a SAM is that they are cheap to run. As well as being able to include much more physics than in the standard hydrodynamical models, making modifications or adding new physics as an experiment can be done relatively quickly and allows you to test many different physical models, more than you would be able to by using other forms of galaxy formation modelling. The typical time to run the EAGLE and ILLUSTRIS hydrodynamical simulations mentioned above is in the order ~ 4.5 million CPU hours, where as the default version of the L-GALAXIES SAM takes only ~ 1000 CPU minutes. For the same reason, it is possible to constrain SAMs using statistical methods such as MCMC, which requires running the model thousands of times to obtain a set of free parameters that can reproduce key observables (such as the low redshift GSMF), an idea that would be impossible to implement in hydrodynamical models.

There are two common criticisms of SAMs. The first is that they are too simplistic as they include a large number of free parameters that allow the model to fit any conceivable constraint without teaching us about the physics involved. It is important to remember that the free parameters represent aspects of a physical process, such as the efficiency of black hole accretion, and actually highlight the areas of galaxy evolution that are poorly understood and require further study. The recent adoption of statistical methods such as MCMC to help constrain these parameters (e.g. [Kampakoglou et al. \(2008\)](#); [Henriques et al. \(2009\)](#)) reveal places where the model breaks down and alternate ideas are needed. This is not a problem for SAMs alone either. Hydrodynamical models also contain a large number of free parameters for the same reasons.

The second common criticism of SAMs is that they offer no predictive power, as they simply reproduce the known relations that were used to build the model. However, due to their efficiency at modelling the statistical properties of the galaxy population as a whole, SAMs have identified several problems in theoretical astrophysics, such as the need for feedback in massive galaxies ([White and Rees, 1978](#)), and the discrepancy between the number of predicted and expected dwarf galaxies ([Kauffmann et al., 1993](#)).

Perhaps the most noteworthy galaxy formation semi-analytic models are L-GALAXIES (Springel et al., 2001; De Lucia et al., 2004; Springel et al., 2005; Croton et al., 2006; De Lucia and Blaizot, 2007; Guo et al., 2011, 2013; Henriques et al., 2013, 2015), GALFORM (Cole et al., 2000; Bower et al., 2006; Font et al., 2008; González et al., 2014; Lacey et al., 2016), and SANTACRUZ (Somerville and Primack, 1999; Somerville et al., 2008, 2012). All three SAMs have evolved in parallel with one another and while they all include models of all the physical processes described above, they all have slightly different prescriptions and constraints which lead to varying results. A recent comparison of these models (among others) can be found in Knebe et al. (2015), which also includes an overview of the physics of each model.

1.2.1 Thesis outline

We structure the thesis as follows: in Chapter 2 we provide a full overview of the physics included in the L-GALAXIES SAM; in Chapter 3 we extend the model to make predictions of physical and derived quantities at high-redshift; in Chapter 4 we provide an introduction to the physics involved in dust modelling; in Chapter 5 we discuss the testing and implementation involved in building our dust model and integrating it into L-GALAXIES; in Chapter 6 we present our predictions for the properties of dust from galaxies in our model. Finally, we conclude our work in Chapter 7.

Unless otherwise stated, all work in this thesis has adopted a Chabrier initial mass function (Chabrier, 2003) and uses a Planck cosmology as defined in Planck Collaboration et al. (2014). Number densities are presented per co-moving volume, ($h^{-1} \text{Mpc}$)³.

Chapter 2

Overview of Physics

The coupling of semi-analytics to model the physics of baryonic matter with a high resolution N-body dark matter simulation in this work follows the techniques originally proposed in [Springel et al. \(2001\)](#). The work presented in this thesis was developed using the latest version of L-GALAXIES presented in [Henriques et al. \(2015\)](#), which builds on over two decades of research into semi-analytic galaxy formation modelling ([Kauffmann et al., 1999](#); [Springel et al., 2001](#); [De Lucia et al., 2004](#); [Springel et al., 2005](#); [Croton et al., 2006](#); [De Lucia and Blaizot, 2007](#); [Guo et al., 2011, 2013](#); [Henriques et al., 2013](#)).

This chapter presents the physics used in the version of L-GALAXIES used in this thesis, primarily described in [Henriques et al. \(2015\)](#), but built on almost 20 years of modifications to the original SAM. The only contribution to the physics presented in this chapter from our work is a modification to redshift dependence of the dust extinction calculation, as described in Section 2.8.3. We show our motivation for this change in Chapter 3. Another significant change to the SAM presented in [Henriques et al. \(2015\)](#) is the implementation of the detailed chemical enrichment model described in Section 2.4 from [Yates et al. \(2013\)](#). The detailed dust model is the last significant difference to the [Henriques et al. \(2015\)](#) SAM, but we choose to withhold its description until Chapters 4 and 5, as it constitutes a vital part for the latter half of this thesis.

2.1 L-GALAXIES

L-GALAXIES, also known as the Munich semi-analytical model ([Kauffmann et al., 1999](#); [Springel et al., 2001](#); [De Lucia et al., 2004](#); [Springel et al., 2005](#); [Croton et al., 2006](#); [De Lucia and Blaizot, 2007](#); [Guo et al., 2011, 2013](#); [Henriques et al., 2013, 2015](#)). is a semi-analytic model of galaxy formation built to run on top of subhalo trees produced

by a dark matter only simulation. The predicted properties of any semi-analytic model built in this way are obviously dependent on the underlying dark matter simulation. Not only is it used to seed the initial mass of hot gas for a galaxy, that later cools and forms stars, it is also vital to knowing the interaction history of galaxies such as major mergers. The evolution of stars and galaxies are both very interesting subjects to study, yet where you can tell almost everything you need to know about how a star will evolve based on its initial mass, the same cannot be said for galaxies. This is because stars rarely interact, where as galaxies are thought to interact much more frequently. Indeed, galaxy interactions are necessary to explain many areas of astrophysics, including super massive black hole growth, AGN activity, and the ‘red and dead’ elliptical galaxy population at recent times. For this reason, it is crucial to use a dark matter simulation with sufficient volume to sample the most massive clusters of galaxies in the universe, while at the same time resolving dwarf galaxy populations, such as the Millennium ([Springel et al., 2005](#)) and Millennium II ([Boylan-Kolchin et al., 2009](#)) simulations.

L-GALAXIES traces the formation and evolution of galaxies according to the physical laws that govern the transfer of mass and energy among the stars found in the galactic disk, galactic bulge and in the halo; the hot and cold gas phases; the central supermassive black hole; and any gas that is lost via ejection and other feedback mechanisms. The physics used in L-GALAXIES has been motivated by a mixture of both observations and simulations, and over the years, L-GALAXIES has found success in reproducing both the stellar mass function and luminosity function in the local universe and out to redshift $z=3$. The model has also reproduced the large-scale clustering of galaxies, the Tully-Fisher relation, the optical colours of local galaxy populations, and the gas phase mass metallicity relation that has been observed in the local universe.

Fig 2.1 shows a generalised schematic of the main physical processes that occur inside our model for each galaxy and at each time step. The model treats galaxies as several separate components: those that contain information about the gas, Cold Gas (ISM), Hot Gas (CGM) and Ejected Gas (ICM); those that contain information about the stars, Stellar Bulge and Stellar Disk; and an additional component that monitors the black hole mass. Very simply, looking at Fig 2.1 as a guide, we see that gas infalls into the galaxy from the halo and is placed into the CGM, where it is cooled into the ISM. Gas inside the ISM is susceptible to star formation processes, which fills the bulge and disk components. Star formation also enriches the gas phases with metals, and also feedback processes that can reheat and eject gas into different phases, where it can be later reintegrated into a

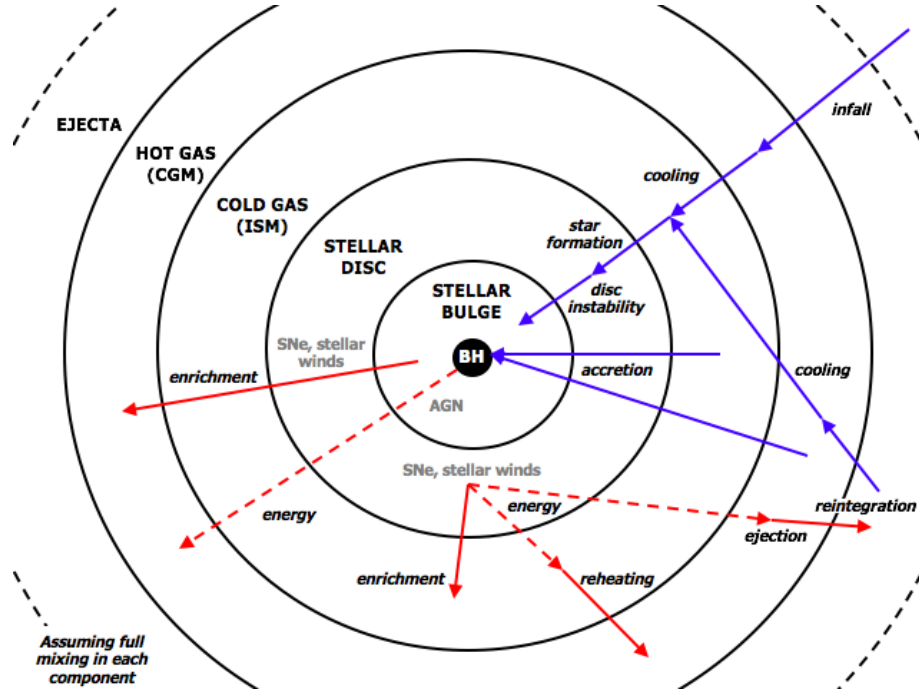


Figure 2.1: A schematic showing the main physical processes that occur inside the model inside each galaxy at every time step. Solid lines represent the transfer of mass, and dashed lines the transfer of energy. This schematic was provided by Rob Yates.

galaxy. On top of this we also have accretion processes onto the central black hole. All of these processes will be described in more detail below.

2.1.1 Millennium simulations

For all the work in this thesis, we use the dark matter structures provided by the Millennium simulations as the foundation of the semi-analytic model. The Millennium simulation (Springel et al., 2005), was the largest N-body simulation of its time (in 2005), tracing how the dark matter mass distribution evolved through time in a box with length 500Mpc/h. Due to the large box size, Millennium is only sensitive to structures at a resolution of $10^9 M_{\odot}$. To probe less massive galaxies, the simulation was re-run in 2009 with the same number of particles but in a smaller box, with length ~ 100 Mpc/h, in order to have higher mass resolution, and this simulation is known as Millennium-II (Boylan-Kolchin et al., 2009). Both simulations follow 10 billion dark matter particles from a redshift $z=127$ down to $z=0$ and together they trace five orders of magnitude in stellar mass at $z=0$ from 10^7 to $10^{12} M_{\odot}$. The postage stamps in Fig 2.2 shows three images of the Millennium simulation at $z=0$, showing the large scale structure of the dark matter on the largest scales (left), to very high resolution of a massive dark matter halo (right).

The original Millennium and Millennium II simulations were run assuming a Λ CDM cosmology with parameters from a combined analysis of 2dFGRS (Colless et al., 2001) and *WMAP1* (Spergel et al., 2003). Using the techniques developed by Angulo and White (2010) and updated in Angulo et al. (2014), this cosmology has been scaled to the latest results from the *Planck* data (Henriques et al., 2015). The cosmology used in this thesis is thus now defined as: $\sigma_8 = 0.826$, $H_0 = 67.3 \text{ km s}^{-1} \text{ Mpc}^{-1}$ ($h = 0.673$), $\Omega_\Lambda = 0.685$, $\Omega_m = 0.315$, $\Omega_b = 0.049$, ($f_b \approx 0.156$) and $n = 0.961$.

The dark matter particle data for Millennium and Millennium II is stored in 64 and 68 snapshots respectively, with the last 60 snapshots from each simulation being at the same redshifts. To identify groups of particles bound together at each snapshot, we use the friends-of-friends algorithm (Geller and Beers, 1982), which identifies halos by calculating the viral masses and joining together particles into groups defined as having a mean-over-darkmatter-density ~ 200 times the critical value for the universe, which is approximately what is expected for a virialised group. The next step is to identify sub-haloes within these friends-of-friends groups, which is done using the SUBFIND routine (Springel et al., 2001). Sub-haloes represent over-dense sub-structures inside each FOF group and this is critical to galaxy formation modelling as this is where galaxies are assumed to reside.

After determining what the dark matter structures and sub-structures look like at each redshift, their evolution is determined by linking halos and sub-haloes to their progenitors at earlier times (earlier snapshots) and saved as ‘merger trees’. These merger trees are then used as the input for the SAM, giving information on the size and distribution of dark matter halos, coupled with their merger history. Since the halos contained within each merger tree are gravitationally isolated from other structures, the properties of galaxies within each tree are only determined by the dark matter halos inside it. Thus the SAM can be run on each tree separately.

2.2 Infall and cooling

Infall

Initially each dark matter halo is seeded a baryonic mass according to the baryonic fraction set by the cosmology, which in our case is $f_b = 15.5\%$ for PLANCK, assuming a primordial composition of 75% hydrogen and 25% helium. This baryonic matter is initially presented as primordial gas and placed directly into the hot gas (CGM) as it is expected to shock-heat as it falls into the gravitational potential well of the halo.

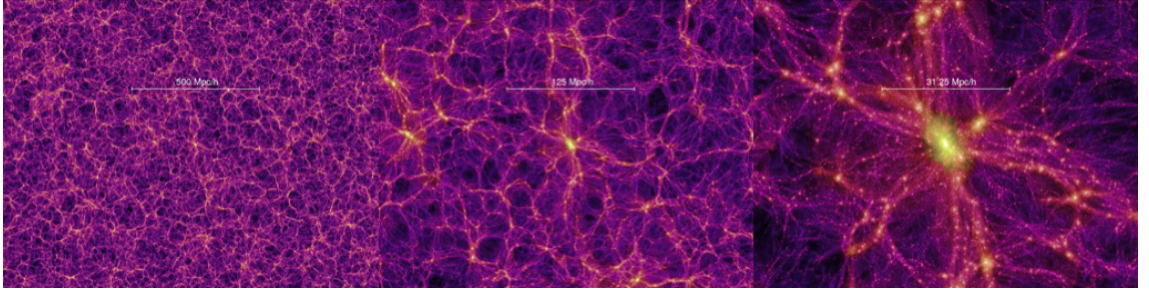


Figure 2.2: Stamps of 15 Mpc/h thick slices from the Millennium simulation at a resolution of 500 Mpc/h (left), 125 Mpc/h (centre) and 31.25 Mpc/h (left). Images taken from the Millennium Simulation Project website (<https://wwwmpa.mpa-garching.mpg.de/galform/virgo/millennium/>).

Information on the masses of dark matter halos are available from the underlying dark matter only simulation, and as time progresses the dark matter halos grow in size. Any new mass that is needed as time progresses that is not already part of the galaxy, is added in the same way, as a primordial gas into the CGM. The baryonic mass available for infall is susceptible to heating from the photoionizing background, and this is discussed in Section 2.5.1.

Cooling

Following the formulation of [White and Frenk \(1991\)](#), the cooling of gas from the CGM into the galactic disk falls into one of two regimes based on the mass of the halo and the redshift at which the halo formed. By assuming gas cools from a hot atmosphere where its distribution is isothermal, the cooling time is given by the ratio between the thermal energy and the cooling rate per unit volume:

$$t_{cool}(r) = \frac{3\mu m_H k T_{vir}}{2\rho_{hot}(r)\Lambda(T_{hot}, Z_{hot})} \quad (2.1)$$

where μm_H is the mean particle mass, k is the Boltzmann constant, Z_{hot} is the hot gas metallicity. The temperature of the gas can be obtained from the circular velocity of the halo using the hydrostatic equilibrium condition: $kT = \frac{1}{2}\mu m_p V_c^2$. T_{hot} is then the temperature of the hot gas which is assumed to be the virial temperature of the halo given by $T_{hot} = 35.9(V_{vir}/km s^{-1})^2 K$ (for sub-haloes we use the temperature as estimated at infall). $\Lambda(T_{hot}, Z_{hot})$ is the equilibrium cooling function for collisional processes which depends both on the metallicity and temperature of the gas but ignores radiative ionization effects ([Sutherland and Dopita, 1993](#)). The hot gas density as a function of radius for a

simple isothermal model is given by:

$$\rho_{gas}(r) = \frac{m_{hot}}{4\pi R_{vir} r^2} \quad (2.2)$$

We take the cooling radius to be where the cooling time equals the halo dynamical time:

$$r_{cool} = \left[\frac{t_{dyn,h} M_{hot} \Lambda(T_{hot}, Z_{hot})}{6\pi \mu m_H k T_{vir} R_{vir}} \right]^{\frac{1}{2}} \quad (2.3)$$

where $t_{dyn,h}$ is the dynamical time of the halo. The dynamical time represents the shortest possible time it can react to an imbalance of pressure and gravity (shocks occur when it cannot react fast enough), and takes the form $t_{dyn,h} = R_{vir}/V_{vir} = 0.1H(z)^{-1}$ (De Lucia et al., 2004).

At early times, and in low mass haloes, the cooling radius can be longer than the viral radius ($r_{cool} > R_{vir}$), and so gas is able to cool rapidly in less than the free-fall time. This cold-flow accretion is modelled as:

$$\dot{M}_{cool} = \frac{M_{acc}}{t_{dyn,h}} \quad (2.4)$$

where M_{acc} is the amount of mass to be accreted.

At late times, and in massive halos, the accretion shock radius is large and so a hot gas atmosphere is formed. In this case, ($r_{cool} < R_{vir}$), the accretion rate is reduced to a cooling flow that takes the form:

$$\dot{M}_{cool} = \frac{r_{cool}}{R_{vir}} \frac{M_{hot}}{t_{dyn,h}} \quad (2.5)$$

2.3 Star formation

There are two main modes of star formation used in the model: that of quiescent star formation that occurs in the traditional sense where cold gas clouds collapse into stars over long time periods; and that of starbursts that occur during merger driven activity.

2.3.1 Quiescent Star Formation

At each time step, stars form from the amount of cold gas available, and the star formation rate is taken to be:

$$\dot{M}_{\star} = \alpha_{SF} \frac{(M_{coldgas} - M_{crit})}{t_{dyn,disk}} \quad (2.6)$$

where \dot{M}_\star is the mass of stars formed; $M_{coldgas}$ is the mass of cold gas; M_{crit} is the critical threshold mass for star formation described below; $t_{dyn,disk}$ is the dynamical time of the disk and is described by $\frac{r_{disk}}{V_{vir}}$; and α_{SF} is the star formation efficiency which is constrained using MCMC (see Section 2.9), and currently takes the value of 0.025 (see Table 2.1).

The critical mass of star formation is based on the work of Kauffmann et al. (1996) where there is a critical surface density above which gas can collapse into stars and is based on observations from Kennicutt (1998). It takes the form:

$$M_{crit} = M_{crit,0} \left(\frac{V_{vir}}{200 \text{ km s}^{-1}} \right) \left(\frac{r_{disk}}{10 \text{ kpc}} \right) M_\odot \quad (2.7)$$

where V_{vir} is the virial velocity and r_{disk} is the disk radius calculated using the methodology of Mo et al. (1998). $M_{crit,0}$ is a parameter that has always taken the value of $3.8 \times 10^9 M_\odot$ in L-GALAXIES since Kauffmann et al. (1999) introduced it as it provides a good fit to local observations. In the version of the model used in this thesis, $M_{crit,0}$ is constrained using MCMC and currently takes the value $2.4 \times 10^9 M_\odot$ (see Table 2.1).

It is assumed that a fraction of stars formed, R_{ret} , are very massive and thus have very short life spans, and are returned to the cold gas reservoir immediately. R_{ret} is calculated from the Chabrier (2003) initial mass function and takes the value $R_{ret} = 0.43$. Therefore the actual amount of mass added to the stellar disk component (and removed from the cold gas) is: $(1 - R_{ret})\dot{M}_\star$.

2.3.2 Merger Driven Star Formation

For star formation that occurs during merger driven activity we use the collisional starburst model of Somerville et al. (2001) based on the simulations of Mihos and Hernquist (1996) where a fraction of the combined cold gas masses of both galaxies is turned into stars:

$$M_{\star,burst} = \alpha_{SF,burst} \left(\frac{M_1}{M_2} \right)^{\beta_{SF,burst}} M_{coldgas} \quad (2.8)$$

where $M_1 < M_2$ is the total baryonic masses of the two merging galaxies; $M_{coldgas}$ is the total summed cold gas mass of the two merging galaxies; and $\alpha_{SF,burst}$ and $\beta_{SF,burst}$ are free parameters originally chosen to reproduce the results of Mihos and Hernquist (1996), but are now constrained using MCMC. Their values can be found in Table 2.1.

2.3.3 Star formation histories

Several physical processes, including the metal and dust enrichment processes, require us to keep track of the star formation history of each galaxy. L-GALAXIES contains 63

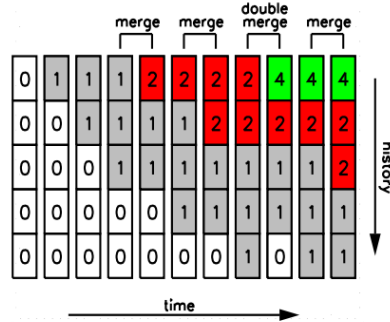


Figure 2.3: Schematic to show the evolution of the first 5 star formation history bins (shown as rows), for an isolated galaxy. The numbers represent the time width of a bin in units of one time step. At every time step in the code (shown as columns), a new bin is activated. Active bins are coloured in this schematic, with grey representing single-width bins, red for double width bins and green for quadruple-width bins. When three or more active bins have the same length, two of the bins are immediately merged, as shown. In the double merge example, two of the single-width bins (grey) are merged into a double-width bin, which makes three, merging two of them together produces the quadruple-width bin. This figure is taken from [Yates et al. \(2013\)](#).

snapshots, which then each contain 20 time steps. To keep the full star formation history at this resolution would require a tremendous amount of memory for the tens of millions of galaxies that exist at $z=0$. Instead, we have adopted a more dynamic approach by which the star formation history array will only ever contain a maximum of 20 elements or bins. As time progresses in the simulation, the oldest star formation history bins are merged together but the newest star formation history bins have a resolution of only one time step. Thus we are able to keep an entire star formation history of each galaxy, with higher resolution at the most recent times and decreasing resolution to longer times. Higher precision at recent times is important because calculating observables such as the luminosity of a galaxy is often dominated by young stars. This process is explored in more detail in [Shamshiri et al. \(2015\)](#), and the specifics of bin merging are described in the schematic in Fig 2.3.

2.4 Chemical enrichment

When stars die, they pollute their surroundings with metals. This thesis includes the use of two separate chemical enrichment models. The standard one that comes with the

[Henriques et al. \(2015\)](#) model is more basic, and assumes that for each solar mass of stars that is formed, there is some yield of metals. This yield is a free parameter that is constrained using MCMC, and currently takes the value of $y = 0.046$. These newly formed metals are integrated into the cold gas phase immediately and can be moved through the various components of the galaxy due to processes such as feedback. This model is used for the work done in Chapter 3 of this thesis.

In Chapters 4 and 5, we implement the detailed chemical enrichment model introduced in [Yates et al. \(2013\)](#). This model includes the delayed enrichment of metals from supernovae and stellar winds by linking the stellar lifetimes with that of mass and metallicity dependent yield tables. The specifics of this model are explained below.

2.4.1 Stellar Lifetimes

Many galaxy formation models (including the standard metal model outlined above) include the use of an instantaneous recycling approximation, which assumes that stars die the moment they are born and thus enrich their environments with metals immediately. However, in the real universe, stars enrich their environments towards the end of their lives and this difference can be an important distinction to make, particularly for low mass stars which can have main sequence lifetimes of billions of years.

We take the stellar lifetimes from the [Portinari et al. \(1998\)](#) metallicity dependent lifetime tables for the delayed enrichment calculations. These tables provide the lifetimes of stars in the $0.6 \leq M/M_{\odot} \leq 120$ mass range and for five different metallicities ranging from 0.0004 to 0.05. The stellar lifetime as a function of mass is plotted in Fig 2.4 for different metallicities. The most massive stars ($120M_{\odot}$) only live for around 3.3Myr depending on their metallicity, where as the least massive stars can live for more than 20Gyr.

2.4.2 Stellar Yields

L-GALAXIES follows the prescription laid out by [Tinsley \(1980\)](#) for the total rate of mass ejected by a stellar population at a time t :

$$e_z(t) = \int_{M_L}^{M_U} M_Z(M, Z_0) \psi(t - \tau_M) \phi(M) dM \quad (2.9)$$

where $M_Z(M, Z_0)$ is the mass of metals released by a star of mass M and metallicity at time of birth of Z_0 . $\psi(t - \tau_M)$ is the star formation rate at the time when the star is born, and $\phi(M)$ is the normalised IMF by number. The amount of mass released for an individual

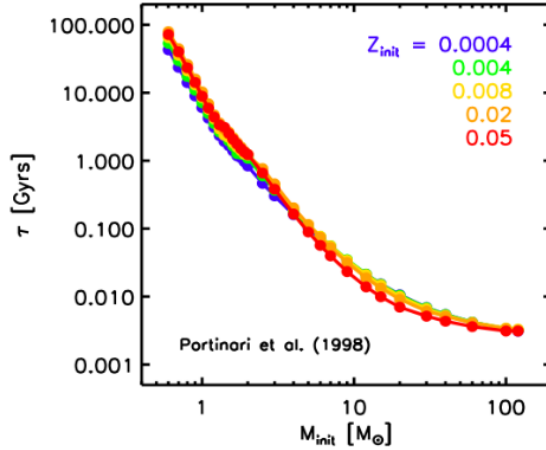


Figure 2.4: The relationship between the initial mass of a star, M_{init} , and its lifetime, τ . The different colours represent the relation for different metallicities. This plot uses the metallicity dependent lifetime tables from [Portinari et al. \(1998\)](#).

star of given mass and metallicity is taken from the following yield tables: [Marigo \(2001\)](#) for low and intermediate mass stars (mainly producing metals via the AGB phase), and [Portinari et al. \(1998\)](#) complete the set for high mass stars (with metal injection via SNI). It is approximated that material is shed at the end of the star's life. Fig 2.5 shows the mass of various elements ejected from individual stars due to AGB winds and supernovae type II.

The production of metals by supernovae type Ia is also considered by including the yield tables of [Thielemann et al. \(2003\)](#). As the star undergoing this type of supernovae is assumed to always be the same mass, these are now only metallicity dependent yield tables, and can also be seen in Fig 2.5. The lifetime of a star undergoing a type Ia explosion is much more complicated than for type II explosions as it depends on what is happening to the white dwarf star. White dwarfs are stable stars, or at least, have lifetimes longer than the current age of the universe, held together in a state of electron degeneracy. They only explode when they accrete enough material to go over the Chandrasekhar mass limit ($\approx 1.39M_{\odot}$) and electron degenerate pressure is no longer sufficient for stabilising the star.

Using a delayed time distribution (DTD) for the mass return of type Ia supernovae is a way of compensating for this. We use power law fit, with slope -1.12, which was found to match the derived SNIa rate from 68,000 galaxies (which included 132 detected SNIa) in the Sloan Digital Sky Survey II (SDSSII) ([Brandt et al., 2010](#)):

$$DTD = a(\tau/Gyr)^{-1.12} \quad (2.10)$$

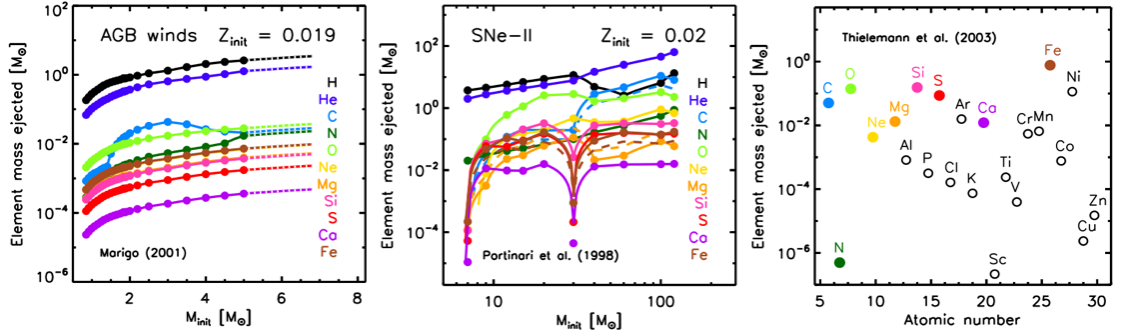


Figure 2.5: Mass released by AGB winds from the [Marigo \(2001\)](#) yield tables (left), type II supernovae from [Portinari et al. \(1998\)](#) yield tables (centre) and type Ia supernovae from [Thielemann et al. \(2003\)](#) yield tables (right). Points indicate the values from the yield tables, and lines the interpolation between those points. Dashed lines show the extrapolation beyond the masses originally modelled. Plots are taken from [Yates et al. \(2013\)](#)

where τ is the delay time since the birth of the SNIa producing binary system, and a is the normalisation constant, coming from the requirement that:

$$\int_{\tau_{min}}^{\tau_{max}} DTD(\tau) d\tau = 1 \quad (2.11)$$

where $\tau_{min} = \tau(8M_{\odot})$ and $\tau_{max} = \tau(0.85M_{\odot})$ are the minimum and maximum assumed lifetimes of a SNIa producing binary in the single degenerate scenario respectively. This choice of DTD means that 45% of supernovae type Ia explode within 400Myr, which is close to the values predicted from the SDSSII observations of the SNe-Ia rate by [Brandt et al. \(2010\)](#) and around the lower limit determined from supernovae remnants in the small and large Magellanic clouds by [Maoz et al. \(2010\)](#).

When comparing this chemical enrichment model to SDSS observations of the oxygen abundance as a function as stellar mass, as in Fig 2.6, we see that the median values of the model and the observations have a good agreement and similar scatters, though the scatter is slightly larger at the high mass end in the model. It provides a much better fit to the observational data than the more basic model traditionally used in the L-GALAXIES SAM (described at the start of this section), which fails to reproduce the shape of the relation.

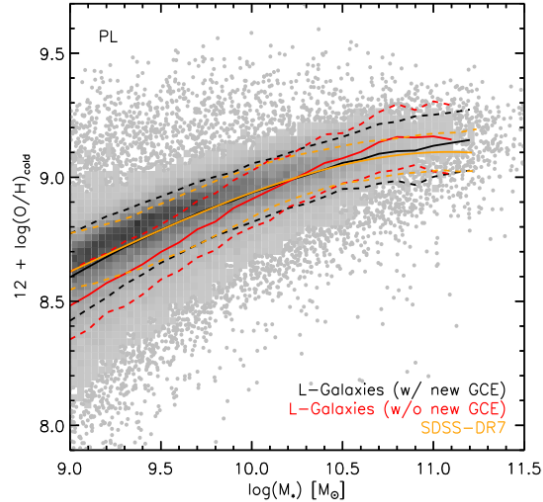


Figure 2.6: The $M_* - Z_{cold}$ relation for L-GALAXIES at $z=0$, showing the new detailed chemical enrichment model (black lines), the old simple model (red lines), compared against observations of emission line galaxies from SDSS (Yates et al., 2012). Plot taken from Yates et al. (2013).

2.5 Feedback

It was first pointed out by semi-analytical models that feedback was necessary in order to explain the discrepancy between the halo mass and luminosity functions predicted by galaxy formation models and observations. Fig 2.7 shows this in more detail (Silk and Mamon, 2012). Galaxy formation models produced a higher number of both low mass and high mass galaxies than were observed in galaxy surveys, but the two converged at the knee of the function. It was explained that some feedback mechanism must be responsible for making star formation less efficient in these systems, and thus quench the over density of both low and high mass galaxies in models. This eventually manifested itself as supernovae feedback, which heats up and ejects the cold gas from low mass galaxies, while AGN feedback can reduce the efficiency of gas cooling in high mass systems.

This section explains all the feedback mechanisms that are considered in the model.

2.5.1 Reionization

One of the most fundamental feedback mechanisms in galaxy formation modelling is reionization. Reionization is important because the photoionizing background is capable of heating the intergalactic medium to temperatures $\sim 10^4\text{K}$, a point where the pressure effects prevent the baryons from accreting onto halos with the dark matter (Efstathiou,

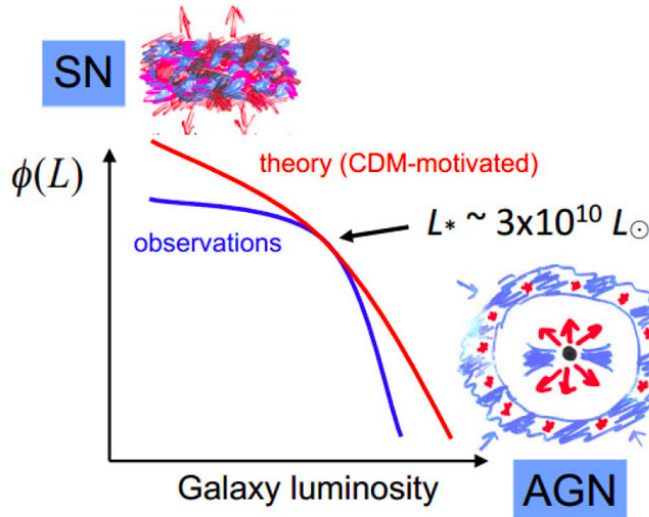


Figure 2.7: The role of feedback in modifying the galaxy luminosity function. Figure taken from [Silk and Mamon \(2012\)](#)

1992). In the model, we follow the results from [Gnedin \(2000\)](#) who defined a filtering halo mass, $M_F(z)$, below which the baryonic fraction is reduced with respect to the universal value ($f_b^{cosmic} = 15.5\%$, see section 2.2). We model this as follows:

$$f_b(z, M_{vir}) = \frac{f_b^{cosmic}}{\left(1 + (2^{\alpha/3} - 1) \left[\frac{M_F(z)}{M_{vir}}\right]^\alpha\right)^{3/\alpha}} \quad (2.12)$$

where the baryon fraction is now a function of redshift, and the virial mass, M_{vir} . α is a free parameter and we adopt $\alpha = 2$. The filtering mass is also a function of redshift, and we take the values of [Okamoto et al. \(2008\)](#), where $M_F(z)$ varies from $6.5 \times 10^9 M_\odot$ at $z=0$ to $10^7 M_\odot$ at $z=8$, just before the onset of the epoch of reionization. For large haloes, with $M_{vir} > M_F(z)$, the suppression of the baryon fraction is negligible, but for haloes with $M_{vir} \ll M_F(z)$ the baryon fraction drops to $(M_{vir}/M_F(z))^3$.

2.5.2 Supernovae

Massive stars have relatively short lifespans and explode as supernovae, releasing a huge amount of energy into the surrounding medium. As a result, some of the cold gas can be reheated to join the hot atmosphere, and the hot atmosphere itself is also subject to further heating, compensating for its cooling and even ejecting gas from the galaxy in a wind. This is one of the most crucial feedback mechanisms and is critical to understanding galaxy formation ([Larson, 1974](#); [White and Rees, 1978](#); [Dekel and Silk, 1986](#)). In order to

produce realistic galaxy populations, a detailed modelling of supernovae is required.

In L-GALAXIES, the energy released by supernovae is calculated according to the mass of material released by stars at a given time. Thus, the total amount of energy produced by supernovae feedback is described by:

$$E_{SN} = \epsilon_{halo} \frac{1}{2} e_M(t) \Delta t V_{SN}^2 \quad (2.13)$$

where $e_M(t)\Delta t$ is the amount of metals released in a given time step; ϵ_{halo} is the halo-velocity-dependent supernova energy ejection efficiency; and V_{SN} is the supernova ejecta speed and is equal to 630km/s.

In the model, stars that die in the disk have their mass and energy released into the cold gas phase, or ISM, where-as stars in the bulge eject their mass and energy into the hot phase, or CGM. Energy injected into the ISM is further able to reheat gas into the CGM, and also eject gas from the galaxy completely (in the model, we refer to this as an ‘ejected gas’ phase). The amount of gas ejected is given by:

$$\Delta M_{ejec} = \frac{E_{SN} - \frac{1}{2} \epsilon_{disk} e_M(t) \Delta t V_{vir}^2}{\frac{1}{2} V_{vir}^2} \quad (2.14)$$

where $\epsilon_{disk} e_M(t) \Delta t$ is the amount of gas that gets reheated but does not get ejected, ϵ_{disk} is the SN feedback gas reheating efficiency. The ejected gas is assumed to return to the hot phase (CGM) in a few dynamical times.

Originally, L-GALAXIES used an instantaneous recycling approximation and thus the energy released by supernovae was proportional to the mass of stars formed instead. This was changed in Yates et al. (2013) with the implementation of the detailed chemical enrichment model (see section 2.4).

2.5.3 AGN

While supernovae feedback is very efficient at quenching low mass galaxies, it does not have a dramatic effect on high mass systems. AGN feedback on the other hand is capable of completely disrupting star formation in high mass galaxies, and is one of the most important mechanisms in the evolution of galaxies from star forming spirals to the ‘red and dead’ ellipticals.

In the model, we follow the methodology of Croton et al. (2006) in assuming that feedback from the central supermassive blackhole is the agent that terminates galaxy growth in massive haloes. Black holes grow when gas is driven to the centre of galaxies, and this is enhanced during mergers of massive systems. We use two modes of AGN

feedback, the quasar mode, which is the result of major mergers and is the main channel by which we see blackhole growth in the model, and radio mode, by which the blackhole is constantly accreting gas from the CGM, generating jets and bubbles, and suppressing cooling onto the galaxy which can eliminate the supply of cold gas and terminate star formation.

Black hole growth - Quasar mode

When two galaxies merge together, their cold gas components are strongly disturbed and this can lead to a significant fraction of the cold gas being driven into the central black hole, or it may form a black hole if one does not already exist. If both merging galaxies have a pre-existing black hole already, they are assumed to merge at the same time as the two galaxies. The amount of cold gas accreted onto the black hole during this phase is taken to be:

$$\Delta M_{BH,Q} = \frac{f_{BH}(M_{sat}/M_{cen})M_{coldgas}}{1 + (V_{BH}/V_{vir})^2} \quad (2.15)$$

where M_{sat} and M_{cen} are the total baryonic masses of the satellite and central galaxies that are merging, $M_{coldgas}$ is the cold gas mass, V_{vir} is the virial velocity of the central halo, and f_{BH} and V_{BH} are free parameters that control the amount of cold gas that is available for accretion onto the black hole, and the virial velocity at which the efficiency saturates. The final black hole mass at the end of the merger is thus:

$$M_{BH,final} = M_{BH,1} + M_{BH,2} + \Delta M_{BH,Q} \quad (2.16)$$

where $M_{BH,1}$ and $M_{BH,2}$ are the masses of the two black holes in the two merging galaxies.

The mass accretion that occurs due to merging galaxies is the main channel of blackhole growth in the model. The fact that bulges (see Section 2.7.1) and blackholes are formed in related processes results in a tight correlation between the black hole and galaxy bulge masses, which has also found in observations (e.g. [Magorrian et al. \(1998\)](#)).

Radio mode - feedback

We assume that the central supermassive blackhole continuously accretes hot gas from their host galaxies, and that this produces radio mode feedback in the form of jets and bubbles, which inject energy back into the hot atmosphere surrounding a galaxy. This accretion rate is given by:

$$\dot{M}_{BH} = k_{AGN} \left(\frac{M_{hot}}{10^{11} M_{\odot}} \right) \left(\frac{M_{BH}}{10^8 M_{\odot}} \right) \quad (2.17)$$

where k_{AGN} is the black hole quiescent hot gas accretion factor.

The relativistic jets and hot bubbles deposit energy at the rate:

$$\dot{E}_{radio} = \eta \dot{M}_{BH} c^2 \quad (2.18)$$

where $\eta = 0.1$ is an efficiency parameter and c is the speed of light. This energy further heats and disrupts the hot gas, which has the effect of suppressing the cooling flow of hot gas into the cold gas disk, resulting in an effective cooling rate given by:

$$\dot{M}_{cool,eff} = \dot{M}_{cool} - 2\dot{E}_{radio}/V_{vir}^2 \quad (2.19)$$

In the model, we assume that the elimination of the cooling flow would also cut off the supply of gas fuelling the black hole, thus terminating further heating of the hot atmosphere. It is further imposed that it is only in the most massive galaxies ($> 10^{10.5} M_{\odot}$) that grow a black hole large enough to produce an amount of heating that is capable of reducing the cooling flow of hot gas, which has the desired effect of only decreasing the cooling in massive halos. This, in turn, decreases the number density of massive systems by suppressing their star formation, and shifting them to the ‘red and dead’ galaxy population (see the mass end of Fig 2.7). This reconciles the model with the notion of cosmic downsizing.

2.6 Reintegration

In the model, gas that is ‘ejected’ from the hot phase by the feedback processes described in the previous section is placed within an ‘ejected’ phase (in the same way our galaxies have a cold gas and hot gas phase). The ejected phase is required in order to quench low mass galaxies from forming too early as the gas is no longer available for cooling, while pushing growth at later times when it finally becomes available between $z=2$ and $z=0$. In actual fact, gas that is ejected from low mass galaxies will never be reincorporated unless the gas becomes part of a more massive system, and in massive galaxies the gas will return almost immediately.

The mass of gas returned to the hot gas halo from the ejecta reservoir is taken to be:

$$\dot{M}_{ejected} = -\frac{M_{ejected}}{t_{reinc}} \quad (2.20)$$

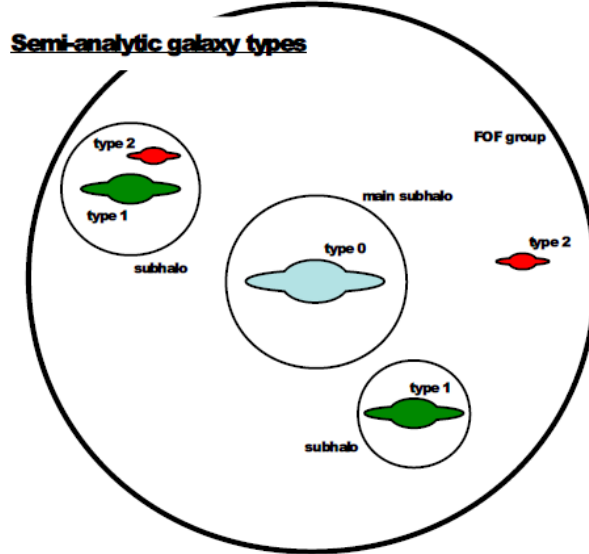


Figure 2.8: A schematic showing the different ‘types’ of galaxies of galaxy considered inside the model. The dark matter halos are also shown by black circles. This figure was provided by Rob Yates.

where the reincorporation time, t_{reinc} , scales inversely with the mass of the host halo:

$$t_{reinc} = \gamma \frac{10^{10} M_{\odot}}{M_{vir}} \quad (2.21)$$

where γ is a free parameter constrained using MCMC whose value can be found in Table 2.1.

2.7 Mergers

Galaxy mergers have been shown to have a very important role in the process of galaxy evolution. They are responsible for starbursts, AGN and quasar activity, and black hole growth, so their implementation in the model is vital.

Galaxies inside the model are labelled in one of three ways, determined from information from the underlying dark matter simulation, as shown in Fig 2.8: a type 0 if they reside in the centre of a dark matter halo; a type 1 if they reside inside their own sub-halo, and a type 2 if they exist without their own halo because it has already been disrupted by the central halo.

In the model a merger can be seen as a two stage process. First, whenever two galaxies get within the gravitational potential of each other, we label the most massive galaxy as

the central galaxy. The satellite becomes a type 1 galaxy, which means that its dark matter halo is now a sub-halo and has started being stripped to become part of the central galaxy main halo. The hot gas of the satellite is immediately stripped and added to the hot gas content of the central galaxy. The satellite is able to continue star formation for as long as it has cold gas. The second phase occurs when the sub-halo of the type 1 satellite is stripped below the resolution limit of the dark matter simulation. At this point, the galaxy loses its halo and becomes a type 2. A merger time scale is then calculated, which dictates the time left until the galaxy merges with its central galaxy companion. This timescale is calculated by assuming that the satellite galaxy is experiencing a force from the central galaxy halo due to dynamical friction:

$$t_{friction} = \alpha_{friction} \frac{V_{vir} r_{sat}^2}{GM_{sat} \ln \Lambda} \quad (2.22)$$

where M_{sat} is the total baryonic and dark matter mass of the satellite galaxy, $\ln \Lambda$ is the Coulomb logarithm: $\ln \Lambda = \ln(1 + M_{vir}/M_{sat})$. $\alpha_{friction}$ is a free parameter constrained by the MCMC (its value can be found in Table 2.1), whose purpose is to match the bright end of the luminosity function at $z=0$.

When the satellite galaxy finally merges with the galaxy at the centre of the main halo, the outcome depends on the baryonic mass ratio of the two, R_{merge} . In a major merger ($R_{merge} > 0.1$), the discs of the two progenitors are destroyed and all their stars become part of the bulge component in the descendent galaxy, as well as any stars that are formed during the merging process. In a minor merger ($R_{merge} < 0.1$), the disc of the larger progenitor galaxy survives and the cold gas component of the smaller galaxy is accreted into it; while any stars in the satellite are added to the bulge of the central galaxy. In both types of merger, cold gas is fed to the central black hole, as described in Section 2.5.3.

2.7.1 Bulge Formation

Bulges are formed either during galaxy mergers (major and minor) and by instabilities in the disk. In a major merger, the bulge of the final galaxy contains all the stars from the two merging galaxies, but in a minor galaxy the new galaxy's bulge is only populated by the stars in the satellite galaxy.

We use energy conservation and the virial theorem to compute the change in size of the bulge in both minor and major mergers (Guo et al., 2011):

$$\frac{GM_{new,bulge}^2}{R_{new,bulge}} = \frac{GM_1^2}{R_1} + \frac{GM_2^2}{R_2} + 2\alpha_{inter} \frac{GM_1M_2}{R_1 + R_2} \quad (2.23)$$

The left hand side of the equation represents the binding energy of the final bulge, the first two terms on the right represent the binding energy of the two progenitors, and the third term is the binding energy of the relative orbit of the two progenitors at the time of the merger. α_{inter} quantifies the binding energy invested in this orbit relative to that in the individual system, and is set to $\alpha_{inter} = 0.5$ as this has shown results of bulge sizes that are in agreement with observations in SDSS data. If either of the progenitors already has a bulge, the half mass radius is calculated assuming as exponential disk and an $r^{1/4}$ power-law bulge.

Disk Instabilities

Another important channel for bulge growth is through disc instabilities. These occur through the formation of bars in spiral galaxies which then buckle. The bar acts as a torque on the gas, funnelling both gas and stars towards the centre and they occur in galaxies where the self-gravity of the disk is dominant over the gravitational effects of the bulge and the halo. The criterion we use for disc instability is as follows (Guo et al., 2011):

$$V_{max} < \sqrt{\frac{GM_{*,d}}{3R_{*,d}}} \quad (2.24)$$

where $M_{*,d}$ and $R_{*,d}$ are the stellar mass and exponential scale-length of the stellar disk. V_{max} is the maximum circular velocity of the host dark matter halo containing the disk galaxy.

When the instability of this equation is met, we begin to transfer stellar mass from the disk into the bulge in an attempt to stabilise the disk. If the galaxy already has a bulge, the new material is assumed to merge with the existing bulge according to Equation 2.23, where $\alpha_{inter} = 2$. This higher value of α_{inter} is to account for the fact that the bulge and disk have no relative motion.

2.8 Calculating Observables

Galaxy formation models have access to a wealth of physical information about galaxies, such as their star formation rates, stellar masses, gas contents and metallicities, due to the way they have been built. Observers on the other hand, only have access to electromagnetic radiation in the form of a flux, or sometimes also a spectrum. Getting this type of

information from simulations is more difficult, but necessary if you want to make any worthwhile comparison of your model with the real world. Some of the important processes we use to get this information from our model are detailed below, including the assumed initial mass function of your stellar population, stellar population synthesis which links your stellar masses to predicted photometric properties and a model of dust extinction.

2.8.1 IMF

The Initial Mass Function (IMF) is a probability density function that describes the mass distribution of stars in a newly formed stellar population. It has taken slightly different forms over the years but was originally described as a simple power law giving us more low mass stars, and fewer high mass stars (Salpeter, 1955). More recently the IMF has taken the form of a broken power law (Kroupa, 2001) or a log-normal distribution (Chabrier, 2003), which has in both cases reduced the number of low mass stars than in Salpeter (1955). In the L-GALAXIES model, we adopt the Chabrier IMF:

$$\phi(M) = \begin{cases} K_1 M^{-1} \exp\left[\frac{-(\log(M) - \log(M_c))^2}{2\sigma^2}\right], & \text{for } M < 1M_\odot . \\ K_2 M^{-\alpha}, & \text{for } M > 1M_\odot . \end{cases} \quad (2.25)$$

where $M_c = 0.08M_\odot$; $\sigma = 0.69$; and K_1 and K_2 are normalisation constants that can be derived by assuming that the function is continuous, and that the total mass is normalised such that:

$$\int_{M_{min}}^{M_{max}} M\phi(M)dM = 1M_\odot \quad (2.26)$$

where M_{min} and M_{max} are the minimum and maximum mass of star you are considering, typically $0.1M_\odot$ and 100 (or 120) M_\odot respectively.

It is assumed in the model that the IMF is universal across space and time, though that is open to debate.

2.8.2 Stellar Population Synthesis

The photometric and spectroscopic properties of a galaxy are obviously determined by the constituent stars that make up that galaxy. Stellar population synthesis is a way, originally used by observers, of matching the observed fluxes or spectroscopic data with the population of stars that would produce that output. More recently it has been used by simulations the other way round, to turn the physical properties of a galaxy into

observable emission at various wavelengths, based on the mass, age and metallicity of the stellar population, assuming some initial mass function.

This is done by combining information of stellar evolutionary tracks (e.g. the PADOVA tracks (Girardi et al., 2000)) with the stellar spectra predicted for individual stars based on their atmospheres (e.g. Lejeune et al. (1997)), and then using isochrone synthesis to compute the spectral evolution of stellar populations (e.g. Charlot and Bruzual (1991); Bruzual A. and Charlot (1993)). This results in being able to calculate the spectral evolution of a stellar population for any star formation history within the model.

The choice of stellar population synthesis (SPS) model is critical on the final predictions of the observed galaxy properties. Two of the most commonly used SPS models today are the BC03 (Bruzual and Charlot, 2003) model, and M05 (Maraston, 2005), and L-GALAXIES has the option of using either as an option when running the model. In our work, and in the default L-GALAXIES options, we use M05 (Maraston, 2005).

2.8.3 Dust Extinction

Actively star-forming galaxies are known to be rich in dust. This can have a dramatic effect on their emitted spectrum since dust significantly absorbs optical/UV light while having a much milder effect at longer wavelengths. As a result, dust-dominated galaxies will generally have redder colours even if they are strongly star-forming. Therefore it is very important to include a model of dust extinction in the simulation in order to compare with observations.

We consider dust extinction separately for the diffuse interstellar medium (ISM) and for the molecular birth clouds (BC) within which stars form. The optical depth of dust as a function of wavelength is computed separately for each component and then combined as described below. We do not attempt to compute the detailed properties of the dust particles or the re-emission of the absorbed light.

Extinction by the ISM

The optical depth of diffuse dust in galactic disks is assumed to vary with wavelength as

$$\tau_{\lambda}^{ISM} = (1+z)^{-1} \left(\frac{A_{\lambda}}{A_V} \right)_{Z_{\odot}} \left(\frac{Z_{\text{gas}}}{Z_{\odot}} \right)^s \left(\frac{\langle N_H \rangle}{2.1 \times 10^{21} \text{ atoms cm}^{-2}} \right), \quad (2.27)$$

where we take the mean column density of hydrogen, $\langle N_H \rangle$, to be:

$$\langle N_H \rangle = \frac{M_{\text{cold}}}{1.4 m_p \pi (a R_{\text{gas,d}})^2} \quad (2.28)$$

Here $R_{\text{gas,d}}$ is the predicted cold gas disk scale-length, the 1.4 accounts for the presence of helium and $a = 1.68$ in order for $\langle N_H \rangle$ to represent the mass-weighted average column density of an exponential disk. Following the results in [Guiderdoni and Rocca-Volmerange \(1987\)](#), the extinction curve in Equation (2.27) depends on the gas metallicity and is based on an interpolation between the Solar Neighbourhood and the Large and Small Magellanic Clouds: $s = 1.35$ for $\lambda < 2000 \text{ \AA}$ and $s = 1.6$ for $\lambda > 2000 \text{ \AA}$. The extinction curve for solar metallicity, $(A_\lambda/A_V)_{Z_\odot}$, is taken from [Mathis et al. \(1983\)](#).

The redshift dependence in Equation (2.27) is significantly stronger than in previous versions of the model ($(1+z)^{-0.5}$ in [Kitzbichler and White \(2007\)](#) and $(1+z)^{-0.4}$ in [Guo and White \(2009\)](#)). The dependence implies that for the same amount of cold gas and the same metal abundance, there is less dust at high redshift. The motivation comes both from observations ([Steidel et al., 2004](#); [Quadri et al., 2008](#)) and from the assumption that dust is produced by relatively long-lived stars. However, it may also be that this redshift dependence has to be introduced as a phenomenological compensation for the excessively early build-up of the metal content in model galaxies (we discuss this in Section 3.5. In practice it has been included simply to give an approximate match to the low extinctions of high-redshift galaxies as inferred from their observed UV slopes ([Bouwens et al., 2012](#)), and to the UV luminosity function, as described in the next chapter.

Extinction by molecular birth clouds

This second source of extinction affects only young stars that are still embedded in their molecular birth clouds, for which we assume a lifetime of 10 Myr. The relevant optical depth is taken to be

$$\tau_\lambda^{BC} = \tau_\lambda^{\text{ISM}} \left(\frac{1}{\mu} - 1 \right) \left(\frac{\lambda}{5500 \text{ \AA}} \right)^{-0.7}, \quad (2.29)$$

where μ defines the fraction of the total effective-absorption optical depth contributed by the ambient ISM. It takes the value of 1/3 on average but has a substantial scatter ([Kong et al., 2004](#)). In our model, we take μ to be given by a random Gaussian deviate with mean 0.3 and standard deviation 0.2, truncated at 0.1 and 1.

Overall extinction curve

In order to get the final overall extinction, every galaxy is assigned an inclination, θ , given by the angle between the disk angular momentum and the z -direction of the simulation box, and a ‘‘slab’’ geometry is assumed for the dust in the diffuse ISM. For sources that

are uniformly distributed within the disk then the mean absorption coefficient is

$$A_{\lambda}^{\text{ISM}} = -2.5 \log_{10} \left(\frac{1 - \exp^{-\tau_{\lambda}^{\text{ISM}} \sec \theta}}{\tau_{\lambda}^{\text{ISM}} \sec \theta} \right), \quad (2.30)$$

Emission from young stars embedded within birth clouds is subject to an additional extinction of

$$A_{\lambda}^{\text{BC}} = -2.5 \log_{10} \left(\exp^{-\tau_{\lambda}^{\text{BC}}} \right). \quad (2.31)$$

The standard L-GALAXIES output does not attempt to model the attenuation of light by the intergalactic medium. However, this is done in post-processing for the lightcones published in the Millennium Run Observatory¹(Overzier et al., 2013). In this thesis, however, we neglect intergalactic attenuation.

2.9 MCMC Parameterisation

In order to sample the full multidimensional parameter space of the model, the free parameters are constrained using Markov Chain Monte Carlo (MCMC) sampling techniques. This enables the exploration of free parameters (within allowed regions) by calibrating with observations. Observations can be a variety of physical and derived quantities, and even be at different redshifts. L-GALAXIES adopts the Metropolis-Hastings algorithm for performing the MCMC calculations. A full MCMC chain requires the evaluation of many tens of thousands of models, which is unfeasible to perform for the full Millennium and Millennium-II simulations. Instead, the MCMC procedure is only performed on a representative subset of the merger trees. Once a best fitting model has been identified, it is implemented on the full volumes of the two simulations.

In the current model, the parameters were constrained using the abundance and passive fractions of galaxies at $z \leq 3$; and the model has successfully reproduced key observables at these redshifts, such as the luminosity and stellar mass functions. We highlight this fact in Figure 2.9, which is a reproduction of the SMF at $z \in \{0, 1, 2, 3\}$ from Henriques et al. (2015). The values of the free parameters constrained by the MCMC in the version of L-GALAXIES used in this thesis, can be found in Table 2.1.

¹The Millennium Run Observatory, or MRObs, allows you to observe the semi-analytic galaxy formation model through the use of ‘virtual telescopes’.

Table 2.1: The free parameters that are constrained in the model using MCMC.

Parameter	Description	Value	Units
α_{SF}	Star formation efficiency	0.025	
$M_{crit,0}$	Gas mass threshold	0.24	$10^{10}M_{\odot}$
$\alpha_{SF,burst}$	Star formation burst efficiency	0.60	
$\beta_{SF,burst}$	Star formation burst slope	1.9	
k_{AGN}	Radio feedback efficiency	5.3E-3	$M_{\odot}yr^{-1}$
f_{BH}	Blackhole growth efficiency	0.041	
V_{BH}	Quasar growth scale	750	
ϵ	Mass-loading efficiency	2.6	
V_{reheat}	Mass-loading scale	480	$km.s^{-1}$
β_1	Mass-loading slope	0.72	
η	Supernovae ejection efficiency	0.62	
V_{eject}	Supernovae ejection slope	100	$km.s^{-1}$
β_2	Supernovae ejection slope	0.80	
γ	Ejecta reincorporation timescale	3.0E10	yr
$M_{r.p.}$	Ram-pressure threshold	1.2E4	$10^{10}M_{\odot}$
R_{merger}	Major-merger threshold	0.1	
$\alpha_{friction}$	Dynamical friction	2.5	
y	Metal yield	0.046	

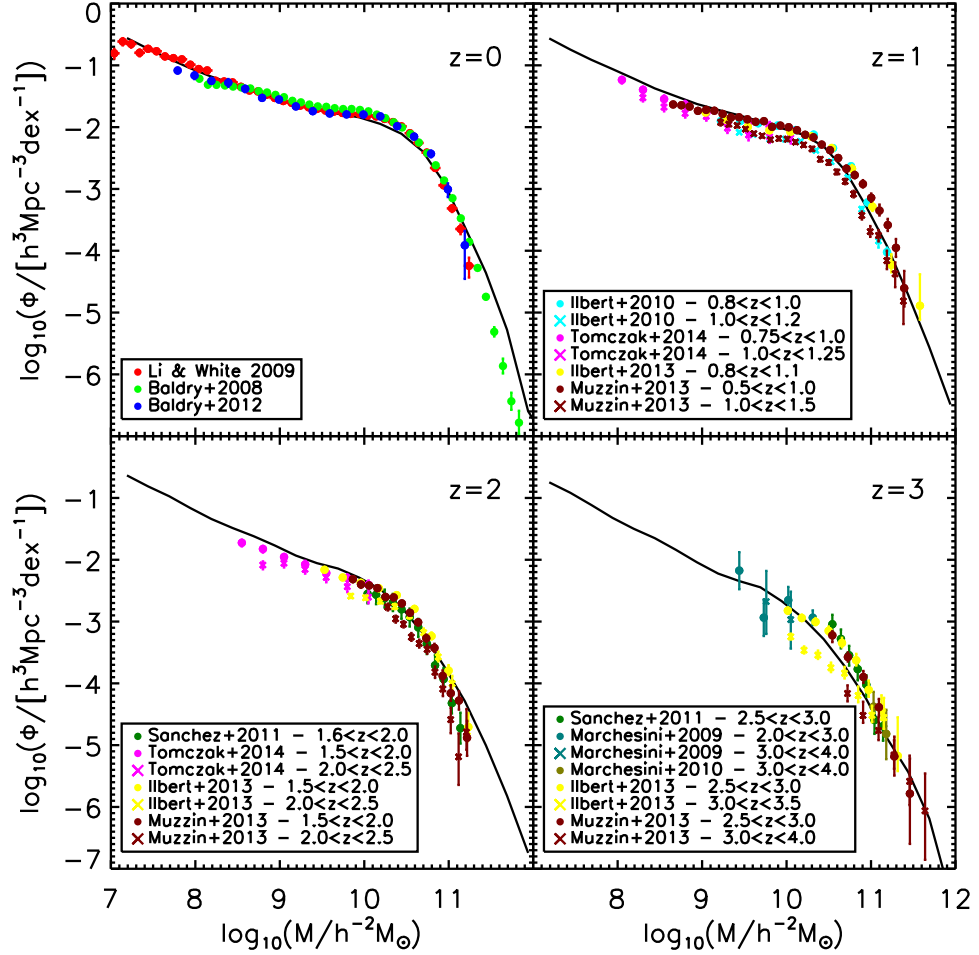


Figure 2.9: Predicted stellar mass functions at redshift $z \approx 0$ (top left); $z \approx 1$ (top right); $z \approx 2$ (lower left) and $z \approx 3$ (lower right). Solid black lines show the stellar mass functions predicted by the model. Observations are taken from several surveys; SDSS (Baldry et al., 2008; Li and White, 2009) and GAMA (Baldry et al., 2012) at $z=0$; and Marchesini et al. (2009), Spitzer-COSMOS (Ilbert et al., 2010), NEWFIRM (Marchesini et al., 2010), COSMOS (Domínguez Sánchez et al., 2011), ULTRAVISTA (Muzzin et al., 2013; Ilbert et al., 2013) and ZFOURGE (Tomczak et al., 2014) at higher redshifts.

Part II

Exploring the High-Redshift Universe with the L-Galaxies Semi-Analytic Model

Chapter 3

High-redshift predictions

The L-Galaxies SAM has had a lot of success over the past decade in predicting various properties of galaxies, such as the stellar mass and luminosity functions in both the local Universe and out to redshift $z=3$. However, the model has never really been explored at higher redshifts. In this chapter, we explore the model in the redshift range $z=4$ to $z=7$, but without altering any of the model parameters that are constrained at low redshift using MCMC. In that sense, results in this section can be considered predictions of the model.

The version of the L-Galaxies model used in this chapter is the one presented in [Henriques et al. \(2015\)](#), with the standard metal model but with post-processing of magnitudes switched off in order to get more accurate UV luminosities ([Shamshiri et al., 2015](#)). Many of the graphs and much of the text from this section were published in [Clay et al. \(2015\)](#).

3.1 Millennium vs. Millennium II

When presenting results at lower redshifts, such as those in [Henriques et al. \(2015\)](#), it is standard practice to make full use of both the Millennium simulations, so that we have the volume to find rarer objects from Millennium, but also benefit from the higher mass resolution for lower mass galaxies from Millennium-II. Merging the simulations and analysing the results together is acceptable so long as the simulations converge, which happens for Millennium and Millennium-II at a stellar mass of $\approx 10^{9.5} M_{\odot}$ at $z=0$.

When we began working on making high redshift predictions, we had to determine if we could use both simulations in the same way, and if so, where do they converge. [Figure 3.1](#) shows the stellar mass function (left) and UV luminosity function (right) at redshift $z=4$. Unfortunately, the simulations do not converge in either plot, with the

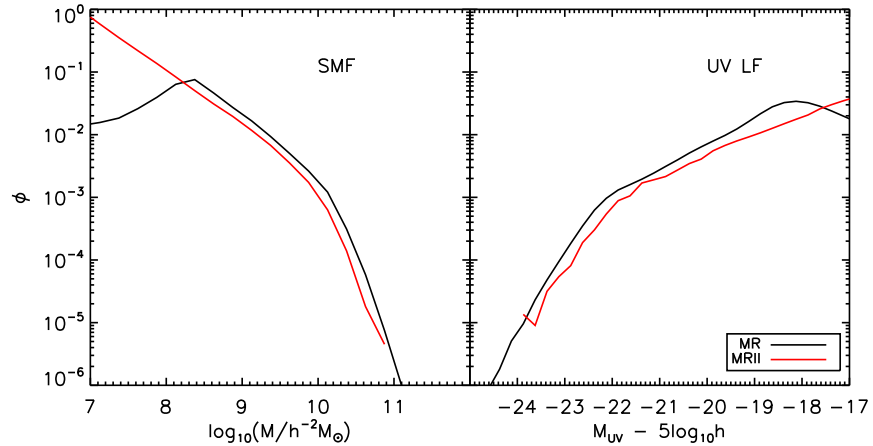


Figure 3.1: Predicted stellar mass (left) and UV luminosity functions (right) at redshift $z \approx 4$. The black lines show the predictions from the Millennium (MR) simulation, and the red line shows the predictions from the Millennium-II (MR II) simulation. The y-axis presents the number density, Φ , in units of $h^3 Mpc^{-3} dex^{-1}$ for the stellar mass function, and units of $h^3 Mpc^{-3} mag^{-1}$ for the luminosity function.

Millennium-II simulation being slightly lower in number density across all masses and luminosities. One possible reason for this is that gas feedback effects have more impact on the higher resolution simulation, which is having an impact on high-redshift galaxies.

For this reason, all the work presented in this chapter uses the Millennium simulation only.

3.2 Star formation

In this section we investigate the star formation rate (SFR) at redshifts $z \in \{4, 5, 6, 7\}$. Star formation is a property that comes out relatively easily from the model (see Section 2.3 for a description of the star formation process). However observationally, the SFR can be quite difficult to detect as it requires measurements in both the UV and far infrared or some measurement of the dust.

Figure 3.2 shows the star-formation-rate distribution function (SFR DF) as predicted by the model alongside measurements from Smit et al. (2012) (converted to our fiducial Chabrier IMF) and Duncan et al. (2014).

Comparing with the Smit et al. (2012) measurements at redshifts $z \approx 5 - 7$ we find generally good agreement. At these redshifts, the Duncan et al. (2014) measurements are generally higher than both the model and the Smit et al. (2012) results. This is partic-

ularly true for the most massive galaxies, though we note that the quoted observational uncertainties can be very large.

At $z \approx 4$, however, the model under-predicts the number of galaxies for $\log_{10}(\text{SFR}/h^{-2}M_{\odot}) < 1$ when compared to both sets of observations (which are consistent with one another at this redshift). The cause of the discrepancy is unclear, though may be a consequence of the model under-estimating the contribution to the SFR from merger-driven activity.

3.3 Stellar mass

The stellar mass is another physical quantity that can be obtained from the model relatively easily but observationally is quite difficult to measure, requiring many observations at varying wavelengths so you can fit the SEDs to model SEDs with known physical properties.

We present the Galaxy Stellar Mass Function (GSMF) at $z \in \{4, 5, 6, 7\}$ predicted by the model in Figure 3.3 alongside recent observational estimates at high-redshift from González et al. (2011) and Duncan et al. (2014).

It is important to first note that the observationally-derived mass functions presented in Figure 3.3 are inconsistent with each other at $z \sim 4-5$. One possible source (see Duncan et al. (2014) for a wider discussion) of this discrepancy is the effect of nebular emission which was included in Duncan et al. (2014) but not in González et al. (2011). Galaxies in the high-redshift Universe are expected (Wilkins et al., 2013a) and inferred (e.g. Smit et al., 2014) to exhibit strong nebular emission which can strongly affect the measured stellar mass-to-light ratios and thus masses (Wilkins et al., 2013a). The accuracy/precision of stellar mass estimates are also affected by the lower sensitivity and angular resolution of the *Spitzer*/IRAC imaging.

Given the above observational uncertainties, it is gratifying that the model predictions split the two observational measurements at $z = 4$. There is a hint that the change in slope at the “knee” of the mass-function ($M_{\text{knee}} \approx 3 \times 10^9 h^{-2} M_{\odot}$) may be sharper in the model than the observations, but the observational error bars are growing at this point and so it is hard to draw firm conclusions. As we move to higher redshifts, however, the model predictions and the observations gradually diverge as follows: (i) the normalisation at M_{knee} declines more rapidly with increasing redshift in the models than in the observations; (ii) the slope of the mass function above the knee is steeper in the models than in the observations.

The exact cause of these discrepancies is difficult to assess. One possibility is that it

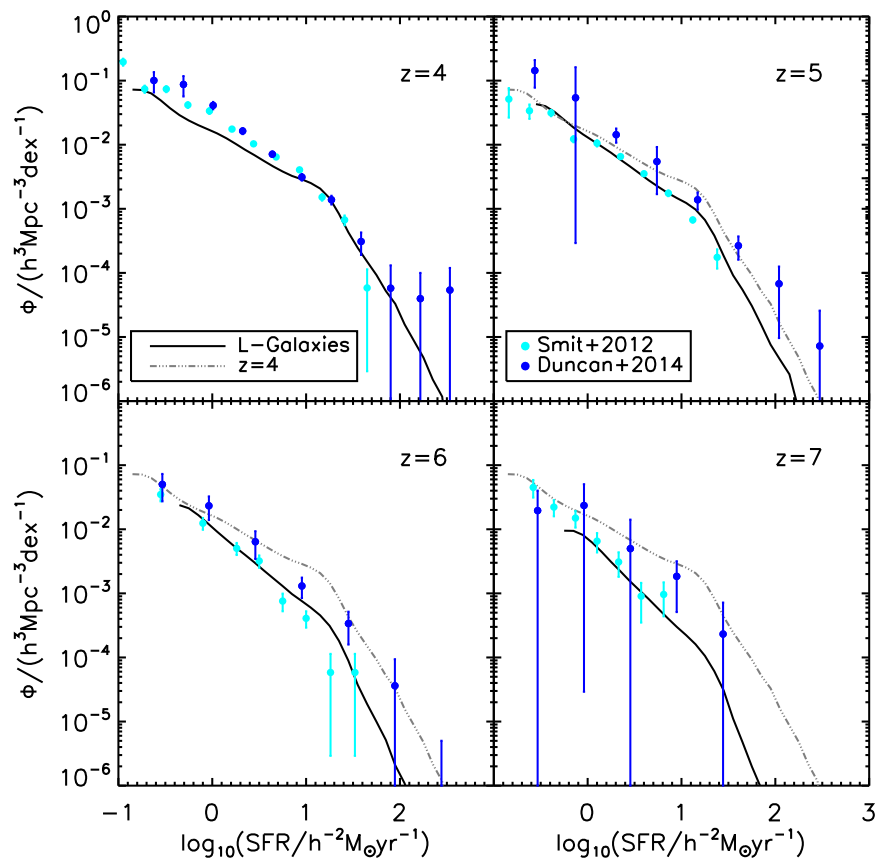


Figure 3.2: Predicted star formation rate distribution functions at redshift $z \approx 4$ (top left); $z \approx 5$ (top right); $z \approx 6$ (lower left) and $z \approx 7$ (lower right). In each instance we use the closest available snapshot from our L-GALAXIES run of $z=3.95$, 5.03 , 5.82 and 6.97 respectively. Solid black lines show the star formation rate distribution function predicted by the model. Our $z = 4$ star formation rate distribution function is repeated at higher redshifts as a grey dot-dash line for comparison. Observations are taken from [Smit et al. \(2012\)](#), converted to a Chabrier IMF, and [Duncan et al. \(2014\)](#).

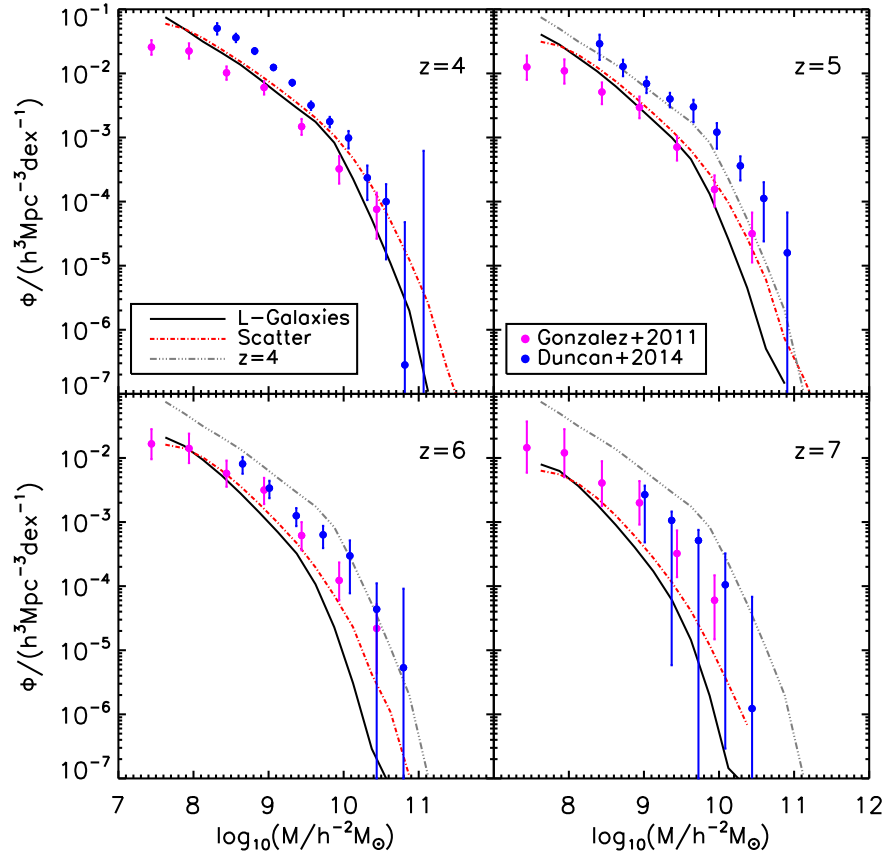


Figure 3.3: Predicted stellar mass functions at redshift $z \approx 4$ (top left); $z \approx 5$ (top right); $z \approx 6$ (lower left) and $z \approx 7$ (lower right). In each instance we use the closest snapshot available to use from our L-GALAXIES run of $z=3.95$, 5.03 , 5.82 and 6.97 respectively. Solid black lines show the stellar mass functions predicted by the model. To indicate the possible effect of uncertainties in the observational stellar mass determinations, we also show as a red dot-dash line the stellar mass function convolved with a Gaussian of standard deviation 0.3 dex. Our $z = 4$ stellar mass function is repeated at higher redshifts as a grey dot-dash line for comparison. Observations are taken from [González et al. \(2011\)](#), converted to a Chabrier IMF, and [Duncan et al. \(2014\)](#).

reflects a deficiency in the model; on the other hand it may reflect a systematic bias in the observations. This has been discussed at low redshift ($z = 0 - 3$) in Appendix C of [Henriques et al. \(2013\)](#). It seems probable that the uncertainties on the individual stellar masses could have been underestimated, and that can strongly boost the inferred number of galaxies in regions where the mass function is particularly steep. As an example of the possible magnitude of this effect, we show in [Figure 3.3](#) the result of convolving with a Gaussian of standard deviation 0.3 dex, similar to that required at low redshift. This largely reconciles the observed and predicted slopes of the mass function, but the normalisation remains too low at $z = 7$.

Recent hydrodynamic simulations, particularly ILLUSTRIS ([Vogelsberger et al., 2014](#)) and EAGLE ([Schaye et al., 2015](#)), have begun making predictions of observables at high redshift ([Genel et al., 2014](#); [Furlong et al., 2015](#)). Like L-GALAXIES, both ILLUSTRIS and EAGLE make predictions at high redshift by only using observational constraints at lower redshift. Both simulations are similar to ours in the prediction of the GSMF at $z = 6 - 7$ in that we all underpredict the abundance of high mass galaxies ($> 10^9 M_\odot$) at these redshifts, although EAGLE better matches the observations at $z = 5$ across the entire mass range. Whilst both L-GALAXIES and EAGLE match a similar shape to the observations, particularly finding good agreement with the slope and abundance for low mass galaxies, ILLUSTRIS predicts a slope that steepens with increasing redshift faster than what is observed, and over predicts the abundance of low mass galaxies at all redshifts.

3.4 sSFR - SM relation

The specific star formation rate (sSFR) is a measure of how quickly a galaxy is forming its stars. We present the sSFRs at $z \in \{4, 5, 6, 7\}$ of our galaxy population predicted by our model in [Figure 3.4](#) alongside recent observational measurements from [Salmon et al. \(2015\)](#). We represent the sSFR of individual galaxies by a 2D histogram; the solid line shows the median value predicted by our model, averaged over bins of 100 or more galaxies.

The observations are consistent with our model, particularly for galaxies of mass $M \approx 10^9 M_\odot$, across all redshifts. However the observations show a decline in the sSFR with increasing galactic stellar mass and we do not identify the same trend. Instead, all galaxies in our model have roughly the same level of activity, regardless of galactic stellar mass. This discrepancy is not surprising: given that the models match the observed SFR but under-predict the stellar masses of the largest galaxies, then we would expect this result.

The question remains as to whether the observations or the model is at fault, or a

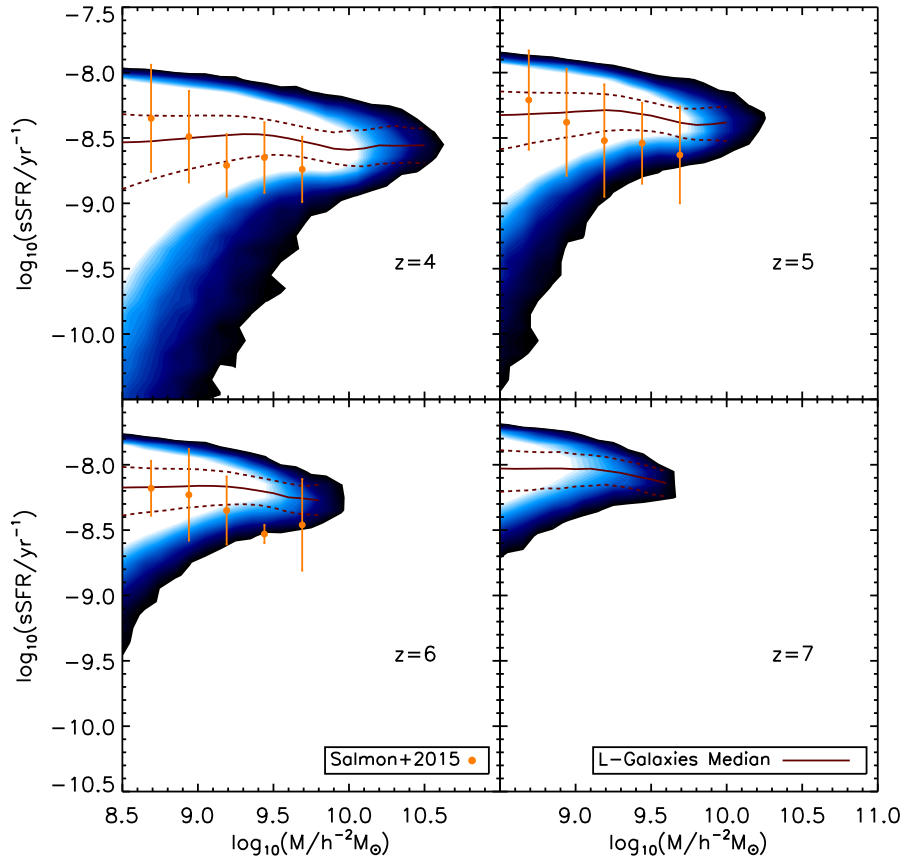


Figure 3.4: Predicted specific star formation rates ($sSFR = SFR/M_*$) at redshift $z \approx 4$ (top left); $z \approx 5$ (top right); $z \approx 6$ (lower left) and $z \approx 7$ (lower right). In each instance we use the closest snapshot available to use from our L-GALAXIES run of $z=3.95$, 5.03 , 5.82 and 6.97 respectively. The histogram density plot represents the L-GALAXIES galaxy population, with white representing the highest density, and blue representing the least. The solid line shows the L-GALAXIES median values, and the dashed lines show the 0.16 and 0.84 percentiles. The observations are taken from [Salmon et al. \(2015\)](#), with the points denoting the median value while the error bars reflect the scatter in the observations, rather than the uncertainty in the median.

combination of both. We could boost AGN feedback in the most massive galaxies in the model, but this would then reduce the bright end of the UVLF. Alternatively, as hinted in the previous section, the inferred masses of the highest-mass galaxies may have been boosted by observational scatter. At lower masses, there will be an observational bias towards the brightest galaxies, and so the median sSFR may be over-estimated.

3.5 Metals

Another important physical quantity to look at is the metallicity, a quantity that finds its way into many equations governing the physical processes of galaxy formation. It can be easily measured at low redshifts by taking the spectra of stars or galaxies, though it becomes more difficult to measure at higher redshifts.

Figure 3.5 shows the metallicity of the cold gas and of the stars, plotted against stellar mass, for all redshifts in $z \in \{0, 1, 2, 3, 4, 5, 6, 7\}$. These plots are made with the more simplistic metal model described at the start of Section 2.4, and not using the detailed chemical enrichment model that is used in later chapters of this thesis, as it was not implemented into the code at the time.

The metallicity of both the stars and cold gas at all redshifts look very similar across the mass range, particularly so in the case of stellar metallicity. The cold gas metallicity is less consistent, particularly at the high mass end at redshifts $z=0-3$, which is perhaps a consequence of higher feedback processes. A lack of evolution in metallicity with redshift tells us that creating a galaxy with a certain mass goes hand in hand with a fixed amount of metal pollution.

3.6 Varying the model of dust extinction

After looking at physical quantities such as the star formation and stellar mass functions, the next thing to do is to look at some derived properties of galaxy formation such as the UV luminosity function. This is something that the observers measure relatively easily, but computationally requires stellar synthesis models to convert the physical properties into spectral fluxes, based on the age, metallicity and mass of the stellar population (see Section 2.8.2 for more information on stellar population synthesis models). Furthermore, any intrinsic luminosity function needs to be converted into one that would be observed by applying a model of dust extinction (see Section 2.8.3 for more information on the dust extinction model we use in L-Galaxies). In the current model, the dust extinction applied

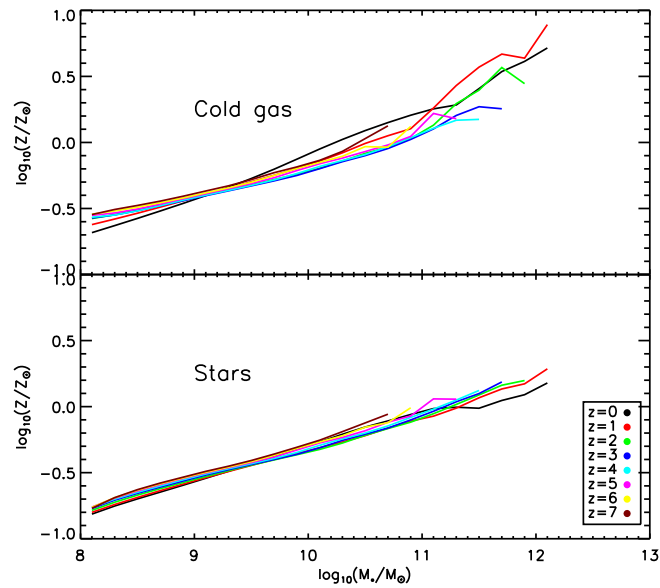


Figure 3.5: Plot to show the median metallicity of the cold gas (top) and the median metallicity of the stars (bottom), plotted against stellar mass. The coloured lines show the relation for different redshifts in the range $z \in \{0, 1, 2, 3, 4, 5, 6, 7\}$.

to each galaxy is proportional to the metallicity and the total cold gas mass, with an additional redshift dependence (Guo and White, 2009) of $(1+z)^{-0.4}$ to better reproduce observational values at higher redshifts.

When we first plotted the UVLF at high redshifts, we noticed there was a poor relation between the observed and simulated galaxy populations after applying a model of dust extinction. We also found that the intrinsic LF was above the observations, suggesting that the problem is with our model of dust extinction rather than a more fundamental problem with the physics of the model. Thus we began experimenting with a number of different dust extinction models.

Figure 3.6 shows the UV LF using a number of different models for dust extinction. The red solid line shows the dust extinction model as it was in the De Lucia and Blaizot (2007) version of L-GALAXIES. One method of changing the level of dust extinction at higher redshifts was to alter the redshift dependence, and we experimented with varying the exponent from -0.4 to -1 , and this model is shown by the solid green line. Another way is to accept that we may not be getting the metallicity correct at high-redshift, as seen in Figure 3.5 where the gas and stellar metallicities are fairly constant for a given stellar mass across all redshifts, which may suggest that we have too many metals in high-

redshift galaxies. So we experimented with changing the galaxy metallicities used in the calculation of the dust extinction to follow the prescription of [Maiolino et al. \(2008\)](#):

$$12 + \log(O/H) = -0.0864(\log M_* - \log M_0)^2 + K_0 \quad (3.1)$$

where we use the values given in the paper for the highest available redshift ($z=3.5$) for the calculation of dust extinction at redshifts $z=4-7$, with $\log M_0 = 12.87$ and $K_0 = 8.90$. We convert the $12 + \log(O/H)$ values into gas phase metallicities by assuming $12 + \log(O/H) = 8.69$ corresponds to Z_\odot . This model is shown by the blue line on the plot. The dashed black line shows the intrinsic luminosity function, before any model of extinction is applied.

Replacing our metallicities with those of [Maiolino et al. \(2008\)](#) using Equation 3.1 for the dust extinction calculations had little impact on the intrinsic LF at all, only noticeable in the brightest galaxies. The change in exponent of the redshift dependence from -0.4 to -1 provided a slightly better fit to observations, and is the version of the model we chose, as it had the best fit to the observations at $z=4-7$ without sacrificing the good fit we find at lower redshifts. We could have varied the exponent more to try find an ever better fit but we decided that we would begin working on changing this at a fundamental level instead, which is discussed in much more detail in the next part of this thesis.

3.7 UV Luminosity

We present the UV luminosity function predicted by our model in Figure 3.7 alongside recent observational estimations at high-redshift ([Bouwens et al., 2015](#); [Duncan et al., 2014](#); [Finkelstein et al., 2015](#); [Bowler et al., 2015, 2014](#)). The solid black line shows our prediction for the attenuated UV luminosity function; the attenuated UV LF at $z = 4$ is also shown on subsequent plots for comparison. The dashed line shows our intrinsic UV luminosity function, with no dust model being applied.

We find a good fit to the faint end of the luminosity function: $M_{UV} > -20$ for $z = 4-6$ and $M_{UV} > -19$ for $z = 7$. At brighter absolute magnitudes, the model counts fall below the observed ones. Note, however, that the raw counts, before dust attenuation, lie above the observations. Given that we saw a good fit in Section 3.2 between predicted and observed SFRs, then this points to a difference in the dust model between the two.

To better understand this, we quantify in Figure 3.8 the attenuation required (as a function of the intrinsic UV absolute magnitude) to reconcile the raw L-GALAXIES data with observations. We do this by comparing observed, $M_{\Phi, \text{obs}}$, and intrinsic, $M_{\Phi, \text{int}}$, absolute magnitudes below which we achieve a particular cumulative number density, Φ

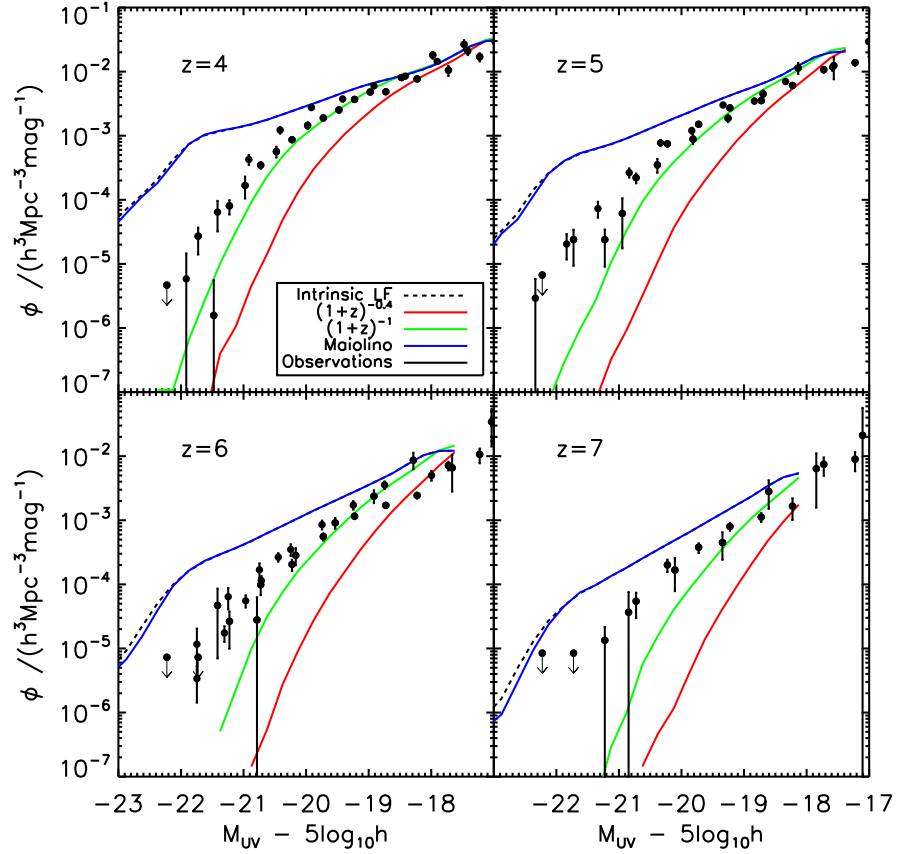


Figure 3.6: The UV luminosity function using various different dust extinction models. The dashed line shows the intrinsic luminosity function. The blue line shows a version of the model where we have replaced our model metallicities with observed values. The blue and green lines show variations on the redshift dependence for the dust extinction model currently used by the model. The black points show observational data from a number of sources (Bouwens et al. (2015), Duncan et al. (2014), Finkelstein et al. (2015), Bowler et al. (2015), Bowler et al. (2014)).

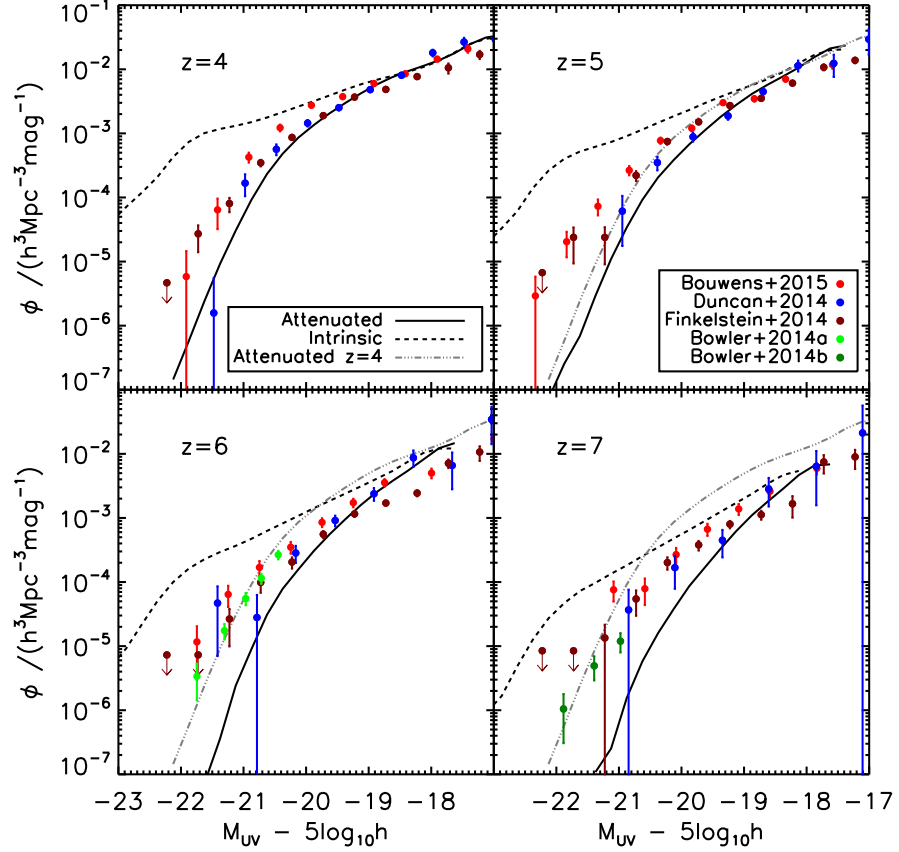


Figure 3.7: Predicted rest-frame (1500 Å) UV luminosity functions at redshift $z \approx 4$ (top left); $z \approx 5$ (top right); $z \approx 6$ (lower left) and $z \approx 7$ (lower right). In each instance we use the closest snapshot available to use from our L-GALAXIES run of $z=3.95$, 5.03 , 5.82 and 6.97 respectively. Solid black lines shows the L-GALAXIES prediction for the attenuated UV luminosity function using the dust extinction model outlined in Section 2.8.3. The dashed black line is the L-GALAXIES prediction of the intrinsic UV luminosity function, with no dust model applied. Our $z = 4$ attenuated UV luminosity function is repeated at higher redshifts as a grey dot-dash line for comparison. Observations are taken from Bouwens et al. (2015), Duncan et al. (2014) and Finkelstein et al. (2015), and at high mass from Bowler et al. (2015) ($z = 6$) and Bowler et al. (2014) ($z = 7$).

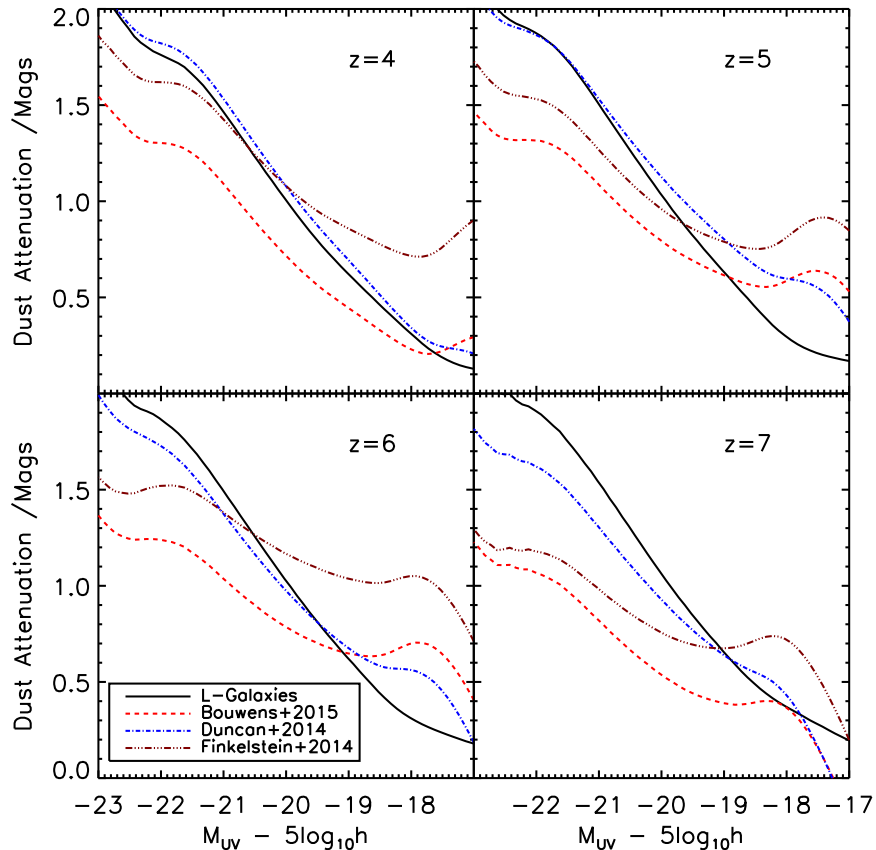


Figure 3.8: This figure shows the amount of dust attenuation required to move our intrinsic UV luminosity function (the dashed, black lines in Figure 3.7) to match different observational data sets (Bouwens et al., 2015; Duncan et al., 2014; Finkelstein et al., 2015), as a function of unattenuated absolute UV magnitude. The solid, black line shows the attenuation built into the L-GALAXIES model as described in Section 2.8.3.

of galaxies:

$$\Phi = \int_{-\infty}^{M_{\Phi}} \phi dM, \quad (3.2)$$

where ϕ is the usual differential number density of galaxies. The attenuation is then $A_{UV} = M_{\Phi, \text{obs}} - M_{\Phi, \text{int}}$.

The dust attenuation required to match the observations (as a function of the intrinsic absolute magnitude) is shown in Figure 3.8. The black, solid line shows the attenuation implemented in L-GALAXIES, as described in Section 2.8.3.

As expected, the built-in attenuation matches that from the Duncan et al. (2014) data fairly well. The other data sets show a shallower slope: the attenuation is reasonable, perhaps even under-estimated in the faintest galaxies, but is strongly over-estimated in

the brightest galaxies and increasingly so at high redshift.

It is important to stress that while we are presenting the results for all the objects within our simulation, observational samples (such as those employed by [Bouwens et al., 2015](#); [Duncan et al., 2014](#); [Finkelstein et al., 2015](#)), are biased and may not truly capture the full galaxy population at these redshifts. Indeed, a defining characteristic of the Lyman break technique, which is regularly used to identify galaxies in the high redshift universe, is that it preferentially selects blue rest-frame UV bright sources, i.e star forming galaxies with low UV dust attenuation ($A_{UV} < 2$). Very dusty galaxies, or those with little to no star formation would then be missed in typical Lyman break galaxy searches (e.g. HFLS3, a very dusty intensely star forming galaxy at $z \approx 6.3$ [Riechers et al., 2013](#)). The degree to which this is a concern at high-redshift is difficult to assess, largely due to the lack of sensitive far-IR and sub-mm imaging which is critical to identify heavily obscured systems.

Given the current observational uncertainties, we conclude that the simple, empirical dust extinction model currently built into L-GALAXIES does a reasonable job, although it could be refined to match particular data sets if required. This work inspired the next part of this thesis (Chapters 4 - 6), where we implement a more physically-motivated dust model: we also note that the current metals model used in this section has prompt recycling, and this could be an issue at these early times when the age of the Universe is just 1.5 Gyr at $z = 4$ and less than 1 Gyr for $z > 6$. Thus we implement the delayed chemical enrichment model from [Yates et al. \(2013\)](#) for the next part of this thesis. We discuss these changes to the model in Chapter 5.

3.8 Intrinsic UV continuum slope

Another derived quantity useful in observational astronomy is the measurement of the UV continuum (UVC) slope. This can be used to measure the amount of dust in high-redshift galaxies where the far-infrared is generally inaccessible. Observationally, the UV continuum slope is typically measured using two or more bands. It is difficult to measure and compare the UVC slope at different redshifts. Instead the continuum is categorised by a power law with slope β . Using our choice of *GALEX* FUV and NUV wavebands (148nm and 219nm respectively) from the model, the conversion from the $(FUV - NUV)_{AB}$ colour to β is:

$$\beta = C \times (FUV - NUV)_{AB} - 2 \quad (3.3)$$

where C is a conversion factor determined by convolving the two filters with a power law spectrum. For the *GALEX* filters, this conversion factor takes the value $C = 2.25$.

3.8.1 Redshift

Figure 3.9 shows the redshift evolution of the median intrinsic UV continuum slope for galaxies with $\log_{10}(\text{SFR}/M_{\odot}\text{yr}^{-1}) > \{0.0, 1.0\}$. There is initially a steady increase in the intrinsic UVC slope, with a peculiar bump at $z \sim 4$, before increasing at a more rapid rate towards $z = 0$. If you only include galaxies with a $\text{SFR} > 10M_{\odot}\text{yr}^{-1}$ then the redshift evolution changes slightly. While initially following the same evolution, including the peculiar bump at $z \sim 4$, from $z = 3$ onwards it evolves at a slightly higher rate towards $z = 0$. This is because galaxies that satisfy the higher star formation rate criteria will have younger, still star forming populations, and thus bluer intrinsic UVC colours. Comparing with observational constraints we find a good fit to the [Heinis et al. \(2013\)](#) results, particularly for $\text{SFR} > 1M_{\odot}\text{yr}^{-1}$ but also within the error range for $\text{SFR} > 10M_{\odot}\text{yr}^{-1}$. The [Casey et al. \(2014\)](#) results are consistent within their errors, and the [Álvarez-Márquez et al. \(2016\)](#) results are a few times too high when compared with our model. Our model does not fit the [Meurer et al. \(1999\)](#) results, though we note the inconsistency of the observations at this redshift and our model fitting the more recent observations, as well as a lack of error analysis.

We also compare our models results to the GALFORM SAM ([Wilkins et al., 2013a](#)) and MASSIVEBLACKII hydrodynamical simulation ([Wilkins et al., 2013b](#)). GALFORM shows a shallower redshift evolution in the intrinsic UVC than L-GALAXIES, though does fit the [Heinis et al. \(2013\)](#) result at $z \sim 1.5$ very well. Comparing with the more reliable results at $z \sim 0$, then GALFORM has an intrinsic UVC that is far too red. MASSIVEBLACKII can not currently be constrained by observations as the simulation has ended by $z \sim 5$, but currently lies between both SAMs at $z > 5$.

3.8.2 Star Formation Rate

Figure 3.10 shows the relationship between the intrinsic UV continuum slope and the star formation rate of galaxies at $z \in \{0.1, 2.0, 6.0\}$. The solid black line shows the median intrinsic UVC slope value in bins of SFR and the dashed line show the 0.16 and 0.84 percentiles. A 2D histogram shows the distribution of galaxies in our model, with a darker grey representing a higher number density of galaxies. The evolution at $z = 6$ is a subtle one, with the intrinsic UVC slope remaining relatively constant until $\log_{10}(\text{SFR}) > 1.4$

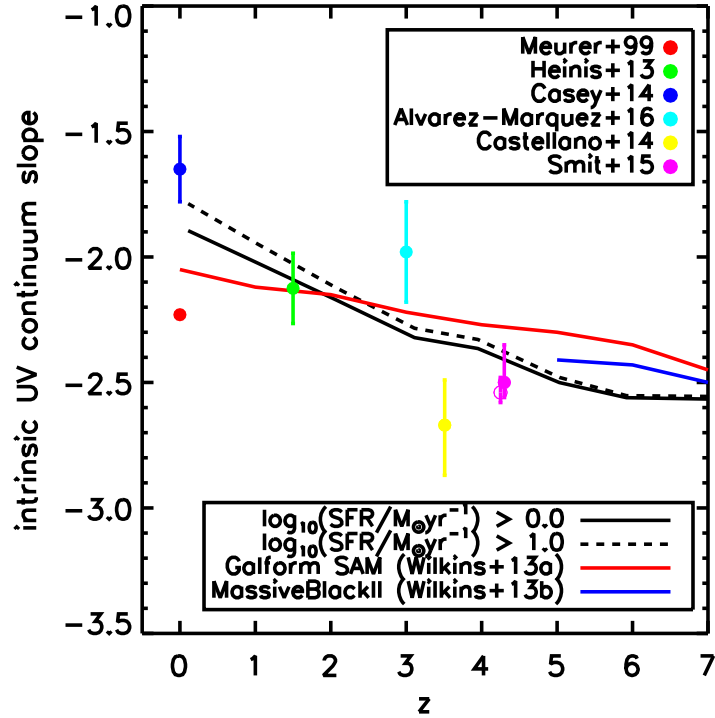


Figure 3.9: The redshift evolution of the median intrinsic UV continuum slope for model galaxies with $\log_{10}(\text{SFR}/M_{\odot} \text{yr}^{-1}) > 0.0$ (solid black line) and $\log_{10}(\text{SFR}/M_{\odot} \text{yr}^{-1}) > 1.0$ (dashed line). The coloured points with error bars show the observational constraints from Meurer et al. (1999), Heinis et al. (2013), Casey et al. (2014), Álvarez-Márquez et al. (2016) and Castellano et al. (2014). Two data points are shown from Smit et al. (2015), the open circle shows the results from photometrically derived redshift values, and the closed circle shows galaxy values with spectroscopically confirmed redshifts. We also compare our results with the GALFORM SAM (Wilkins et al., 2013a) and the MASSIVEBLACKII simulation (Wilkins et al., 2013b).

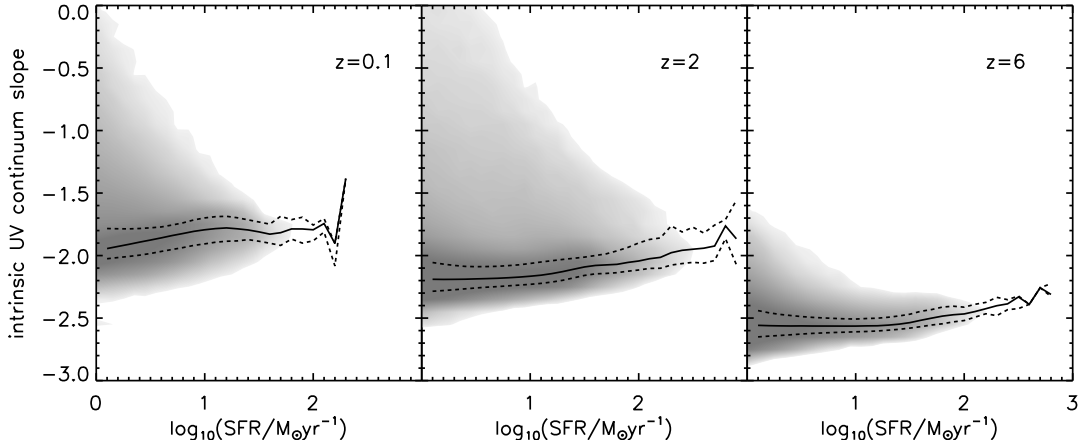


Figure 3.10: The relationship between the intrinsic UV continuum slope and the star formation rate of galaxies in our model at $z \in \{0.1, 2.0, 6.0\}$. The solid black line shows the median value (as a function of star formation rate) while the dashed lines denote the 16th – 84th centile range. The shaded region shows a 2D histogram representing the number density of galaxies.

when it starts to steadily increase for the most active star forming galaxies. At $z = 2$ we see a gradual shift towards redder colours with increasing SFR, though the spread of values is much larger than it was previously. We see a similar relation at $z=0.1$. We also note the increased normalisation towards bluer colours with time. The differences in the spread and in the evolution reflections the differences in the star formation histories and metal enrichment histories. We would expect an increase to bluer UVC colours with increasing SFR due to the actively star forming galaxies to have more young and hot stars. The decrease at $z = 0.1$ for the most star forming galaxies is peculiar, but perhaps an artefact that the only galaxies capable of achieving a new burst of star formation already have an older population shifting to redder colours.

3.8.3 Stellar Mass

The relationship of the intrinsic UV continuum slope with stellar mass is shown in Figure 3.11. The solid black line shows the median intrinsic UVC slope value in bins of SFR and the dashed line show the 0.16 and 0.84 percentiles. A 2D histogram shows the distribution of galaxies in our model, with a darker grey representing a higher number density of galaxies. At high redshift ($z \approx 6$) the relationship between the stellar mass and the intrinsic slope is similar to the relationship with star formation rate, with a steady increase

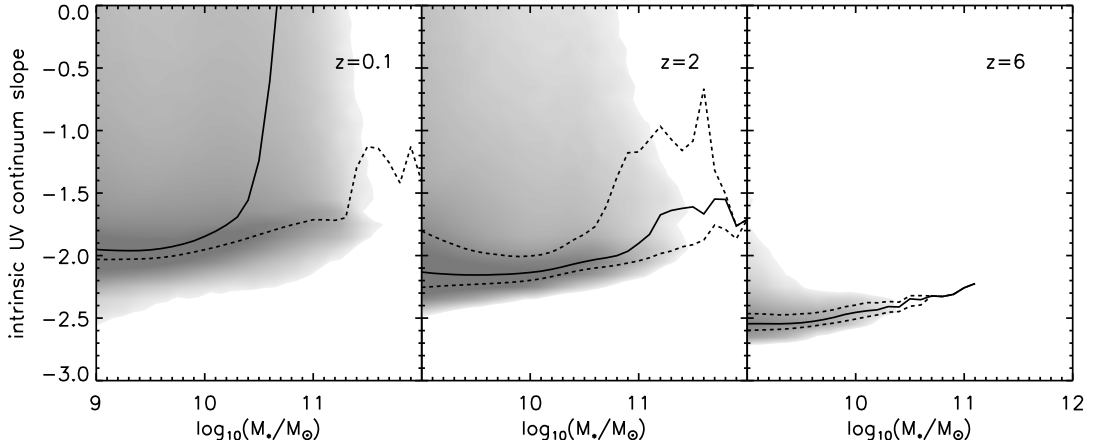


Figure 3.11: The relationship between the intrinsic UV continuum slope and the stellar mass of galaxies in our model at $z \in \{0.1, 2.0, 6.0\}$. The solid black line shows the median value (as a function of stellar mass) while the dashed lines denote the 16th – 84th centile range. The shaded region shows a 2D histogram representing the number density of galaxies.

in intrinsic UVC slope value with increasing stellar mass. This is not surprising as at high-redshift the star formation and stellar mass are highly correlated. At low-redshift, however there is strong evolution with stellar mass, such that the most massive galaxies have very red slopes on average. The distribution of slopes is also strongly asymmetric with a long tail to extending to very red intrinsic slopes. This is not surprising as these galaxies are essentially passively evolving.

3.9 Evolution of high-redshift quantities

To make it easier to see how the properties of our model galaxies change with time, we extract the model predictions from each of the four redshifts shown in Figures 3.2, 3.7, 3.3 & 3.4 and display them in single panels in Figure 3.12.

Concentrating first on the SFR (upper-left panel), we see the knee of the distribution remains relatively unchanged, at about $20h^{-2}M_{\odot}\text{yr}^{-1}$ over this period. However, the normalisation of the relation grows and the slope decreases, such that the comoving number density of galaxies with star-formation rates of $0.3h^{-2}M_{\odot}\text{yr}^{-1}$ is approximately constant, while that of higher star-formation rates in excess of $100h^{-2}M_{\odot}\text{yr}^{-1}$ grows by several orders of magnitude. As might be expected, a similar, but less pronounced, trend is seen in the UV LF, although the knee of the distribution is harder to discern.

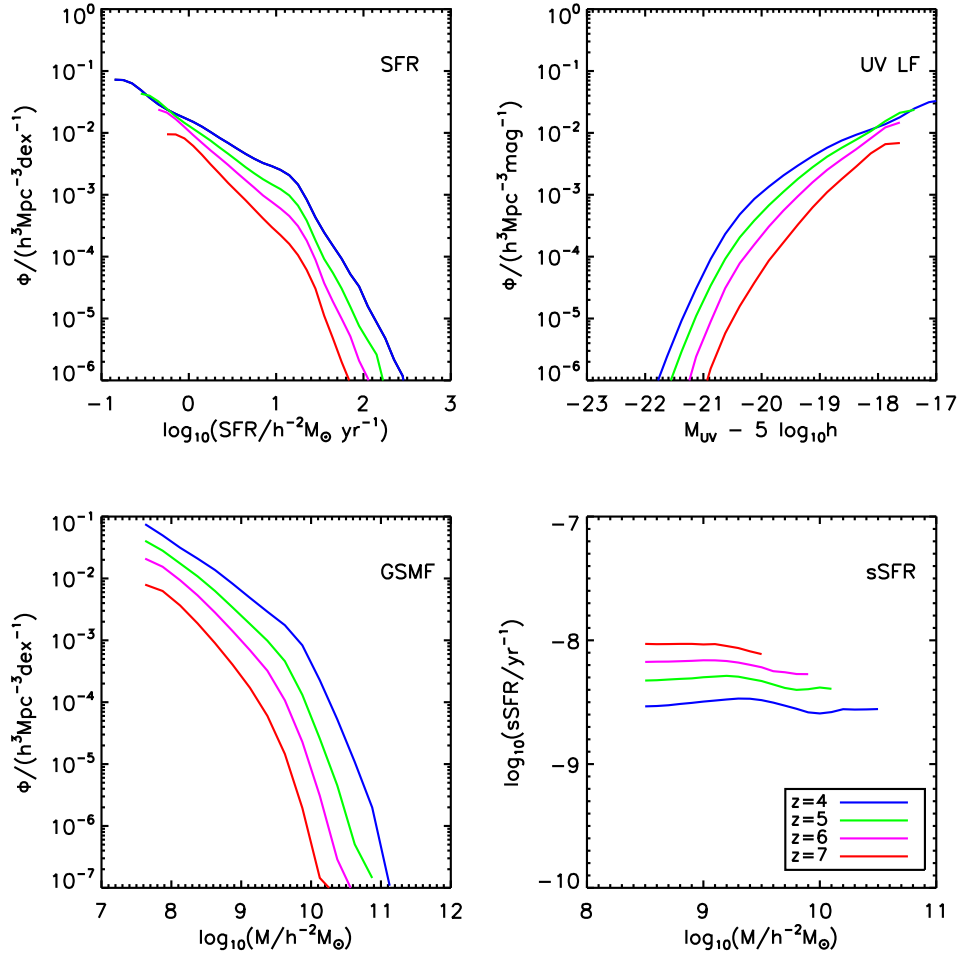


Figure 3.12: Plot to show the evolution of the stellar mass (top left); star formation rate (top right); UV luminosity function (lower left); and specific star formation rate (lower right) in the redshift range $z = 4 - 7$. The lines show the median values for each property at each redshift. In each instance we use the closest snapshot available to use from our L-GALAXIES run of $z=3.95, 5.03, 5.82$ and 6.97 respectively.

In contrast to the SFR DF, the galactic SMDF shows only a slight reduction in slope from $z = 7$ to $z = 4$. Consequently, the comoving number density of low-mass galaxies increases by about 1 dex over this time. This is reflected in the specific star-formation rate, which reduces by a factor of about 0.5 dex in the same period (as the sSFR is approximately independent of mass, this conclusion holds for individual galaxies, not just the population).¹

3.10 Conclusions

In this chapter we have used the L-GALAXIES semi-analytic model (Henriques et al., 2015) to explore its predictive power at high-redshift for certain observed properties, such as the star-formation-rate distribution function (SFR DF); UV luminosity function (UV LF); galactic stellar mass function (GSMF); and specific star-formation rates (sSFRs) of galaxies. Our conclusions are as follows:

- (i) We find a good fit to both the shape and normalization of the observed SFR DF at $z = 4 - 7$ (Figure 3.2), apart from a slight under-prediction at the low SFR end at $z = 4$, possibly caused by a lack of SFR contribution from merger-driven activity in our model.
- (ii) We find a good fit to the faint number counts for the observed UV LF (Figure 3.7). At brighter magnitudes, our predictions lie below the observations, increasingly so at higher redshifts.
- (iii) We change the redshift dependence of our dust extinction model from $(1 + z)^{-0.4}$ to $(1 + z)^{-1}$ in order to improve our observed luminosity functions at higher redshifts, particularly for the brightest galaxies.
- (iv) At all redshifts and magnitudes, the raw (unattenuated) number counts for the UV LF lie above the observations, and so we interpret our under-prediction as an over-estimate of the amount of dust in the model for the brightest galaxies, especially at high-redshift (Figure 3.8).
- (v) While the shape of our SMF matches that of the observations, we lie between the observations at $z = 4 - 5$ and under-predict at $z = 6 - 7$ (Figure 3.3). We note,

¹The age of the Universe roughly doubles over this period; thus the sSFR measured in terms of this age shows much less variation and even at $z = 4$ is sufficient to double the mass of a galaxy in less than a quarter of the age at that time.

however, that both sets of observations are inconsistent with one another, and have, at times, large errors attached to them.

- (vi) The sSFRs of our model galaxies (Figure 3.4) show the observed trend of increasing normalisation with redshift, but do not reproduce the observed mass dependence, indicating instead that galaxies of all masses the same level of activity. It is unclear as to whether this is caused by observational bias, or by an under-estimate of AGN feedback in the model.
- (vii) Both the stellar and cold gas metallicities are found to have little to no variation with redshift, instead depending on the stellar mass (Figure 3.5).
- (viii) Predictions of the UV continuum slope as a function of redshift (Figure 3.9), stellar mass (Figure 3.11) and star formation rate (Figure 3.10) are broadly in line with recent observational efforts at both low and high redshift.

In summary, the L-GALAXIES model has mixed success in reproducing observations at high redshift. It provides a reasonable match to both the SFR DF and the low-mass end of the SMF, but fails to show the observed mass-dependence of the sSFR. The predicted UV LF is highly-dependent upon an ad-hoc scaling with redshift of the dust model. The dust model is also dependent on the metallicity, which is shown to not vary with redshift in the model, which might not be true for real galaxies. In order to better predict the observed UV LF we need a better model for the dust extinction. To improve the metals we will use the detailed chemical enrichment modelling from Yates et al. (2013), which added delayed enrichment from stellar winds and supernovae, as well as metallicity-dependent yields and the tracking of eleven heavy elements (such as O, Mg and Fe). This has shown promising results in reproducing the mass-metallicity relation at $z=0$ but remains untested at higher redshifts, but should provide a more realistic prediction of what the metallicity of galaxies is at early times.

Additionally, we will add a physically motivated model of dust growth and destruction, which should help in better reproducing predictions of the observed UV LF by knowing the exact dust content of galaxies. Our work on this dust model is presented in part III of this thesis.

Part III

Detailed Dust Modelling with the L-Galaxies Semi-Analytic Model

Chapter 4

The Physics of Detailed Dust Modelling

The third part of this thesis presents our new physically motivated dust model that has been implemented into our semi-analytic model, L-GALAXIES. In Chapter 4, we discuss the relevant background to the physics of dust production and destruction. In Chapter 5, we discuss our implementation and testing of the dust model once fully integrated with L-GALAXIES, and finally in Chapter 6 we show our results once the model has been run on the full volumes of both Millennium and Millennium-II.

4.1 Introduction

Cosmic dust is by its very nature elusive to us, and thus remains a huge problem in astronomy due to its nature of obscuring the light from objects we wish to observe. As discussed in the previous chapter, it has been problematic in galaxy formation and evolution modelling for the reproduction of observed luminosity functions, but also plays a role in almost all areas of astronomy. Observations (and any derived physical quantities) are also vulnerable to the dust content of galaxies and the intergalactic medium, as dust reduces the luminosity of the source to an observer. Indeed, it is now thought that 30% of light in the universe has been reprocessed by dust grains at some point ([Bernstein et al., 2002](#)).

Dust has a long history in astronomy. On a clear night, the dust lanes of the Milky Way are clearly visible to the naked eye, and it is these same dust lanes that make it impossible for us to observe our own galactic bulge from here on Earth. Two hundred years ago, it was Hershel who first described the dark patches in the sky as ‘holes in the

heavens'. It was then a few years later with the advent of infrared astronomy, when these dark patches 'lit up', that we finally began to understand just how prominent it really is. It wasn't for another 100 years in 1930 when it was finally proven that these dark regions in our night sky are actually caused by solid dust particles in space (Trumpler, 1930), and since then the nature of interstellar grains has been the subject of active research, both in terms of the chemistry of their composition and also its effects in galaxy evolution and interstellar extinction.

Dust is now thought to consist of small, cold, micrometer sized grains typically composed of carbon or oxygen based compounds and though we do know that it exists, the true source and production mechanisms, whether it be from stars or something else, has continued to be debated in the literature. Observations in the far infrared have started to identify large dust masses in galaxies at very high-redshifts ($z=6-7$), suggesting that understanding the physics of dust production and evolution is critical to understanding galaxy formation and evolution. If we want a detailed dust model that works self-consistently across cosmic time, we need to model the various production and destruction processes and analyse the impact this has on the host galaxy.

In recent years, simulations of galaxy formation have started to implement detailed chemical enrichment models (e.g. Arrigoni et al., 2010; Yates et al., 2013), and a detailed modelling of the dust chemistry is the natural next step. However this has been slow on the uptake, particularly in cosmological models, perhaps due to a lack of observational constraints, particularly at high-redshift. Additionally, the physics of dust evolution is a more complicated process. The large number of possible dust molecules from the various combination of metals requires more consideration, and the weaker chemical bonds in dust grains than in metals means that dust is susceptible to additional growth and destruction processes. Arguably, the most important question is where and how dust grains are formed. Over the years, there have been two competing theories, the formation of dust in evolved stars, and the growth of new material in the interstellar medium.

Core collapse supernovae were actually thought to be important sites for the formation of dust long before the existence of any observational evidence supporting the idea (Cernuschi and Codina, 1967; Hoyle and Wickramasinghe, 1970). This changed with the explosion of supernova SN1987A which provided a wealth of information, including the first detection of dust in a supernova ejecta. The formation of dust has been shown to follow the formation of CO molecules in novae explosions (Gehrz and Ney, 1990) and this was observed for the first time in the ejecta SN1987A (Danziger et al., 1991). Dust first

manifested itself in the remnant of SN1987A (via the depletion of key refractory elements in the gas and an excess in the infrared light curve that occurred simultaneously with a drop in the UV (Bautista et al., 1995)), at around day 530 after the initial explosion.

It remains unclear to this day what the contribution of type Ia supernovae is to the dust content in galaxies. From a physical stand point, ejection velocities and the abundance of radioactive material are much higher in type Ia supernovae compared to type II, and this may inhibit the formation of dust (Gehrz et al., 1998). Observationally there has been no direct dust detection in the remnants of type Ia explosions (Borkowski et al., 2006). Other studies have found that while the formation of dust in SNIA remnants should in principle be possible via condensation in the iron rich expanding ejecta, most of this dust is likely to be destroyed as the ejecta reaches temperatures of 10^4 K (Wang and Mukherjee, 2006).

The other major source of stellar dust production is in the cool atmospheres of evolved stars, such as AGB and supergiant stars. These stars are shown to have the ideal environment necessary for the growth of dust grains (Sedlmayr, 1989). The presence of dust in these systems has been inferred from excess infrared emission, as well as from the extinction, scattering and polarization effects on the underlying UV photons. In addition to supernovae and giant stars, dust is thought to also come from Wolf-Rayet stars (Cohen et al., 1975; Williams et al., 1987) although these are thought to be rare, and Novae (Geisel et al., 1970) though their contribution is thought to be negligible (Dwek, 1998).

When considering cosmological timescales it is important to consider the role of different production mechanisms at different times. AGB stars are low to intermediate mass stars and therefore have main sequence lifetimes of the order billions of years, thus you would not expect them to be contributing heavily to the dust content until the universe is around 1Gyr old (although this has been shown to be heavily dependent on the assumed IMF, Valiante et al. (2009) for example found that this could actually be as early as 150Myr when using a Larson IMF). Type II supernovae on the other hand take place as the final act of a massive stars life, with a main sequence lifetime much shorter (tens to hundreds of millions of years). In this case, you would expect them to be influencing their environments on much shorter timescales, and thus potentially very important contributors to the dust content in very early, or the first, galaxies. With that said, it is currently unknown how efficient the production of dust in supernovae remnants really is. The shocks (and reverse shocks) produced by supernovae explosions are also one of the main destructive processes responsible for the removal of dust grains, and so the net production rate for supernovae, and the efficiency of this process, has long been debated

in the literature and is obviously vital to the understanding of dust production in galaxies at early times.

Evidence for grain destruction in the ISM has been found in the depletion of elements in high velocity clouds, with an observed trend of decreasing depletions with increasing cloud velocity (Spitzer and Morton, 1976; Cowie, 1978; Shull, 1978), suggesting that shocks are responsible for destruction of dust grains. Dwek and Arendt (1992) also inferred dust grain destruction in the general ISM from the infrared spectrum of shock-heated dust in supernovae remnants. Other processes that may destroy or alter dust grains include photo-evaporation and chemical explosions (de Boer et al., 1987; Savage and Sembach, 1996).

Another process that destroys dust is star formation, which removes dust grains from the ISM when they are incorporated into newly formed stars on a time scale of around 2.5 Gyr. This also happens to be the typical timescale for the replenishment of dust from stellar sources (Zhukovska et al., 2008) which would suggest a steady state in the absence of any other processes. Theoretical studies of grain destruction induced by supernovae shocks have found the process to have a typical timescale of the order 0.5 Gyr (Jones et al., 1996), which is much shorter than the typical timescale for replenishment and would suggest that galaxies would have a very low abundance of dust. However, we actually observe the opposite, high depletion rate of refractory elements in the gas phase of the ISM (e.g. Savage and Sembach, 1996; Jenkins, 2004). This suggests the need for another production mechanism in the ISM, that removes metals and converts them into dust, that must be on a very short timescale to counter the destruction of grains. The only possible site where this could happen would be the accretion of material onto dust grains inside the cold, dense, molecular clouds (Dwek and Scalo, 1980).

It was first suggested by Dwek and Scalo (1980) that dust grain growth inside molecular clouds could be a significant source of the dust mass in galaxies. However, molecular clouds must first be seeded with star dust (Draine, 1990). These dust particles provide the surface area on which to accrete atoms to grow more dust material inside the ISM. It has now been suggested that the bulk of ISM dust could be grown inside molecular clouds, even in high-redshift galaxies (Draine, 1990).

The importance and efficiency of all of these dust production and destruction mechanisms has long been argued in the literature and no consensus has been formed even when using models to try to reproduce observed dust masses in galaxies. Observations of galaxies at high redshift may help shed some light on what's happening, such as A1689z-D1

at $z=7.5$ and QSO SDSS J1148+5252 at $z=6.42$. The large dust masses in these galaxies at such early times has led some authors to propose that supernovae must be responsible (i.e. [Maiolino et al., 2004](#); [Sugerman et al., 2006](#); [Bianchi and Schneider, 2007](#)) but this would require around $1M_{\odot}$ of dust to be formed in each supernovae remnant to explain these observations ([Dwek et al., 2007](#)), which is around two orders of magnitude higher than what is observed in local supernovae remnants ([Draine and Fraise, 2009](#)). However, this is also contested, with some authors claiming that more dust can survive in remnants than previously thought ([Bianchi and Schneider, 2007](#)), such as in the local crab nebula where we find $0.24M_{\odot}$ of dust now, suggesting supernovae dust formation can be efficient ([Gomez et al., 2012](#)). [Michałowski \(2015\)](#) suggested that supernovae can produce the large dust masses detected in high redshift galaxies, so long as the dust is not destroyed with its injection into the ISM, which seems unlikely. [Dwek et al. \(2014\)](#) went further and said that supernovae are the only source of dust at redshifts $z>9$ where grain destruction rates are lower due to the low dust to gas ratios and that this changes towards lower redshifts as supernovae become net destroyers.

Other work has suggested that stellar sources are relatively insignificant ([Mattsson, 2015](#)) and that grain growth inside molecular clouds is by far the most dominant source of dust ([Dwek and Scalo, 1980](#); [Zhukovska et al., 2008](#); [Draine and Fraise, 2009](#); [Calura et al., 2010](#); [Valiante et al., 2011](#); [Gall et al., 2011](#); [Zhukovska, 2014](#); [Mattsson et al., 2014](#); [Michałowski, 2015](#)). Even at high redshifts, a small amount of dust from supernovae is sufficient to initiate growth in the ISM that is able to explain the observations ([Draine and Fraise, 2009](#)). Even if AGB stars dominate dust production at $z = 8-10$ ([Valiante et al., 2011](#)), high redshift observations could not be reproduced without a substantial contribution from grain growth. [Rowlands et al. \(2014\)](#) suggested you need either inefficient supernovae destruction, grain growth or a top heavy IMF to match the high-redshift observations. [Mancini et al. \(2015\)](#) suggested it may actually be a function of mass, with stellar sources dominating dust production in low mass galaxies, and grain growth dominating in high mass galaxies ($> 10^{9.5}M_{\odot}$) due to higher levels of metal enrichment.

Interestingly, two galaxies have been detected at approximately the same redshift ($z\sim 6.5$), one using ALMA and HST observations ([Ouchi et al., 2013](#)) named ‘Himiko’ and another using HerMES sub-mm observations ([Riechers et al., 2013](#)) named ‘HFLS3’. Despite being at the same redshift, and both undergoing a starburst, Himiko is observed to have a surprisingly low dust content and even may consist of mainly primordial gas. HFLS3 on the other hand is observed to be very dust-rich. Himiko is undergoing a triple

major event. Thus we are likely witnessing an early massive galaxy during a key period in its mass assembly close to the end of the reionization era. Whatever the source of dust, having two galaxies with very different dust content at the same redshift suggests the evolution from one regime to another must be very fast (Mattsson, 2015).

In the next section we describe in more detail the physics of dust production and destruction for all the main processes we consider in our model. These include the two stellar sources of dust, AGB stars and supernovae remnants; dust growth inside molecular clouds; and dust destruction induced by supernovae shocks.

4.2 Stellar sources of dust production

4.2.1 AGB yields

All low and intermediate mass stars (from $0.8 M_{\odot}$ to $\sim 8 M_{\odot}$) undergo an asymptotic giant branch (AGB) evolutionary stage when they leave the main sequence. During this phase, the stars pulsate and undergo mass loss due to stellar winds. It is in these stellar winds where we get the formation of dust grains. Inside the stellar winds, the collision of different particles causes growth via van der Waals forces or electromagnetic interaction. If the particle has a high enough bound energy, it is captured and becomes a building block of the solid (e.g. Gail and Sedlmayr (1987))

The type of dust produced by AGB stars is dependent on the stellar surface C/O abundance ratio, which can change during the star's evolution due to repeated third dredge events, where the surface convection zone extends down closer to the core where material has undergone nuclear fusion, resulting in fusion products being brought up to the surface and potentially changing the C/O ratio and the spectroscopic features of the star, and leading to different stellar wind properties (Ferrarotti and Gail, 2006).

The stars evolution in the C/O ratio depends on the initial mass of the star. In low mass stars ($< 1.5M_{\odot}$), the envelope is lost by stellar winds before the carbon abundance exceeds that of the oxygen abundance. For the very low mass stars, no third dredge up stage occurs. Stars in the mass range $1.5 < M_{\odot} < 4.0$ increase their carbon abundance over oxygen and become carbon stars, which then evolve further and lose their envelope in a stellar wind.

Intermediate mass stars (stars in a mass range $4.0 < M_{\odot} < 8.0$) convert any dredged up carbon into nitrogen via the CNO cycle. The oxygen is not affected by this process and thus the carbon abundance is much less than the oxygen. They do not become carbon

stars until most of their envelope is lost.

In [Ferrarotti and Gail \(2006\)](#), a model for the dust production rate of AGB stars was produced by combining simple models of dust formation in stellar winds with AGB evolutionary models, allowing them to determine the quantity and composition of dust produced via this process. They presented their results in the form of mass and metallicity dependent yield tables which we use in our model. More information on how we implemented these tables into our model is presented in the next chapter.

4.2.2 Supernovae yields

Massive stars ($M_* > 8M_\odot$) can also be factories for dust production. Similar to dust production in AGB stars, dust can also be formed in the stellar winds of Red Supergiants which is an evolutionary stage for stars in the mass range $8M_\odot \leq M_* \leq 40M_\odot$. However, it is expected that any dust formed during this process is destroyed by the shock wave of the subsequent core collapse supernovae explosion ([Zhukovska et al., 2008](#)). The most massive stars ($M_* > 40M_\odot$) are able to form dust in the massive shell ejections caused by giant eruptions during the Luminous-Blue-Variables (LBV) phase ([Smith and Owocki, 2006](#)). There is currently not enough information on these objects to include them in dust chemistry models, and it is unknown how much dust (if any) survives the subsequent supernovae explosion as with the red supergiants, though there is some evidence that the expansion velocity from giant eruptions may be much higher than with stellar winds and the dust may therefore survive.

Another type of dust production is from Wolf-Rayet stars. These are massive stars undergoing huge mass loss in their last evolutionary stage before they go supernova. Their contribution to dust production is presumably negligible due to them being rare ([Marchenko et al., 2006](#)), and the supernovae explosion occurring very shortly after this stage which destroys most of the dust anyway ([van der Hucht, 2006](#)).

The last source of dust production from massive stars is in core collapse supernovae remnants, where dust is assumed to be produced in the same way it is produced in stellar winds described above. Unfortunately, no modelling has been done on the production rate of dust in high mass stars, and thus their values are constrained using observations of local supernovae remnants.

4.3 Dust destruction

The destruction of dust grains is mainly caused by high velocity supernovae shocks with velocities exceeding 100 km s^{-1} (Jones et al., 1996; Seab, 1987). The dust grains are bombarded with particles (usually He^+) energised by the shock which causes destruction of the dust grains by the ejection of particles due to the bombardment, a process known as sputtering.

McKee (1989) described the average galactic timescale for destruction of a dust species j by supernovae as:

$$\tau_{dest} = \frac{M_{ISM}}{M_{j,cleared} f_{SN} R_{SN}} \quad (4.1)$$

where M_{ISM} is the total mass of the ISM, R_{SN} is the supernovae rate, f_{SN} is the fraction of supernovae that explode within the galactic plane and destroy dust and $M_{j,cleared}$ is the mass of cold gas that is totally void of a particular species of dust that is destroyed by an average supernovae.

4.4 Dust growth

Dust growth in molecular clouds is an important aspect in dust chemistry models and is necessary in order to reproduce both high redshift dust mass observations and the high observed depletions of elements in the ISM (e.g. Jenkins, 2004). Dust growth occurs when particles are accreted onto existing grains and is thus favoured to happen in denser environments (in order to have more interactions) and cooler environments (so that collisions do not destroy or fracture grains). Thus a perfect environment for dust grain growth is inside the cold dense environment of molecular clouds. As particles must be accreted onto existing dust grains, molecular clouds must first be seeded by dust grains from stellar sources in order to start the process.

Derivation of the dust growth equation and accretion timescale

We derive the fractional change of dust and accretion timescale from first principles. We take the rate of accretion of an atom onto a dust grain to be:

$$\nu_j \sigma_g v n_d \quad (4.2)$$

where ν_j is the ‘stickability’ of an atom onto a dust grain, σ_g is the cross section for dust grain interactions, v is the velocity and n_d is the number density of dust grains.

The mass of an element j , M_j , decreases by the rate at which it accretes onto dust grains, and can be described by:

$$\frac{1}{M_j} \frac{dM_j}{dt} = -\nu_j \sigma_g v n_d \quad (4.3)$$

with the number density of dust grains described as:

$$n_d = \frac{M_d}{m_g V} \quad (4.4)$$

where M_d is the dust mass, m_g is the typical grain mass and V is the volume. If we substitute the number density into the above equation we get:

$$\frac{dM_j}{dt} = -\nu_j \sigma_g v \frac{M_d}{m_g V} M_j \quad (4.5)$$

If we assume that the ‘stickability’ of element j , ν_j is the same for all elements, then we can replace ν_j with ν , and then sum over all different elements to get the total loss of all elements onto dust grains:

$$\frac{d \sum M_j}{dt} = -\nu \sigma_g v \frac{M_d}{m_g V} \sum M_j \quad (4.6)$$

We can define M_{zd} as the total mass in metals both locked up in dust and in the diffuse gas, so that:

$$M_{zd} = \sum_j M_j + M_d \quad (4.7)$$

and then

$$-\frac{dM_d}{dt} = -\nu \sigma_g v \frac{M_d}{m_g V} (M_{zd} - M_d) \quad (4.8)$$

Let $f_d = M_d / M_{zd}$, be the fraction of condensible elements locked up in dust. With some rearranging we find:

$$\frac{df_d}{dt} = \frac{\nu \sigma_g v}{m_g} \frac{M_{zd}}{V} f_d (1 - f_d) \quad (4.9)$$

We can define the first set of terms on the right hand side as a timescale such that:

$$\tau_{acc} = \left(\frac{m_g}{\nu \sigma_g v} \frac{V}{M} \right) \left(\frac{M}{M_{zd}} \right) \quad (4.10)$$

where we add a mass, M , to the top and bottom. The terms in the first set of brackets represent the properties of the dust grain, whereas the properties on the right represent

the properties of the growth environment. This now gives us an ordinary differential equation:

$$\frac{df_d}{dt} = \frac{f_d(1 - f_d)}{\tau_{acc}} \quad (4.11)$$

that can be solved to find:

$$f_d(t) = \frac{C e^{t/\tau_{acc}}}{1 + C e^{t/\tau_{acc}}} \quad (4.12)$$

where C is a constant. Using the initial condition that at $t = 0$ we have some initial dust mass; $f_d(0) = f_{d0}$, we can rearrange this to find:

$$f_d(t) = \frac{f_{d0}}{f_{d0} + (1 - f_{d0})e^{-t/\tau_{acc}}} \quad (4.13)$$

This equation now describes the fraction of condensible material that will be converted into dust grains at time t . Thinking about this equation we can see that it makes sense. At time $t=0$, we see that $f_d = f_{d0}$; while for larger times ($t \gg \tau_{acc}$) we find that f_d tends towards $f_d = 1$, which would represent the total condensation of metals onto dust grains.

The environment most favourable for grain growth to occur is inside cold and dense molecular clouds. At the instant a molecular cloud is formed, the cloud will inherit the dust content of the ISM. If we take the initial condensation value to be f_{d0} , the effective dust mass return for an individual molecular cloud would be:

$$M_{grown,MC} = (f_d - f_{d0})M_{zd,MC} \quad (4.14)$$

where $M_{zd,MC}$ is the total amount of condensible elements in metals or dust available for accretion inside that one molecular cloud.

The probability distribution function for the lifetime of a molecular cloud can be modelled as a Poisson distribution:

$$p(t) = \frac{1}{\tau_{exch}} e^{-t/\tau_{exch}} \quad (4.15)$$

Here it is assumed that cloud destruction occurs at random with a mean lifetime τ_{exch} . We take the probability that the cloud has a lifetime less than t to be:

$$P(t) = \int_0^t p(t)dt = \int_0^t \frac{1}{\tau_{exch}} e^{-t/\tau_{exch}} dt \quad (4.16)$$

The fractional change of material to the ISM occurs at the end of the molecular cloud lifetime, and can be taken to be (assuming a constant cloud production rate):

$$f_{d,ret}(t) = \int_0^t p(x) f_d(t-x) dx = \int_0^t \frac{1}{\tau_{exch}} e^{-x/\tau_{exch}} \frac{f_{d0}(t-x)}{f_{d0}(t-x) + (1-f_{d0}(t-x))e^{-x/\tau_{exch}}} dx \quad (4.17)$$

This equation describes the fractional change of material returned to the ISM, for a molecular cloud that was born at time $t=0$ and which inherited the dust fraction of the ISM, which occurred at a time $(t-x)$ ago.

Zhukovska et al. (2008) arrived at the same equation, but from a different derivation (thus a different accretion timescale). They found that the dust production by clouds is nearly independent of the details of the growth process within the clouds and is almost exclusively determined by the cycling frequency between the clouds and the ISM. They found a good analytic fit to integrating Equation 4.17 for a full range of t_{acc} and t_{exch} values to be:

$$f_{d,ret} = \left[\frac{1}{f_{d0}^2 (1 + \tau_{exch}/\tau_{acc})^2} + 1 \right]^{-0.5} \quad (4.18)$$

This approximation requires the assumption that $t \gg$ than the maximum possible values for τ_{exch} and τ_{acc} so that the upper limit on the integral in Equation 4.17 can be replaced by ∞ and so f_{d0} is essentially constant over timescales of the order $t \gg \max(\tau_{exch}; \tau_{acc})$. In our tests, we found that this equation further requires that $\tau_{exch} \gg \tau_{acc}$ or else f_d plateaus at the wrong value.

We can now expand Equation 4.14 to get the total dust mass return from all molecular clouds:

$$\dot{M}_{d,grown} = \frac{1}{t_{exch,eff}} (f_{d,ret} - f_{d0}) M_{zd} \quad (4.19)$$

where we have defined an effective timescale for the cycling of material through molecular clouds.

$$\tau_{exch,eff} = \tau_{exch} \frac{1 - f_{mol}}{f_{mol}} \quad (4.20)$$

where f_{mol} is the molecular gas mass fraction.

Final equations to solve

This leaves us with the following equations to describe the evolution of element j from metals into dust via accretion:

$$\dot{M}_{j,d,grown} = \frac{1}{\tau_{exch,eff}} (f_{j,d,ret} - f_{j,d0}) (M_{j,metals} + M_{j,dust}) \quad (4.21)$$

$$f_{j,d,ret} = \left[\frac{1}{f_{j,d0}^2 (1 + \tau_{exch}/\tau_{acc,j})^2} + 1 \right]^{-0.5} \quad (4.22)$$

$$\tau_{acc,j} = \frac{m_g}{\nu \sigma_g \nu} \frac{V}{M} \frac{M}{(M_{j,metals} + M_{j,dust})} \quad (4.23)$$

These are the equations that we need to solve in our SAM, and the implementation of these equations and the subsequent testing and results are described in the next two chapters.

4.5 Converting observations into physical quantities

In order to compare our model with observational data, it is important to understand how observers calculate the dust properties of their galaxy populations. Observers only really have access to the luminosity of a galaxy, and sometimes also its spectrum. In order to get a dust mass you need observations of a galaxy in several different wavebands in order to produce a spectral energy distribution across as much as the electromagnetic spectrum as possible, which can then be compared with theoretical models.

Derivations of physical dust quantities are generally done using SED modelling. This involves fitting the observed SED to some template library which was built assuming specific properties of the dust, most importantly a dust temperature which is used to calculate a modified blackbody (greybody) curve. More complicated models can also take into account other microscopic dust properties, such as the dust composition and grain size (Zubko et al., 2004). These models typically assume that dust properties and conditions are uniform throughout the galaxy (Rémy-Ruyer et al., 2015), or that the dust properties in all galaxies at all times are similar to those in local models (Santini et al., 2014).

At higher redshifts, far infrared (FIR), millimetre(mm) and submillimetre(sub-mm) observations are generally only possible in extreme galaxies, such as those undergoing starbursts or heavy AGN activity. Though mm and sub-mm observations have still been shown to be powerful tools in determining how the dust and gas is evolving in high-redshift galaxies, with molecular transitions such as CO and the continuum emission been used to determine the properties of the gas (e.g. Greve et al. (2005), Tacconi et al. (2006), Scott et al. (2011)) and dust (e.g. da Cunha et al. (2008)) respectively. Further complications

arise from the further heating of dust at higher redshifts due to the CMB (da Cunha et al., 2013), and the lack of many observational data points in the FIR (often only one point) mean a dust temperature can't be calculated in the typical way, and one must be assumed. The assumption of a dust temperature can lead to differing dust masses by up to an order of magnitude (Schaerer et al., 2015). Still, observations using ALMA and the Plateau de Bure Interferometer (PdBI) have been used to provide upper limits on the dust content of high-redshift galaxies (e.g. Kanekar et al., 2013; Ouchi et al., 2013; Ota et al., 2014; Schaefer et al., 2015; Maiolino et al., 2015). The dust content of the $z=7.5$ Lyman break galaxy A1689-zD1 (Watson et al., 2015) suggests a dust mass of $4 \times 10^7 M_{\odot}$, highlighting the need for efficient dust growth mechanisms when the universe is less than 1Gyr old (Mancini et al., 2015). Though these galaxies may not be representative of the 'normal' galaxy population, they help us constrain the dust formation process (Popping et al., 2016).

An alternate method for calculating dust properties is by using Gamma Ray Bursts (GRBs). GRBs are massive stellar explosions observed to have synchrotron spectra, thus any absorption lines must originate from the medium between us and the GRB (Wiseman et al., 2017). They are also useful tools over a large range of redshifts due to their extreme luminosities. Unlike the typically 'extreme' high-redshift galaxies detected in the FIR or mm/sub-mm, GRBs can be detected in galaxies of any physical properties (e.g. Fynbo et al., 2008; Mannucci et al., 2011; Krühler et al., 2015; Cucchiara et al., 2015). Using UV and optical absorption line spectroscopy, it is possible to measure the dust and metal column densities, and thus the dust to metal ratio (e.g. De Cia et al., 2013; Wiseman et al., 2017). It is not possible to calculate dust masses themselves without assuming a column length. This is not a problem for the dust to metal ratio calculation as any assumed column length would cancel out. The caveat to using this method for deriving dust properties is that you don't always have knowledge of the location of the GRB inside a galaxy. If the GRB goes off inside a heavy star-forming region full of dust, this will give more biased results as opposed to going off in a region void of dust, for example.

It should be noted that some observational studies such as Santini et al. (2014) found that galaxies with the same physical properties (such as stellar mass and star formation rate) do not show any significant evolution in terms of dust content with redshift. However, different redshifts are generally populated by galaxies of different star formation and stellar mass properties, hence different dust masses in general. If anything, their observations showed a slightly higher dust content in higher redshift galaxies, perhaps as a consequence

of the higher ISM content in those galaxies.

Chapter 5

The testing and implementation of a physically motivated dust model

This chapter of the thesis is dedicated to the implementation, testing and challenges introduced by implementing a physically motivated dust model into L-GALAXIES. It includes a description of the equations that were used in producing the new dust model, any alterations to the existing L-GALAXIES model, as well as the testing we performed in order to ensure the model was working as intended.

5.1 General considerations

Some of the more general challenges when implementing the new dust model into L-GALAXIES were how we would keep track of the new information that would be introduced, and how we would treat the dust on a physical level inside the code. As explained in Chapter 2, the detailed chemical enrichment model keeps track of individual metal species separately, but they remain a component of the gas phases at any given time. In order to conserve mass in the simplest way possible, it would be easiest for us to deal with dust in exactly the same way, thus any dust is also part of the total gas mass. One thing we did have to consider though, was whether the dust mass would also be a portion of the metal mass, or whether we would treat the dust and metals as totally separate entities. Motivated by observations, we decided to track dust separately from metals, as we originally thought that the observed gas phase metallicity measurements generally ignore dust content. We later learnt that observers generally correct for dust by assuming some depletion factor of metals onto dust, but opted not to change the code at that point. This means that any dust production or destruction calculations in our model require a

corresponding calculation to take place on the metals in order to conserve mass (as dust is created from metals).

In terms of keeping track of the new information introduced by the dust model, any detailed dust model needs to be compatible with the underlying chemical enrichment model, which in our case keeps track of 11 individual elements (H, He, C, N, O, Ne, Mg, Si, S, Ca and Fe). Many dust models in the past have chosen to model dust based on species, such as silicate or carbonate based dust, rather than by metal abundance (e.g. [Zhukovska et al. \(2008\)](#)). In our model, AGB dust production comes from mass and metallicity dependent yield tables (we discuss this in more detail below) and these yield tables also give their output in the form of a mass of a specific dust species returned, rather than the individual element make up. When we originally started working on the model, we decided to treat the dust in the same way, with each galaxy storing the amount of dust held for silicates, carbonates, silicon carbides and iron dust, with the sum of these four types representing the total dust mass. However, this ended up causing a number of problems, such as with the conservation of elements (elements could change type when converted into dust and later destroyed back into metals). In the end, we decided to track the dust as a function of its element composition instead, any conversions required between dust species and element abundance (such as when converting the AGB dust yield tables) were done assuming the element mass percentages that make up that specific dust species on average, as described by [Table 5.1](#).

In our model, we assume that the temperature of the hot and ejected gas phases are sufficient to destroy dust grains immediately, such that the cold gas or ISM phase of the model is the only one in which dust can survive. If dust in our model is moved out of the ISM due to a physical process, such as feedback, we assume that the dust is destroyed and returned to its metal components. In [Figure 5.1](#) we see a schematic outlining the main processes under consideration in the new dust model within the stellar disk and cold gas components, with the cold gas additionally split into its metal and dust components. When stars die in the disk, they enrich the cold gas with both metals (shown by the red lines) and dust (shown by the green lines). Dust is also grown inside molecular clouds from the accretion of metals onto pre-existing dust grains, and similarly dust grains can be destroyed by supernovae shocks and thus returned to its metal components. The dust growth and destruction processes are represented by the green lines showing exchange between the metal and dust components of the ISM. The blue lines represent the star formation process, where material from the ISM, including cold gas, metals and dust are

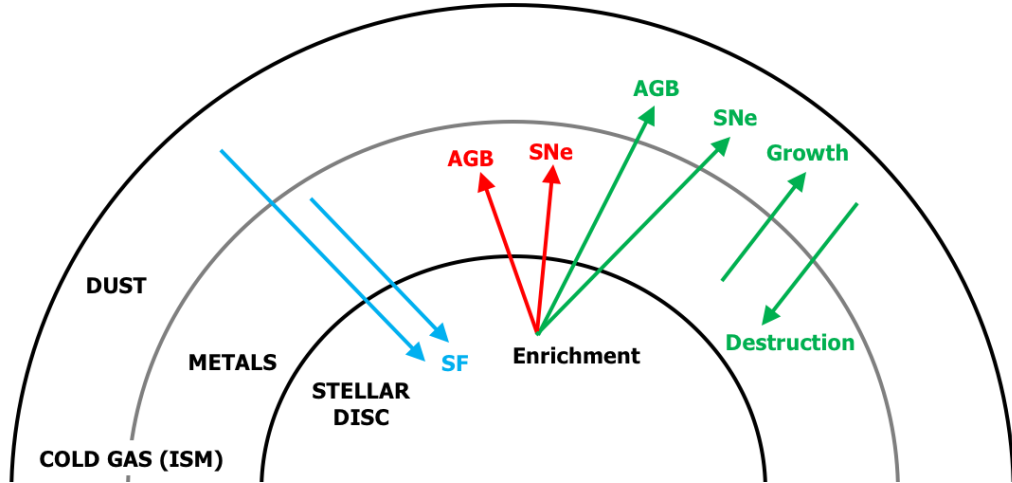


Figure 5.1: Schematic to show how the production of metals and dust is dealt with inside the model. This simple schematic shows the stellar disk component of a galaxy in our model, as well as the cold gas (ISM) component. The ISM is further split into the metal and dust components that we treat separately from one another. The red arrows show the enrichment of metals from the death of stars. The green lines show the enrichment of dust when stars die, as well as dust growth within molecular clouds (converting metals into dust), and grain destruction (converting dust into metals). Also shown is the star formation process, which removes both metals and dust (and cold gas) from the ISM into newly formed stars.

incorporated into newly formed stars. For simplicity, only processes directly relevant to the dust model are shown.

5.2 Other changes to the model

For the most part, the version of L-GALAXIES used for the rest of this thesis is the same one as in previous chapters. However, in order to model the dust more effectively, we required the implementation of the detailed chemical enrichment modelling of [Yates et al. \(2013\)](#), as this adds the delayed enrichment of 11 elements to the model. The switch from an instantaneous recycling approximation to delayed enrichment is very important, particularly when considering the growth of dust at very early times. The addition of the 11 elements to the model, which includes several refractory elements known to exist inside dust grains, such as silicon, carbon and iron, allows us to calculate the dust return from supernovae, which essentially converts some portion of the metals produced in supernovae into dust based on a condensation parameter derived from observations of local supernovae

Table 5.1: This table describes the different dust species considered in this work, and the average mass by element of each dust species. Where we have a dust species mass, such as from the low mass dust return tables, we then convert this to its individual elements based on the mass breakdown listed here.

Dust Species	Chemistry	Mass Breakdown
Forsterite	Mg_2SiO_4	Si (20%) O (45%) Mg (35%)
Fayalite	Fe_2SiO_4	Si (14%) O (31%) Fe (55%)
Enstatite	MgSiO_3	Si (28%) O (48%) Mg (24%)
Ferrosilite	$\text{Fe}_2\text{Si}_2\text{O}_6$	Si (21%) O (36%) Fe (42%)
Quartz	SiO_2	Si (31%) O (69%)
SiC	SiC	Si (70%) C (30%)
Iron	Fe	Fe (100%)
Carbon	C	C (100%)

remnants. This is described in more detail in Section 5.4.1 below.

5.3 Main Equation

The dust production rate of a galaxy can be simply given by the following equation:

$$\dot{M}_d(t) = \dot{Y}_d(t) + \dot{M}_{d,\text{grown}} - \dot{M}_{d,\text{dest}} + f(M_d) \quad (5.1)$$

where $\dot{M}_d(t)$ is the rate of dust production, $\dot{M}_{d,\text{grown}}$ is rate of dust grown in molecular clouds, $\dot{M}_{d,\text{dest}}$ is the rate of dust removed due to destruction. $f(M_d)$ describes other processes that are not included in the equation in order to keep it simple, but have an impact on the dust content of galaxies, such as star formation or feedback. We describe these processes in detail in Section 5.7 below. $\dot{Y}_d(t)$ is the stellar yield rate of dust production and is described by:

$$\dot{Y}_d(t) = \int_{m(t)}^{m_{up}} m_d(m, Z) \Phi(m) SFR(t - \tau(m)) dm \quad (5.2)$$

where $m_d(m, Z)$ is the mass of dust produced by a star of mass m and metallicity Z , $\tau(m)$ is the lifetime of a star with mass m , $\Phi(m)$ is the normalised IMF by number, and $SFR(t - \tau)$ is the star formation rate at the time when the star was born.

$SFR(t - \tau) \cdot \Phi(m)$ gives the birthrate of stars of mass m at time $(t - \tau)$. We then multiply this value by $m_d(m, Z)$, which is the mass of dust produced by a single star of

mass m and metallicity Z , giving us the total dust yield from stars of mass m at time t . We can then integrate over a suitable choice of mass limits to obtain the total yield rate, in the case above we use a lower limit of $m(t)$ to be the mass of star with a lifetime t , which would be the lowest mass of star that could have died by this time, and an upper limit of m_{up} , the highest mass of star considered in this work, which is $120M_{\odot}$.

5.4 Stellar Yields

In order to obtain the dust mass returned from stellar sources, such as AGB stars and supernovae, we must solve Equation 5.2 which gives us the total mass of dust returned from all stars that have died by a time, t . The mass of dust produced by a low mass star of given mass and metallicity is taken from the tables given in the literature (Ferrarotti and Gail, 2006). Unfortunately, there does not exist any table giving dust release from more massive stars, and we discuss what we do for the dust return from massive stars (via supernovae remnants) below in Section 5.4.1.

Solving the integral for each galaxy at each time step proved too time consuming and expensive, and in the end, unnecessary. Instead, much of the integral can be calculated before the main semi-analytic model is run, and the data stored in a set of look-up-tables that can be assessed during the main program. This is possible, in part, because the time structures of the star formation history arrays are the same for every galaxy at any given time step inside the code, allowing the determination of which stars can die (based on their initial mass) in each star formation history bin.

We can therefore rewrite Equation 5.2 as:

$$\dot{Y}_d(t) = SFR(t - \tau) \left[\int_{m(t)}^{m_{up}} m_d(m, Z) \Phi(m) dm \right] \quad (5.3)$$

where we now calculate the integral (assuming $1M_{\odot}$ stellar populations) before the main semi-analytic model is run and then multiply these pre-determined values by the stellar birthrate, which is now outside the integral. This requires an assumption that all stars in the range $m(t) \leq m \leq m_{up}$ are born at the same time, such that $\tau_{m(t)} = \tau_{m_{up}} = \tau$. The integral is then solved numerically for a range of metallicities, in every star formation history bin at every time step. The stellar lifetimes are taken from the mass and metallicity dependent tables from Portinari et al. (1998). Inside the model, the true metallicity value of a galaxy is used to interpolate between the pre-calculated integrals at each time step, and multiplied by the stellar birthrate. The total stellar dust yield is then given by $\dot{Y}_d(t) \cdot \Delta t$, where Δt is the width of the time step. Any dust that is produced is then removed from

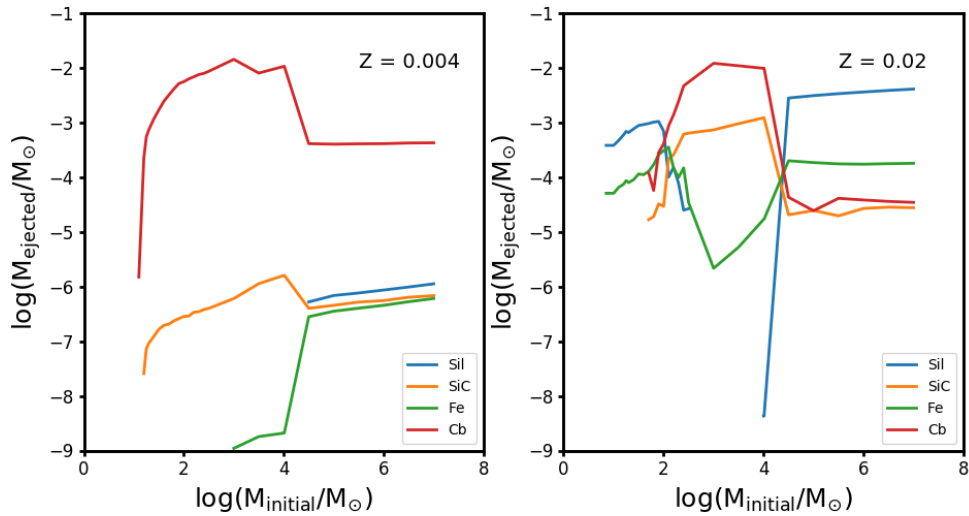


Figure 5.2: The mass of dust species (silicates, carbon, silicon carbide and iron) returned for a star based on the star’s initial mass. The left panel shows the relation for a metallicity of $Z = 0.004$, and the right panel for $Z = 0.02$ ($\sim Z_{\odot}$)

the metal component of the ISM and added to the dust component, in order to preserve the conservation of mass.

The [Ferrarotti and Gail \(2006\)](#) dust tables we use provide the mass of dust returned for a given low mass star as a function of key dust species, such as silicates or iron based dust grains, as shown in Figure 5.2. As discussed earlier, we store our dust grains as a structure of elements rather than as species, and so we convert between the two using the mass fraction of composite elements that build each dust species on average, as shown in Table 5.1.

During testing of the dust yields from low mass stars it became apparent that, very early in a galaxy’s life, we could end up with negative metal masses, and thus negative metallicities. This is the result of having produced more dust than we have metals available. On investigation it was discovered that the dust yield tables for low mass stars had a larger range of metallicities ($0.0002 < Z < 0.4$) than the partner tables that calculate metal return from low mass stars ($0.0004 < Z < 0.05$), in particular the dust yield tables went to higher metallicities. Thus for galaxies with very high metallicity, we could end up in a situation where we were producing more dust than we had metals. As dust is formed from metals, this should not be physically possible, and so we decided to limit the metallicity range of the dust yield tables to be the same for both dust and metal production. If a

galaxy has a metallicity greater than the highest metallicity available to us from the metal yield table, we return the maximum metal yield from the highest metallicity available to us, rather than attempt to extrapolate our metal and dust yields.

5.4.1 Supernovae

Unfortunately, there does not currently exist any dust yield tables for high mass stars that we can use in order to implement this production process in the same way as for AGB stars. Therefore, we follow the implementation defined in [Zhukovska et al. \(2008\)](#) where it is assumed that the amount of dust that is formed in supernovae remnants is proportional to the total mass return of the key element required to form that particular type of dust. The four types of dust modelled in [Zhukovska et al. \(2008\)](#) are silicates (main element Si), Silicon Carbides (main element Si), Carbon based dust (main element C) and Iron based dust (main element Fe). We then convert these dust species into their composite elements as described above and outlined in [Table 5.1](#). We also choose to implement SNIa dust production, despite conflicting reports in the literature (this was described in more detail in the previous chapter).

We use the following production rates for dust formed in core collapse supernovae:

$$R_{sil,dust} = \eta_{sil,SNII} R_{Si,SNII} \frac{A_{sil}}{A_{Si}} \quad (5.4)$$

$$R_{car,dust} = \eta_{car,SNII} R_{C,SNII} \frac{A_{car}}{A_C} \quad (5.5)$$

$$R_{sic,dust} = \eta_{sic,SNII} R_{Si,SNII} \frac{A_{sic}}{A_{Si}} \quad (5.6)$$

$$R_{iro,dust} = \eta_{iro,SNII} R_{Fe,SNII} \frac{A_{iro}}{A_{Fe}} \quad (5.7)$$

where A_x is the atomic weight of the given element or dust species; R_x is the mass return of a given element and η_x are the efficiency parameters for converting a specific species into dust and are based on observations of condensation in local supernovae remnants. These efficiency parameters are defined considering the effects of the reverse shock and are therefore smaller than they would be for initial dust condensation.

Similarly, for dust produced in the remnants of SNIa explosions:

$$R_{iro,dust} = \eta_{iro,SNIa} R_{Fe,SNIa} \frac{A_{iro}}{A_{Fe}} \quad (5.8)$$

The efficiencies and atomic weights can be found in [Table 5.2](#) and are taken from [Zhukovska et al. \(2008\)](#).

Table 5.2: The conversion efficiencies used for the production of dust grains in supernovae remnants based on the mass return of key metals.

	silicates	carbon	iron	SiC
η_{SNII}	0.001	0.15	0.001	0.0003
η_{SNIa}	0.0	0.0	0.005	0.0
key element	Si	C	Fe	Si
Atomic weight A	172.0	12.01	55.85	40.10

The only thing remaining for the calculation is now the mass return of specific elements from supernovae, which we get from our detailed chemical enrichment model, as described in Chapter 2. This enrichment model obtains the stellar yields of stars in the mass range $6M_{\odot} < M_{*} < 120M_{\odot}$, and for 5 different metallicities in the range 0.0004 to 0.05 from the yield tables by [Portinari et al. \(1998\)](#). Their work was based on the PADOVA stellar evolutionary tracks ([Girardi et al., 2000](#)).

5.5 Dust growth

The implementation of dust growth inside molecular clouds proved challenging. To model this properly, we would need to consider how accretion of metals onto dust grains varies for different grain surfaces and compositions and for different metals as these processes depend on the chemistry of the compounds involved. We instead go for a simpler model which requires far fewer assumptions. To start with we assume that any element in our model (except hydrogen and helium) can grow onto dust grains inside molecular clouds in a manner that is proportional to the current abundance of that particular metal, as described by the following equations.

The amount of dust grown inside molecular clouds is calculated following the prescription of [Zhukovska \(2014\)](#) (and the derivation in the previous chapter) and is given by:

$$\dot{M}_{d,grown} = \sum_j \left[\frac{1}{\tau_{\text{exch,eff}}} (f_j - f_{j,0}) (M_{j,metal} + M_{j,dust}) \right] \quad (5.9)$$

where $\dot{M}_{d,grown}$ is the total rate of dust grain growth when summed over all metals. $M_{j,metal}$ and $M_{j,dust}$ are the mass of element j currently in metals and in dust, respectively. f_j is the condensation fraction of element j onto dust grains, and is taken from our derivation in the previous chapter, using the analytic approximation from [Zhukovska et al. \(2008\)](#),

we define this to be:

$$f_j = \left[\left(f_{j,0} \left(1 + \frac{\tau_{\text{exch}}}{\tau_{\text{acc}}} \right) \right)^{-2} + 1 \right]^{-\frac{1}{2}} \quad (5.10)$$

where $f_{j,0}$ is the initial condensation fraction of element j in dust. We define this as the initial condensation at the start of each time step and it takes the form:

$$f_{j,0} = \frac{M_{j,dust}}{M_{j,metal} + M_{j,dust}} \quad (5.11)$$

The above equations consider two separate timescales, τ_{acc} and τ_{exch} . As we assume that dust can only accrete onto dust grains inside cold, dense environments, such as molecular clouds, we assume an effective exchange time, $\tau_{\text{exch,eff}}$, which describes the cycling of the cold gas (and thus metals) through molecular clouds and is taken from [Zhukovska \(2014\)](#), and is given by:

$$\tau_{\text{exch,eff}} = \tau_{\text{exch}} \frac{1 - f_{\text{mol}}}{f_{\text{mol}}} \quad (5.12)$$

where f_{mol} is the molecular gas fraction, and we explain how we obtain that from our model below. τ_{exch} is the time scale for exchange from molecular clouds to the ISM, and also the average lifetime of molecular clouds and is equal to 20Myr ([Murray and Rahman, 2010](#)).

A second timescale describes the accretion of material onto dust grains, and was also derived in the previous chapter:

$$t_{\text{acc}} = \left[\frac{m_g}{\nu \sigma_g v} \frac{V}{M_{mc}} \right] \frac{M}{M_{zd}} = t_{\text{acc},0} \cdot \frac{M}{M_{zd}} \quad (5.13)$$

The bracketed quantities represent the physical quantities of the grains. m_g is the mass of an individual dust grain, ν is the "stickability" factor of elements onto dust grain surfaces and takes a value between 0 and 1, σ_g is the grain cross section and v is the velocity of interactions of elements with the grain surface. V and M_{mc} are the volume and mass of an average molecular cloud respectively. M is the mass of metals inside all molecular clouds in our model available to grow onto dust grains and M_{zd} is the total amount of material available to form dust or currently inside dust.

If we assume typical values, for radius $a = 0.1 \mu\text{m}$ grains, we expect a typical grain density of 2 to 3 g/cm³. We can then calculate the grain mass, m_g , if we assume grains have spherical symmetry. The cross section, σ_g , can be approximated as πa^2 . We can find the thermal velocity easily if we assume a molecular cloud temperature of 50K, and an

average atom mass, for which we use carbon-12. This leaves us with the volume and mass of an average molecular cloud, which we take to be 10^5 pc^3 and $2 \times 10^5 M_\odot$ respectively. Combining these together gives us a timescale of $t_{acc,0} = 0.2 \text{ Myr}$.

We considered several other ways of dealing with dust growth inside molecular clouds. One way was to ignore the considerations of individual elements and instead do these calculations once, for just the total dust mass. That way, we can ignore the individual chemistry of specific elements in dust growth accretion, and it may even be more representative for element abundances as we make fewer assumptions about what happens in this phase. However we would lose information of the elemental make up of dust content in our galaxies by only tracking the total dust mass, and in testing, elements were able to convert from one species to another via the dust growth and destruction processes, thus metal abundances were no longer conserved.

Molecular gas fraction

The standard L-GALAXIES model does not differentiate between atomic and molecular hydrogen in the gas phase. We instead implement the model of [Blitz and Rosolowsky \(2006\)](#), first implemented into L-GALAXIES in [Martindale et al. \(2016\)](#), to split the cold gas components into atomic and molecular fractions. In this model, the ratio of HI to H₂ gas in a galaxy is determined by the mid-plane hydrostatic pressure in the galactic disk. We use the approximation to this model from [Obreschkow et al. \(2009\)](#):

$$R_{\text{mol}} = [K r_{\text{disk}}^{-4} M_{\text{gas}} (M_{\text{gas}} + \langle f_\sigma \rangle M_{\text{disk}}^{\text{stars}})]^\alpha \quad (5.14)$$

$$\frac{M_{\text{H2}}}{M_{\text{HI}}} = \frac{\int \Sigma_{\text{H2}}(r)}{\int \Sigma_{\text{HI}}(r)} \approx (3.44 R_{\text{mol}}^{-0.506} + 4.82 R_{\text{mol}}^{-1.054})^{-1} \quad (5.15)$$

where r_{disk} is the scale length of the gas disk, M_{gas} is the total cold gas mass, $M_{\text{disk}}^{\text{stars}}$ is the mass of the stellar disk and $K = G/(8\pi P_0)$. We adopt the same values for the constants as in [Obreschkow et al. \(2009\)](#): $P_0 = 2.34 \times 10^{-13} \text{ Pa}$, $\alpha = 0.8$, $\langle f_\sigma \rangle = 0.4$.

5.6 Dust destruction

There are a number of processes that can destroy dust in the ISM. Here we only consider the destruction of dust due to supernovae blast waves, following the prescription of [McKee \(1989\)](#):

$$\dot{M}_{d,\text{dest}} = \sum_j \left[\frac{M_{j,\text{dust}}}{\tau_{\text{dest}}} \right] \quad (5.16)$$

where $M_{d,\text{dest}}$ is the total amount of dust destroyed when summed over all elements, $M_{j,\text{dust}}$ is the mass of a particular element locked in in dust, and τ_{dest} is the timescale for destruction of dust:

$$\tau_{\text{dest}} = \frac{M_{\text{ISM}}}{M_{\text{cleared}} f_{\text{SN}} R_{\text{SN}}} \quad (5.17)$$

where M_{ISM} is the mass of the ISM which we take to be the cold gas mass in our galaxies. M_{cleared} is the amount of cold gas that is totally cleared of dust by an average supernovae. This can take a different value depending on the type of dust considered, in the range 600 - 1000 M_{\odot} . Rather than have a different value for each element locked up in dust, we choose to set this as a constant of 1000 M_{\odot} . f_{SN} accounts for the effects of correlated supernovae and supernovae out of the plane of the galaxy, and takes the value of 0.3. We calculate the rate of supernovae, R_{SN} , as the rate of supernovae type II and we derive it from the IMF.

We neglect dust destruction by SNIa shocks since $R_{\text{SNIa}} < R_{\text{SNII}}$ for the whole of galaxy evolution. We do not consider dust destruction due to UV radiation and cosmic rays.

5.7 Changes to existing functions in L-GALAXIES

There are other pre-existing functions that act on the cold gas phase in general, and they need to be modified to consider the dust that also now resides within the ISM.

Star formation

When parts of the ISM collapse to form stars, anything that resides within the ISM can also make its way inside stars, including both metals and dust. Due to the high temperatures involved, we make the assumption that any dust is almost certainly destroyed by the star formation process, and we add any dust to the stellar metal component (as opposed to the cold gas metal component). We remove dust from the ISM in proportion to the mass of stars that are formed.

$$\Delta M_d = - \left(\frac{M_{\text{formed}}}{M_{\text{cg}}} \right) \cdot M_d \quad (5.18)$$

Mergers

We follow the same methodology for merging galaxies as described in Chapter 2. In a minor merger, we assume the dust components of the merging galaxies survive and are placed into the disk component of the most massive galaxy. In a major merger, the disk component is transferred to the bulge of the descendant galaxy. It is assumed the dust can not survive at these higher temperatures and so it is destroyed into metals and added to the hot gas metal component of the new descendent galaxy.

Transfer functions

There are several other mechanisms, such as feedback, reheating or cooling, that call upon transfer functions in the code to move material between different phases in the galaxy, such as from the ISM to the CGM. We assume in our model that dust can only exist in the cold gas phase, and that anywhere else, the temperature is sufficient to destroy dust grains back to its metal components. Thus, any transfer of dust to gas phases outside the ISM, is put into the metal component instead.

5.8 A simple test model

In order to test the implementation of our code for the dust growth and destruction mechanisms, we can use a simple test model environment where we control everything, and then compare the answer from this simple model with the analytic solution of the equations that govern these mechanisms. Therefore we created a very simple model that starts with some basic initial conditions for the mass in cold gas and the mass in metals, and then apply the equations we are attempting to test at each time step. In all the three test scenarios below, there is no replenishment mechanism for the cold gas or for the metals. Figure 5.3 shows how the simple model works, at each time step, some cold gas is converted into stars, which can then produce some metals and dust. Over time, the cold gas depletes while the other components increase, as you'd expect for a simple model with no replenishment mechanisms for the cold gas. We now use this model to test three different scenarios: (1) dust growth only, (2) dust destruction only and (3) both dust growth and destruction.

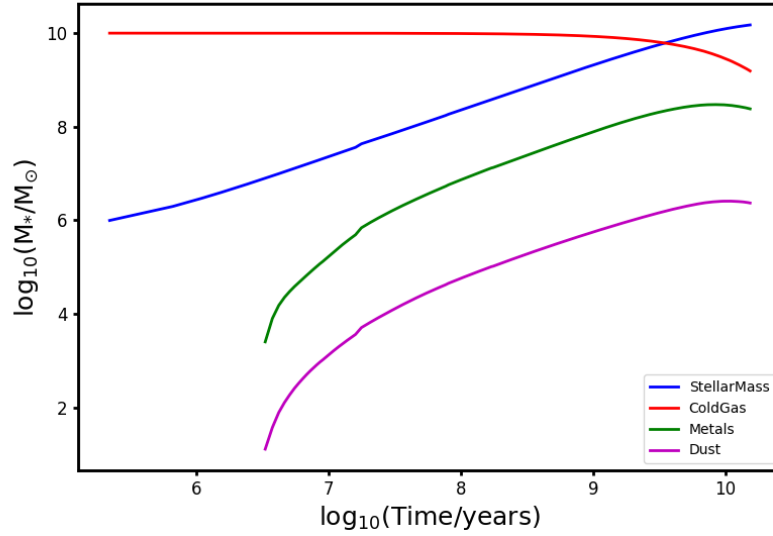


Figure 5.3: A plot showing how the cold gas, stellar mass, metal mass and dust mass evolve through time in our simple test model.

5.8.1 Dust growth

In the first test scenario, we will test the implementation of the dust growth equations. For this test, we seed our code with some initial cold gas mass, metal mass and dust mass. We need to start with some dust in order to grow more dust, as all other sources of dust production are disabled for this test. The evolution of the cold gas, metal mass and dust mass is shown in the left panel of Figure 5.4. In order to verify the code is working as intended, we must solve the dust growth equations analytically, and then compare with the model.

Analytic Solution

We start with the equation we are trying to solve, the dust growth equation:

$$\dot{M}_{d,\text{grown}} = \sum_j \left[\frac{1}{\tau_{\text{exch,eff}}} (f_j - f_{j,0}) (M_{j,\text{zd}}) \right] = \sum_j \left[\frac{1}{\tau_{\text{exch,eff}}} (f_j M_{j,\text{zd}} - M_{j,\text{dust}}) \right] \quad (5.19)$$

If we assume that for any specific element, j , that all interactions are the same, we can take care of the summation:

$$\dot{M}_{d,\text{grown}} = \left[\frac{1}{\tau_{\text{exch,eff}}} (f M_{\text{zd}} - M_{\text{dust}}) \right] \quad (5.20)$$

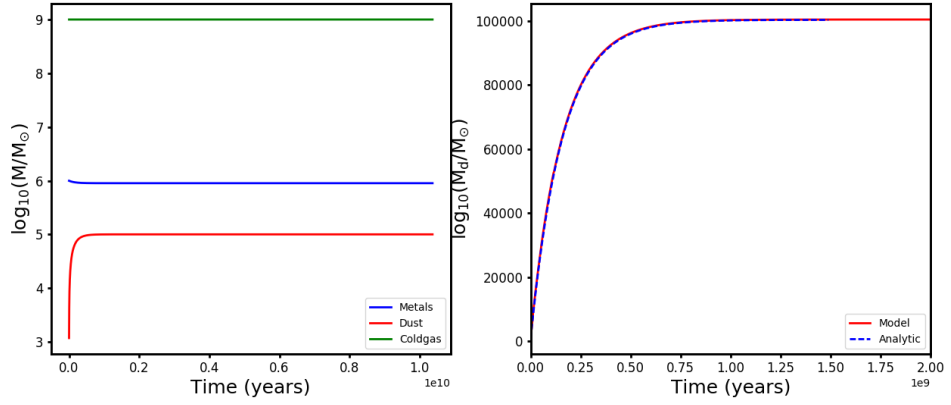


Figure 5.4: A simple model testing the implementation of the dust growth equations with the analytic solution.

In order to make the equation easier to solve, we can rename some of the variables. Let $B = \tau_{\text{exch,eff}}$, $A = f$ and $M_{\text{dust}} = D$. In the case of our simple model, with no replenishment mechanisms for cold gas or metals, and with known initial conditions, we are able to rewrite $M_{\text{zd}}(t) = M_{\text{metals}}(t) + M_{\text{dust}}(t) = M_{\text{metals}}(0) - M_{\text{dust}}(t) + M_{\text{dust}}(t) = M_{\text{metals}}(0) = C$. In order to make the equation easier to solve, we also treat f as a constant. If we then substitute this into the above equation, we get:

$$\dot{D} = \left[\frac{1}{B}(AC - D) \right] \quad (5.21)$$

Grouping similar terms:

$$\dot{D} \left(\frac{1}{AC - D} \right) = \frac{1}{B} \quad (5.22)$$

$$\int_{D(t=0)}^{D(t)} \left(\frac{1}{AC - D} \right) dD = \int_{t=0}^t \frac{1}{B} dt \quad (5.23)$$

which can be solved using integration by substitution:

$$\left[-\ln[AC - D] \right]_{D(t=0)}^{D(t)} = \left[\frac{t}{B} \right]_{t=0}^t \quad (5.24)$$

$$\frac{t}{B} = \left[-\ln[AC - D] \right] - \left[-\ln[AC - D_0] \right] \quad (5.25)$$

$$t = B \ln \left[\frac{AC - D_0}{AC - D} \right] \quad (5.26)$$

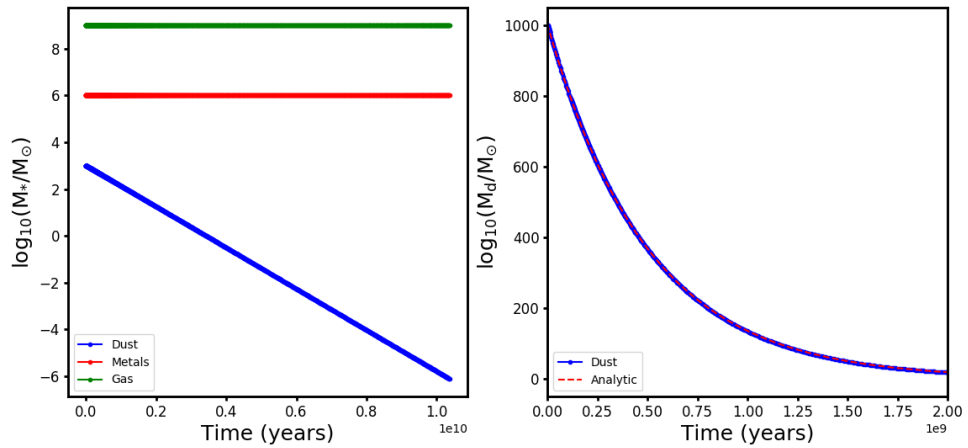


Figure 5.5: A simple model testing the implementation of the dust destruction equations with the analytic solution.

Physically, D , or M_{dust} can take any value $M_{d,0} \leq M_d \leq fM_{m,0}$, and given the above analytic solution, we are now able to calculate a time, t , for a given M_{dust} value. Comparing this with the output of the simple model should give the same distribution of answers if the code is implemented correctly. This can be seen in the right hand panel of Figure 5.4, where you can see they are the same.

5.9 Dust destruction

The second implementation test we considered was the equations for the dust destruction process. In this case, our simple model was seeded with an initial mass of cold gas, metals and dust but this time there were no dust production mechanisms at all. The left panel of Figure 5.5 shows the evolution of the cold gas, metals and dust mass and we can see that it evolves as expected, with the dust mass getting depleted over time due to no replenishment mechanisms. Once again, we can solve the equations analytically in order to compare with this simple model.

Analytic Solution

We start with the initial equation for the dust destruction mechanism:

$$\dot{M}_d(t) = -\frac{1}{\tau_{des}} M_d \quad (5.27)$$

For simplicity let the destruction timescale be a constant such that, $\frac{1}{\tau_{des}} = A$, thus making the equation trivial to solve:

$$\frac{dM_d}{dt} = A.M_d \quad (5.28)$$

$$\int_{M_d(0)}^{M_d(t)} \frac{1}{M_d} = \int_{t_0}^t A dt \quad (5.29)$$

$$[\ln(M_d)]_{M_d(0)}^{M_d(t)} = A.t \quad (5.30)$$

$$- \ln\left(\frac{M_{d,0}}{M_d(t)}\right) = A.t \quad (5.31)$$

$$t = -\frac{1}{\tau_{des}} \ln\left(\frac{M_{d,0}}{M_d(t)}\right) \quad (5.32)$$

We can solve this for a range of values $0 \leq M_d \leq M_{d,0}$, and then compare with the output from the simple model, as shown in the right hand panel of Figure 5.5 and as you can see, the results are the same.

5.9.1 Additional test: Dust growth and destruction in a steady state

The third and final test we tried was the implementation of both the dust growth and destruction processes together. Combining the equations for dust growth and destruction, we get a function that looks like this:

$$\dot{M}_{dust}(t) = \left[\frac{1}{\tau_{exch,eff}} (fM_{zd}(t) - M_{dust}(t)) \right] - \frac{1}{\tau_{des}} M_{dust}(t) \quad (5.33)$$

This is less trivial to solve than the previous two tests. Instead, we can consider a steady state, where $\dot{M}_d(t) = 0$, this allows us to solve this equation to find a value of M_{dust} where the dust growth and destruction processes will stagnate. With a little rearranging we end up with:

$$\frac{1}{\tau_{exch,eff}} (fM_{metals}(0) - M_{dust}(t)) = \frac{1}{\tau_{des}} M_{dust}(t) \quad (5.34)$$

$$M_{dust}(t) = \frac{fM_{metals}(0)}{\tau_{exch,eff}} \cdot \frac{1}{\frac{1}{\tau_{exch,eff}} + \frac{1}{\tau_{acc}}} \quad (5.35)$$

Substituting the values for these constants and initial conditions from our simple model, we find a value where the growth and destruction processes stagnate to be $M_d \sim 75758M_{\odot}$.

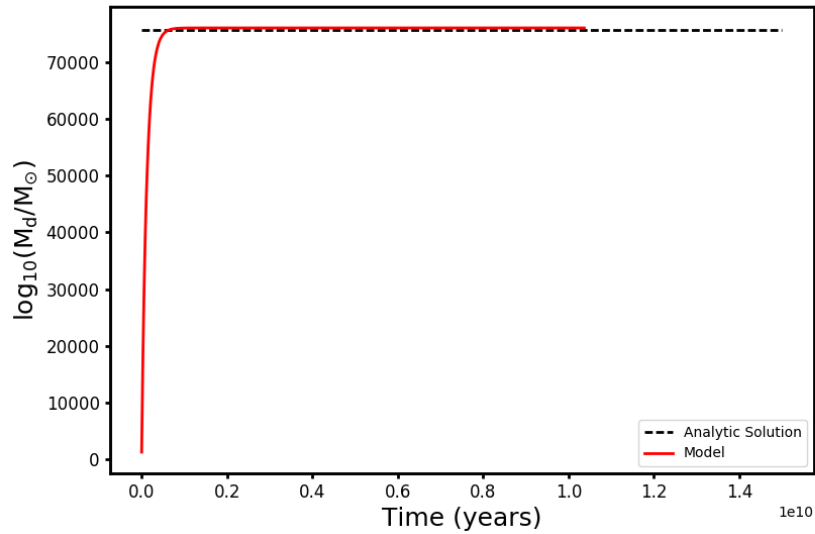


Figure 5.6: A simple model testing the implementation of both the dust growth and destruction equations with the analytic solution.

If we compare this to how our simple model evolves, as shown in Figure 5.6, you can see that the model tends towards the value calculated as predicted.

5.10 Testing the model

For the remainder of this chapter we will discuss the testing of the model once fully implemented into the L-GALAXIES SAM, including some of the variations of the model we ran in order to finalise the model and its parameters. Rather than do this on the full Millennium and Millennium-II simulations, we run on only one tree file of Millennium, representing 1/512 of the full Millennium box, but chosen to be representative of the full simulation.

If we put all the components described above together, we now have a physically motivated dust model built into L-GALAXIES which includes production from AGB stars, supernova remnants and grain growth inside molecular clouds, and also a model of dust destruction due to supernovae shocks. One of the first plots we can look at is the stellar mass to dust mass relation at $z=0$, shown in Figure 5.7. This was a function we had been watching during the development of the model, and something we had wanted to match, in part due to the large number of observational constraints available for this at $z=0$ and beyond. This plot shows the L-GALAXIES model described above, with no additional or

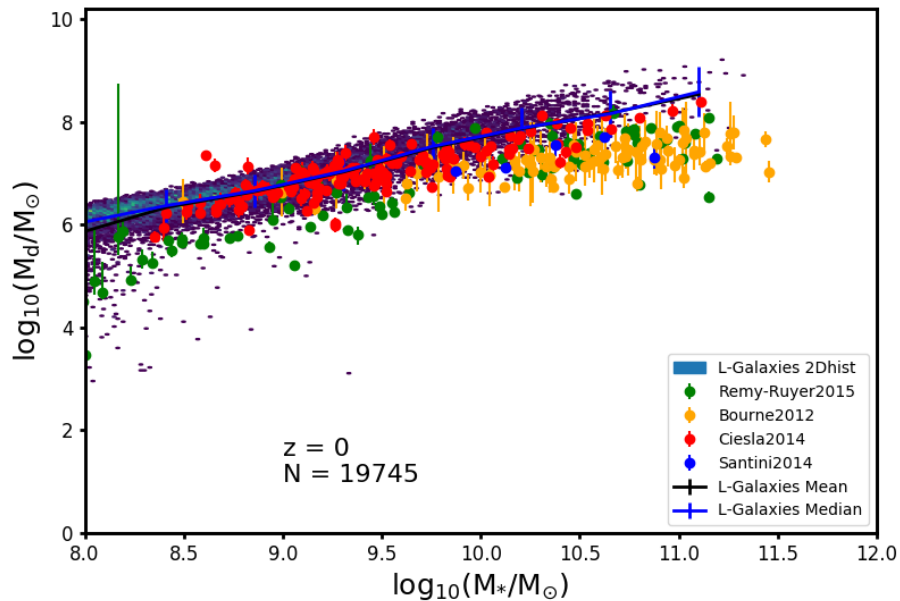


Figure 5.7: The stellar-dust mass relation at $z=0$. The black line shows the median result of our model, with the 2D histogram underneath representing individual galaxies. The model was only run on 1/512 of the total Millennium simulation, though on a tree thought to be representative. The observations are shown by coloured points.

fine tuning of any parameters. A selection criteria is applied to select star forming galaxies only, in order to match the same selection bias of observations. For the median model value to match as well as it does is impressive, though we are obviously over estimating the amount of dust in the most massive galaxies at this redshift when compared with the observations. With that said however, there is a discrepancy in the shape of the relation between the four different observational datasets, and we investigate this further in the next subsection.

5.10.1 Variation in observations

There is a large discrepancy in the observations available at $z=0$ for the stellar-dust mass relation, particularly in the shape of the relation at the high mass end. This is highlighted in Figure 5.8 which shows our model compared with each individual dataset in a separate panel. The observations from Rémy-Ruyer et al. (2015), Bourne et al. (2012) and Ciesla et al. (2014) show individual galaxies, where as Santini et al. (2014) shows binned data. All these observed dust and stellar mass quantities were derived from model fitting to the spectral energy distributions (SEDs) of the observed galaxies.

Our model shows the best fit to the [Ciesla et al. \(2014\)](#) observations, matching both the shape and normalisation well. The [Rémy-Ruyer et al. \(2015\)](#) observations show a much larger scatter and larger errors than the other observational datasets, but when compared with our model shows a fairly good agreement to the shape, though the observations have a slightly lower normalisation across all stellar masses. [Bourne et al. \(2012\)](#) shows a much shallower relation than the model does, with the largest discrepancy at the high mass end where the difference between the observations and the model is quite large. As for the [Santini et al. \(2014\)](#) data, if we ignore the last data point, the model matches the shape of the function, but doesn't quite match the normalisation, though it is within the scatter shown by the underlying histogram.

The observations themselves contradict one another, particularly at the high mass end, and this just highlights how difficult it is to obtain dust masses from observational data. The SED fitting process requires a number of assumptions. The fact that the model matches the shape of almost all the observations, and does a fairly good job at matching the normalisation, particularly for low to intermediate mass galaxies, is encouraging. Though we do appear to over predict the dust content of the most massive galaxies.

5.10.2 Convergence of MR and MR II

It is standard practice in [Henriques et al. \(2015\)](#) to make full use of both the Millennium and Millennium-II simulations at low redshifts, so that we benefit from both the larger volume of Millennium, but also benefit from the higher mass resolution of Millennium-II. This however, requires that the simulations converge at some point in the plane you are considering.

We plot the stellar-dust mass relation for a range of redshifts $z=0-9$ in [Figure 5.9](#) using both Millennium and Millennium-II separately, and we can see that the simulations converge in this space for $z=0-4$ at $\sim 10^9 M_\odot$, but fail to do so at higher redshifts. This test was only conducted on one (representative) tree file, so we may have more success at $z=5$ and $z=6$ when running the full simulations.

We plot the stellar-dust mass relation for a range of redshifts $z=0-9$ in [Figure 5.9](#) using both Millennium and Millennium-II separately, and we can see that the simulations converge in this space at around $10^9 M_\odot$ for $z=0-6$. At higher redshifts, Millennium-II doesn't have galaxies with sufficient mass to converge with Millennium. This test was only conducted on one (representative) tree file, so more tree files may show convergence at the higher redshifts too.

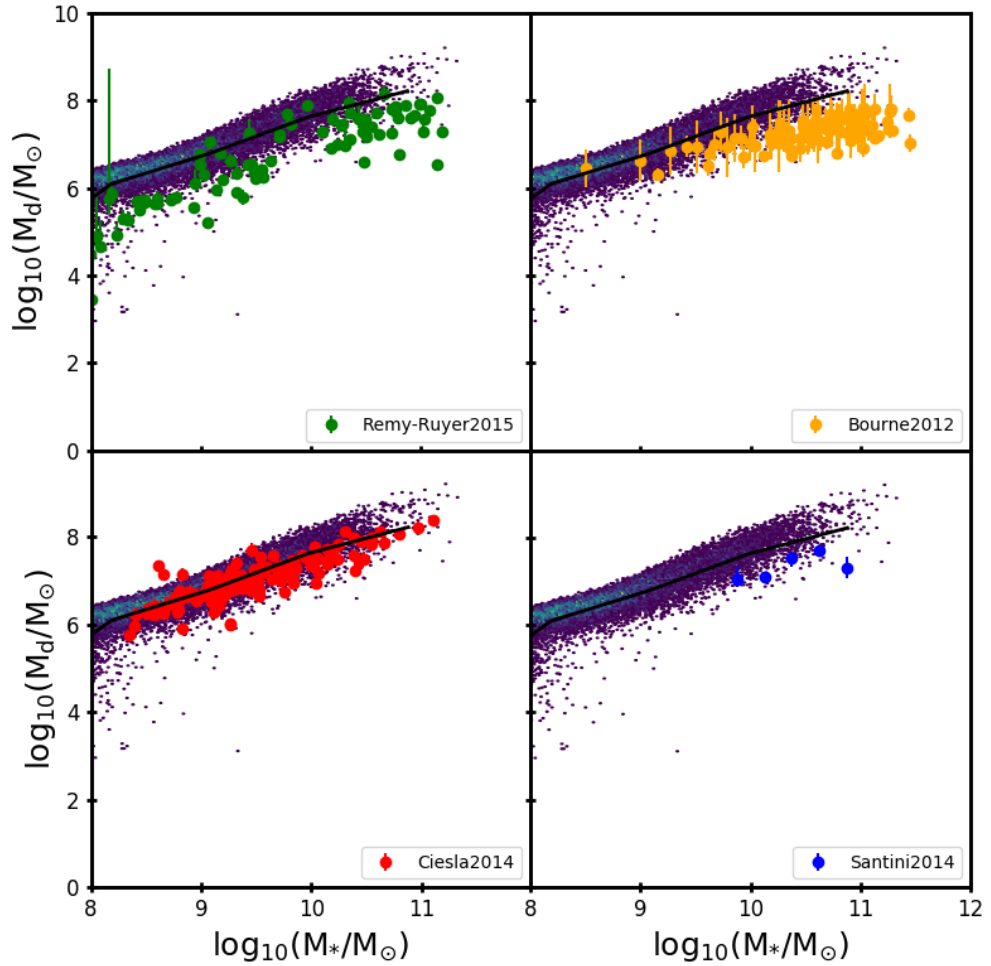


Figure 5.8: The stellar-dust mass relation at $z=0$. The black line shows the median result of our model, with the 2D histogram underneath representing individual galaxies in purple. The model was only run on 1/512 of the Millennium simulation, though on trees thought to be representative. Each panel represents a different set of observations, [Rémy-Ruyer et al. \(2015\)](#) in the top left, [Bourne et al. \(2012\)](#) top right, [Ciesla et al. \(2014\)](#) bottom left and [Santini et al. \(2014\)](#) bottom right.

Figure 5.9 shows that we can combine our analysis of the two simulations for $z=0-6$ and so we will do this in the next chapter of this thesis when we run the model on the full Millennium simulations.

5.11 Different production mechanisms

Our dust model is comprised of several different production mechanisms, and it could be interesting to know how important each one is to the dust production in galaxies. The contribution of each type, such as whether AGB stars dominate in the local universe but supernovae are much more important at earlier times, or if we need efficient grain growth in the early universe to explain high redshift observations has long been debated in the literature, and we provide a summary of this in the previous chapter. Having modelled these processes over a cosmological time we can provide some insight to what works best in our model by switching off specific components.

In this section, we run our model for a number of different scenarios: (1) dust production by AGB stars only; (2) dust production by supernovae type-II only; (3) dust production by supernovae type-Ia only; (4) dust production by grain growth in molecular clouds only; (5) all the dust production mechanisms in scenarios 1,2,3,4 but with no dust destruction mechanisms and (6), the intended model, with all production and destruction mechanisms. In the case of scenario 4, you will never get any dust growth in molecular clouds if you have no initial seeding of dust from stellar sources, so we seed these galaxies with an initial dust mass. The seeded dust mass is chosen to be very small, but dust growth is expected to begin in these galaxies before it usually would and thus we expect slightly higher dust masses for this test. All the model variants are shown for redshift $z=0$ in the stellar-dust mass relation in Figure 5.10 and then compared against observational constraints.

Its clear from Figure 5.10 that none of the stellar sources of dust (AGB, SNII, SNIa) are capable of matching this relation at $z=0$ on their own. Its important to remember that L-GALAXIES is a self-consistent galaxy formation model across cosmic time, so what happens in the past affects the future. Thus, AGB stars may not be the sole contributor to the dust mass across all times, but they may still be very important at low-redshifts. We will discuss the evolution of the dust rate for these production mechanisms in the next chapter. For now though it is clear that, not only is dust growth in molecular clouds necessary, it totally dominates by $z=0$, almost identically matching the plot representing the ideal case with everything switched on. What is perhaps more surprising is how little

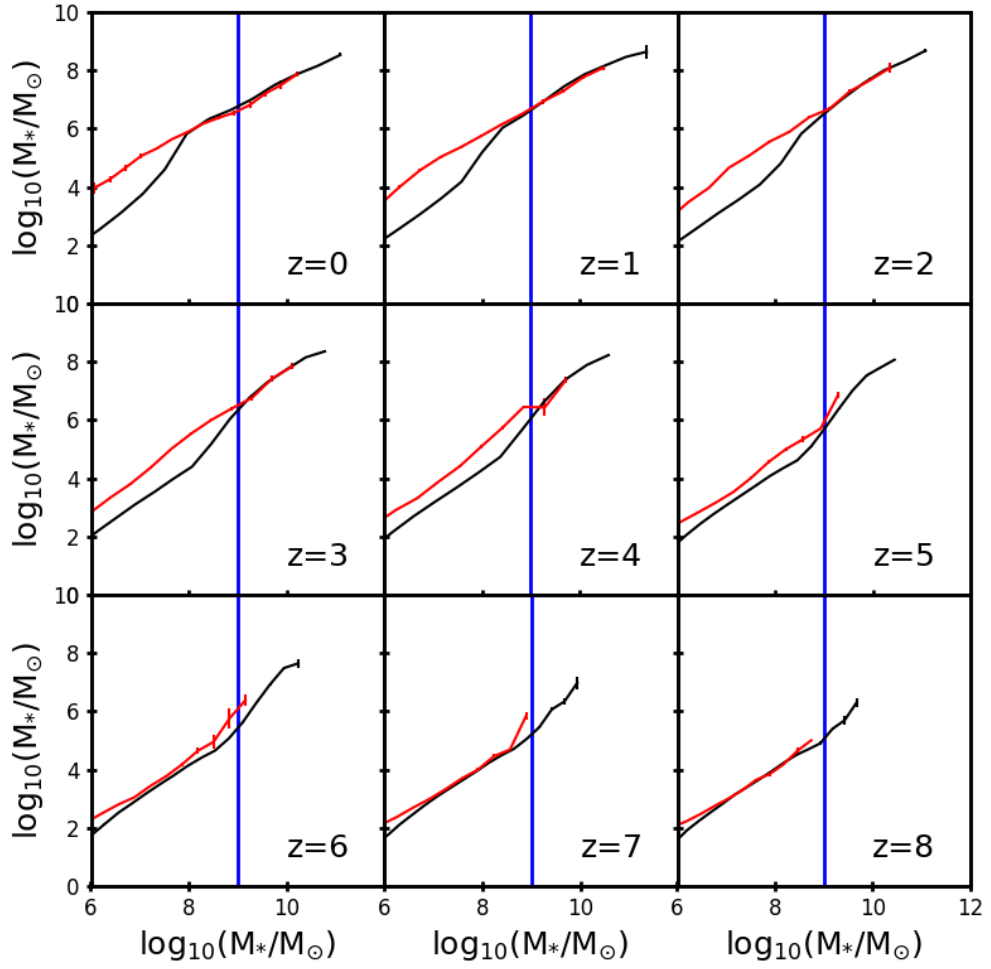


Figure 5.9: The stellar-dust mass relation for redshifts $z=0-8$. The black line shows the results from the Millennium simulation, whereas the red line shows the results from the Millennium-II simulation. A line is drawn at $10^9 M_\odot$ (roughly the convergence point) to guide the eye.

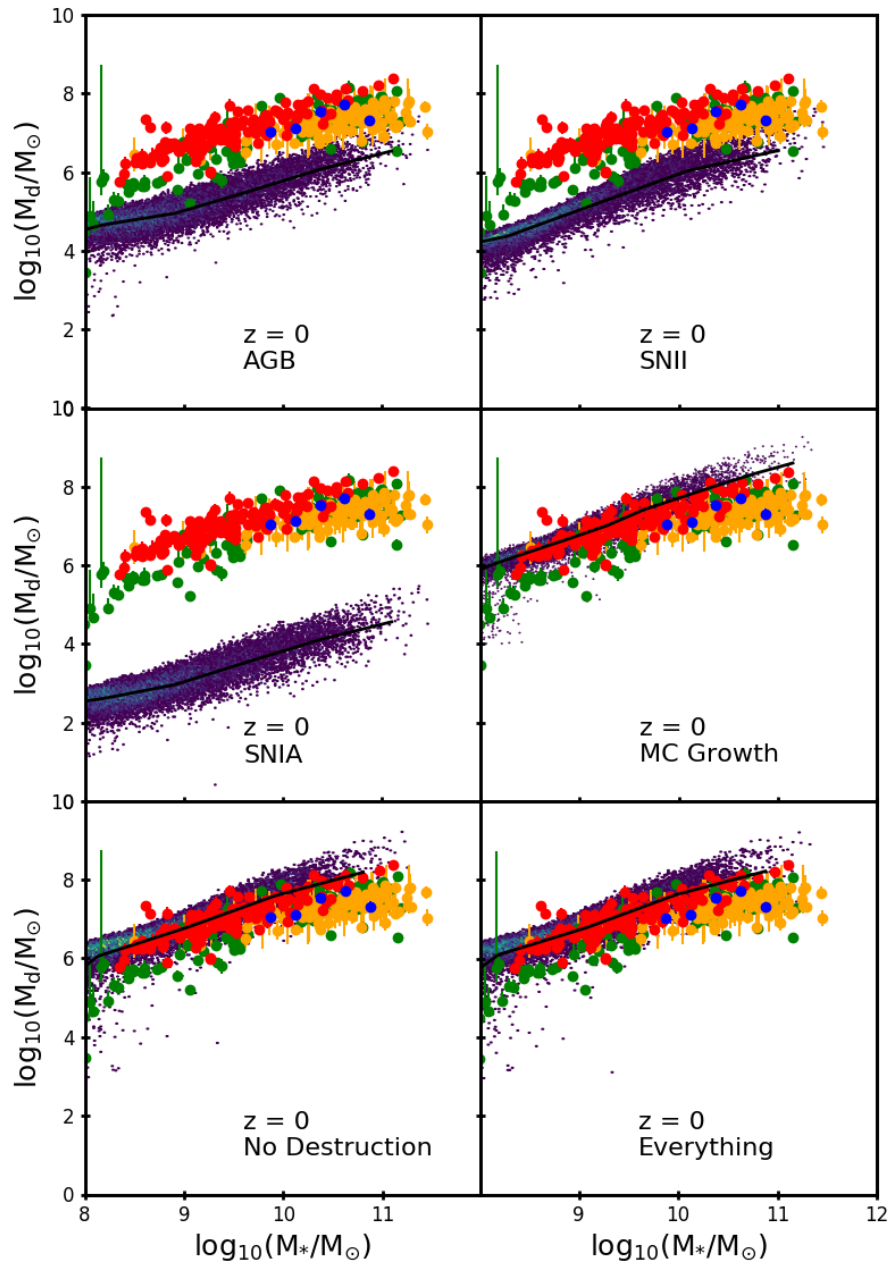


Figure 5.10: The stellar-dust mass relation at $z=0$ when running different variations of the dust model. These include: AGB dust production only (top left); supernovae type II production only (top right); supernovae type Ia production only (centre left); grain growth production only (centre right); no dust destruction (bottom left); and the idealised model with all production and destruction mechanisms (bottom right). The purple points show individual galaxies in our model and the black line shows the median. Red, green, orange and blue points show the observational constraints.

the model changes when we switch off dust destruction. This led to an investigation at higher redshifts to see if this was always the case.

Figure 5.11 shows the stellar-dust relation, using the model variations outlined above but for redshifts $z=0-7$. While the dust growth, no destruction and ideal models are all practically identical at $z=0$, this is not always the case. Surprisingly, the model with no destruction only shows a noticeable difference to the fiducial model at very high redshifts and in the most massive galaxies. Stellar sources of dust on their own struggle to reproduce the observations at all redshifts. For the model with only dust growth, it does not match the observations at $z=5-7$, but starts to reach the required normalisation in high mass galaxies between $z=3$ and $z=4$. By $z=2$, it can achieve the required dust masses in all but the lowest mass galaxies, and finally matches the full shape and normalisation for $z=0-1$. Our model highlights the need for a fast efficient dust growth mechanism that occurs very early on in galaxy formation to explain the observed dust masses in high redshift galaxies, though those galaxies must first be seeded with a source of dust from stellar sources. Without a combined stellar and grain growth production model, we fail to achieve the observed results at $z=5-7$.

There are times in Figure 5.11 when it seems that the dust growth only model lies above the no destruction model. This is due to the initial seeding of the galaxies with dust in the growth only model.

5.12 Varying model parameters

In this section we vary some of the model parameters introduced in the dust model to see how this impacts the results. Two of the quantities we will experiment with are the dust accretion timescale (described by Equation 5.13) and the total amount of dust destroyed. Both of these parameters are derived using physical quantities, though its been common practice to set these as free parameters in other work, particularly the dust accretion timescale (e.g. Dwek (1998), Zhukovska et al. (2008), Popping et al. (2016)).

5.12.1 Varying the rate of grain growth in molecular clouds

In Section 5.5, we calculated a value for the dust accretion timescale from physical quantities, and arrived at a value of 0.2Myr. However, for the work in this section, we set this as a free parameter to see how this impacts the results.

Figure 5.12 shows the stellar-dust mass relation at redshift $z=0$ for three different accretion timescales, 0.2Myr, 2.0Myr and 20Myr. As expected, longer timescales result in

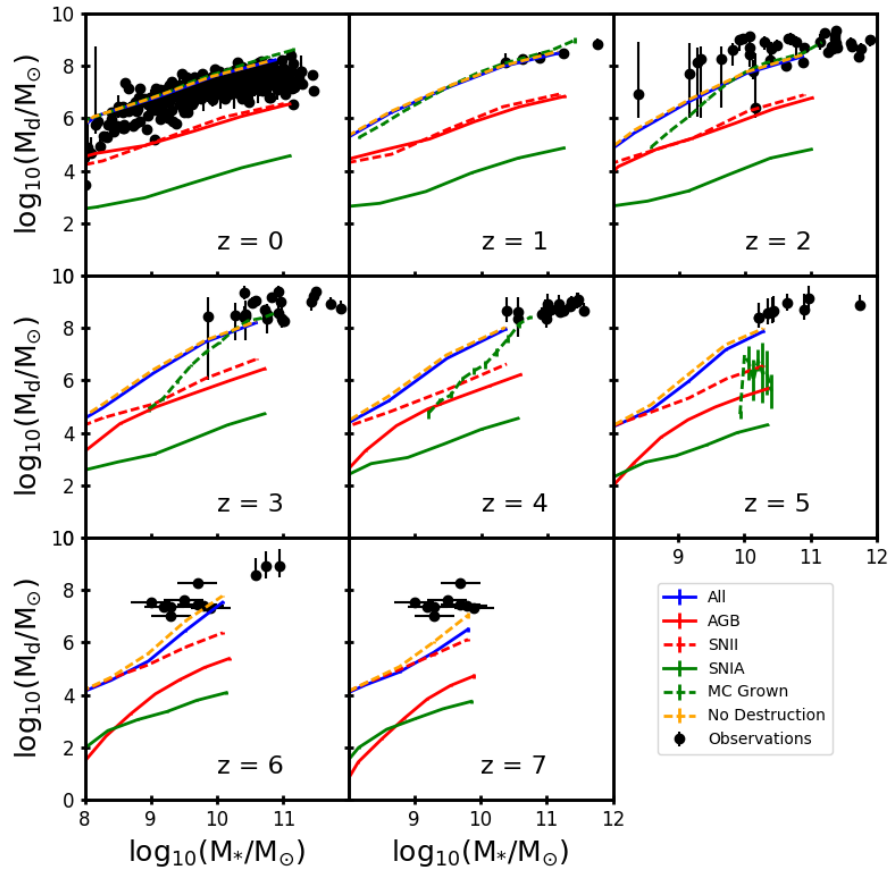


Figure 5.11: The stellar-dust mass relation at $z=0-7$ when running different variations of the dust model. These include: AGB only; SNII only; SNIa only; grain growth in molecular clouds only; no destruction; and a fiducial model with all production mechanisms switched on with destruction. The black points show observations from a number of different sources as described in the text.

less dust growth, though the difference between 0.2Myr and 2Myr is minor by $z=0$. We see slightly less dust mass for the same stellar mass for the 2Myr timescale, and a larger scatter in the model galaxies, particularly at the low mass end. This suggests that the time scale here is not the defining characteristic, and that it's a lack of metal material preventing further growth for the 0.2Myr timescale, or that the growth rate has reached a steady state with the dust destruction. For timescales of 20Myr, we see that we no longer produce enough dust to match the observational constraints by approximately one order of magnitude. This highlights how important the production of dust via a grain growth mechanism is to the total galactic dust mass, but also how sensitive it is to the choice of accretion timescale.

5.12.2 Varying the mass of dust destroyed

In this section we choose to vary the destruction rate by changing the mass of dust destroyed by a factor of 0.1, 1.0 or 10.0 and the results for this are shown in Figure 5.13. The fact that there is negligible difference between the models for 'normal' dust destruction and when it is reduced by a factor of 10, suggests that its effect is minor at $z=0$, and corresponds with what we noticed above when varying the accretion timescale between 0.2Myr and 2.0Myr, that dust growth is limited more by the amount of available metals for accretion at redshift $z=0$ than anything else. By reducing the dust destruction by a factor of 10 we see that our galaxies only gain a small amount of dust, suggesting that grain growth is already close to peak efficiency at a destruction rate of 1.0. We do see a reduction when we increase the amount of dust destroyed by a factor of 10, though it mainly manifests itself as a change in the shape of the relation, particularly for high mass galaxies. We also see a population of galaxies below the main relation when using this increased destruction factor that suggests a number of galaxies have had their dust masses quenched significantly. This occurs across the full range of stellar masses and is not limited to just high mass galaxies. The fact that the mass in dust destroyed does not seem to be important is an effect of showing this graph at $z=0$. The mass in dust destroyed is proportional to the supernovae rate and thus the star formation rate, which is decreasing at $z=0$. We explore the effects of dust destruction at higher redshifts, where it has more of an impact, in the next subsection.

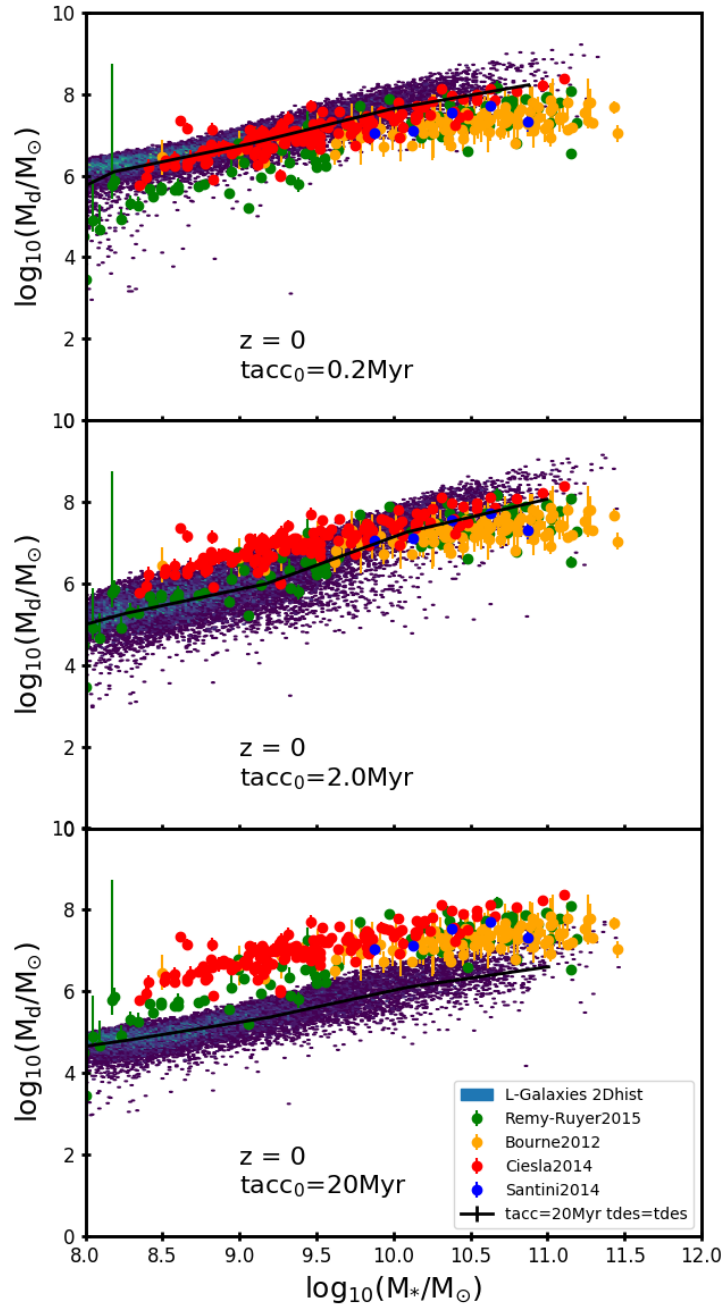


Figure 5.12: Stellar-dust mass relation at $z=0$ with the dust accretion timescale set as a free parameter. It takes a value of 0.2Myr in the top panel, 2.0Myr in the central panel and 20Myr in the bottom panel.

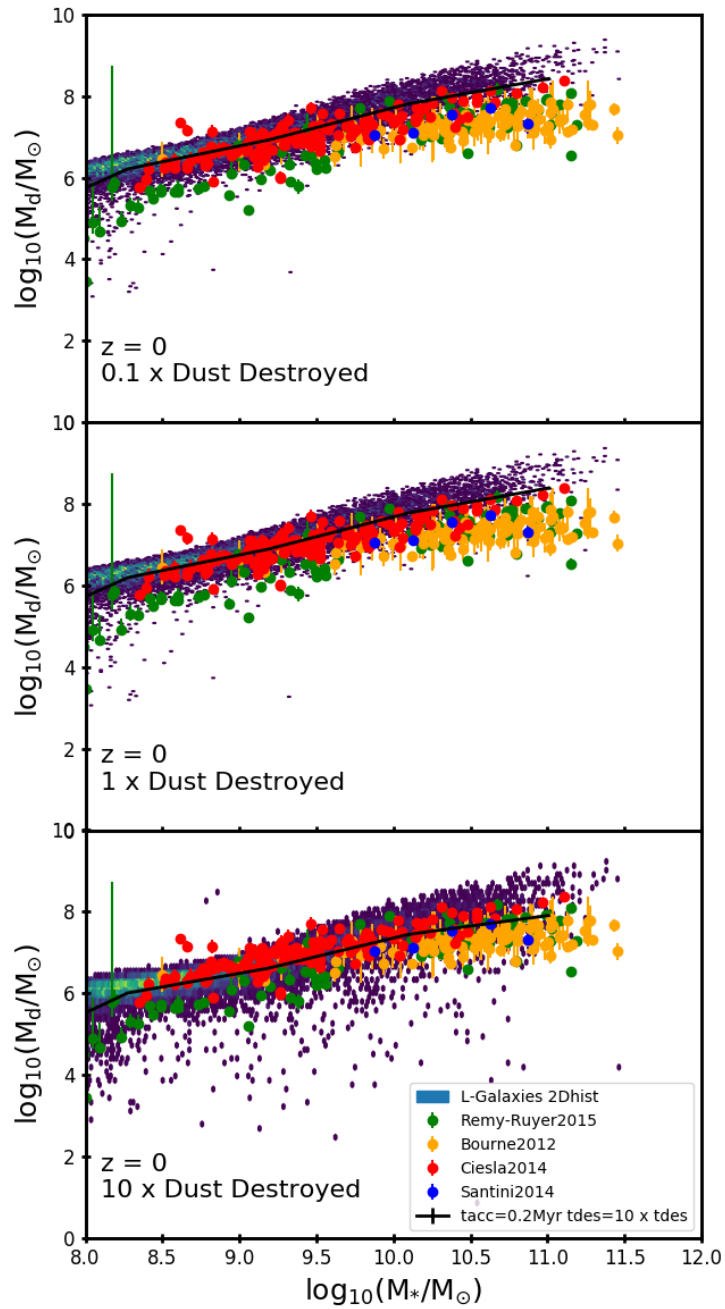


Figure 5.13: Stellar-dust mass relation at $z=0$ while varying the amount of dust destroyed in the model. The top panel shows a model where we have reduced dust destruction by a factor of 10, the central panel shows the ‘normal’ destruction, and the bottom panel shows increased destruction by a factor of 10.

5.12.3 Varying dust growth and destruction at higher redshift

We are attempting to produce a dust model that reproduces observed dust properties at all redshifts, not just $z=0$, so we need to see how varying the growth and destruction rates effects results at higher redshifts. Figure 5.14 shows the stellar-dust relation at redshifts $z=0-7$, for the ‘normal’ parameter model, as well as the varied models outlined in the two sections above for varied growth and destruction rates.

Varying the growth accretion timescale from 0.2Myr to 2.0Myr or 20Myr shows suppressed dust growth in both models until relatively low redshift. The two only start to diverge in high mass galaxies at $z=3$, and in all galaxies by $z=0$. A timescale of 20Myr fails to reproduce observed dust masses at all redshifts, but a timescale of 2.0Myr begins to match observations at the high mass end around $z=1$, and at all masses at $z=0$.

Models run with less destruction are the only models capable of achieving the normalisation required to match the dust properties of galaxies at $z=7$, with the full model catching up by $z=4$. Increasing the amount of dust destroyed significantly suppresses the growth of dust in galaxies, failing to match observed dust masses by orders of magnitude until $z=0$.

These results highlight the need for an efficient dust growth mechanism at high-redshift, as only models with a growth timescale of 0.2Myr able to match the observed normalisations. Variations in these timescales are possible if you’re only interested in matching the results at $z=0$, such as increased destruction, or a longer growth timescale.

5.13 Conclusion

In this chapter we have introduced a physically motivated dust model into the L-GALAXIES semi-analytical model and performed some initial testing on only a few tree files of the Millennium simulation (which represents 1/512 the total volume). Our conclusions are as follows:

- (i) L-GALAXIES now includes a physically motivated dust model that tracks the production of dust from supernovae remnants, AGB winds and grain growth inside molecular clouds. The model also includes a model for dust destruction by supernovae shocks.
- (ii) The dust model is fully integrated into L-GALAXIES such that the evolution of dust is included in all the recipes relevant to the formation and evolution of galaxies, including: metal enrichment; star formation; radiative feedback; cooling and reheating; and both major and minor mergers.

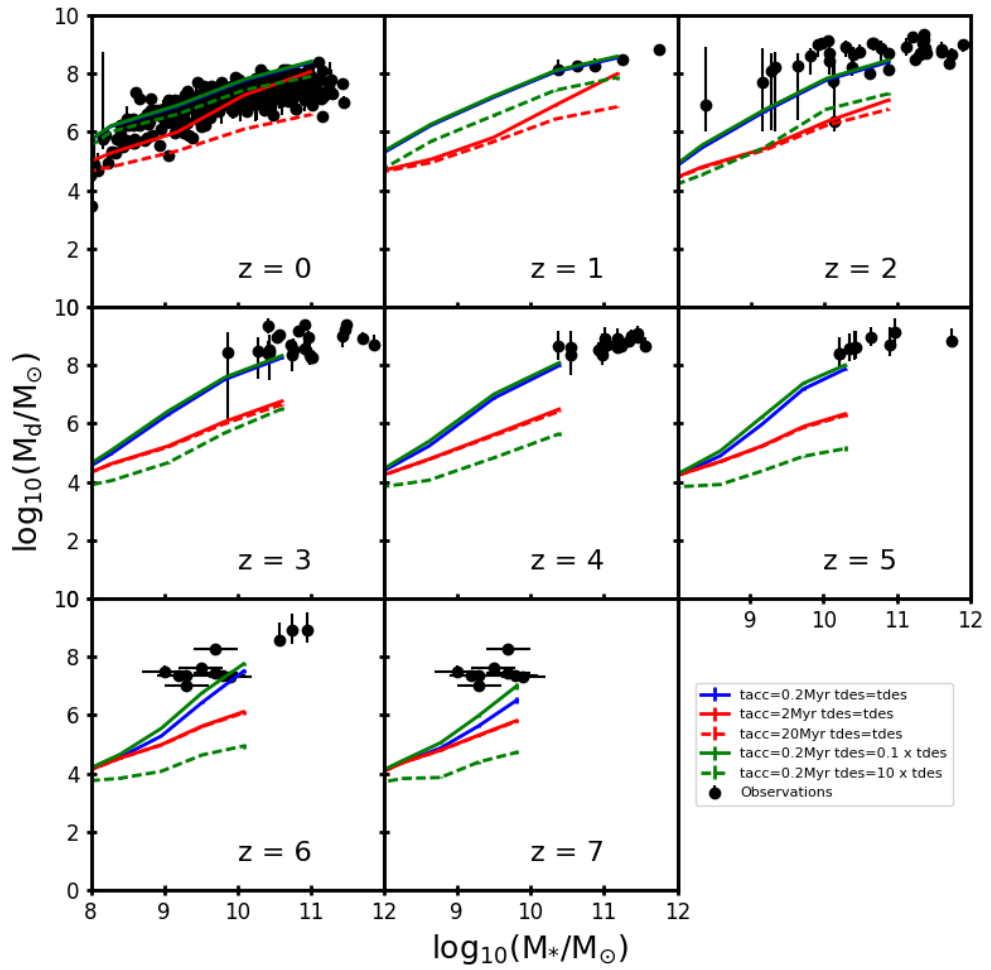


Figure 5.14: Variations of the stellar-dust relation at different redshifts ($z=0-7$) for variations of the dust growth and dust destruction efficiencies in the model.

- (iii) A simple modified model was run to test the implementation of the grain growth and destruction processes which were then compared with the analytic solution; this confirmed they were working as intended (Figures 5.4, 5.5 and 5.6).
- (iv) We find a good fit to the shape and normalisation of the stellar-dust mass relation at $z=0$, particularly at the low to intermediate masses, though we over predict the dust mass in the most massive galaxies (Figure 5.7). However we note a large discrepancy in the observations, particularly at the high mass end (Figure 5.8), though we find a good fit to the Ciesla et al. (2014) observations at all masses.
- (v) We found that running variations of the model to only include stellar sources of dust could not reproduce the stellar-dust mass relation, even at early times ($z=7$); the predicted dust masses from supernovae are almost two orders of magnitude lower than required to match the observations. This suggests the need for efficient dust production in the early universe, which can only be explained by grain growth in molecular clouds. When we include grain growth in our model, we match the observations at all redshifts where we have observations ($z=0-7$) (Figure 5.11).
- (vi) When experimenting with the dust accretion timescale as a free parameter, we found that increasing it by an order of magnitude provided a slightly better fit to observations at $z=0$, at the expense of matching observations at all other redshifts. This once again suggests the need for very efficient grain growth in the early universe. (Figure 5.14)
- (vii) Reducing the amount of dust destroyed in the model surprisingly had very little difference on the stellar-dust mass relation, with only a noticeable difference to the relation at $z > 3$, suggesting that the grain growth is running at almost peak efficiency in the fiducial model and that reducing the destruction had little impact. Increasing the amount of dust destroyed had a more significant impact, delaying the growth of dust inside galaxies to match observations all the way until $z=0$. This actually provided a slightly better fit at $z=0$ than our normal model, by flattening the relation at the high mass end, though at the expense of matching observations at all other redshifts.

In summary, the new dust model manages to find success in reproducing the normalisation of observations in the stellar-dust mass plane for a wide range of redshifts. Tests have shown that grain growth is the most efficient dust production mechanism in our model

by far, and that a relatively short dust accretion timescale is required in order to match observations at the highest redshifts. In the next chapter we will extend the predictions of the model to look at a wider range of dust properties, as well as running the model on the full Millennium and Millennium-II simulations.

Chapter 6

The dust properties of galaxies in the L-GALAXIES SAM

This chapter of the thesis presents the final predictions of the dust properties of galaxies using our detailed dust model and the L-GALAXIES SAM. This includes the modelling of the formation and destruction of dust through physical processes, such as the contribution of AGB stars, supernovae and grain growth inside molecular clouds. Now that the dust model is fully integrated into L-GALAXIES, the model is run using both the Millennium and Millennium-II simulations in order to make use of both the high mass resolution of Millennium-II, and the large volume of Millennium. The majority of the results presented in this section show results from both simulations, assuming that the simulations converge at $\sim 10^9 M_{\odot}$. For redshifts $z \leq 5$ we use both simulations, but at higher redshifts we restrict ourselves to using Millennium-II only. Unless otherwise stated, we restrict our samples to central star forming galaxies in order to select galaxies most comparable to those identified in observational surveys.

6.1 Stellar-Dust Mass relation

The relationship between the stellar mass and the dust mass of galaxies is the relation we focused on during the development of the model, in part due to the large number of observational constraints available over a large redshift range. In the previous chapter we discussed this relation in great detail, particularly at $z=0$. In this chapter, we extend that discussion to a larger number of redshifts ($0 < z < 8$) and a much larger number of galaxies by using the full Millennium and Millennium-II simulations, rather than just one tree file representing 1/512 of the total volume. Figure 6.1 shows the new stellar-dust

mass relation. The 2D histogram represents individual galaxies from the simulation, while the black line shows the median result. The coloured points show observational data.

At $z=0$, we find a good fit to the normalisation and shape of the observations, particularly for low and intermediate masses. Despite a very good fit to the [Ciesla et al. \(2014\)](#) observations, on the whole, we over predict the amount of dust in the most massive galaxies. The observations tend to show a flattening in the relation after $10^{10}M_{\odot}$ which we don't see in the simulation. At higher redshifts, observations are typically only available for more massive galaxies, but we generally see that the model provides a good fit to the normalisation until $z=6$. At very high redshift ($z=6-7$), our median result is under the observations, but they are within the scatter of the histogram. We should note that the majority of high-redshift observations often come from a single measurement in the FIR. The dustiest galaxies will provide the strongest FIR flux, and so we may have an observational bias towards the dustiest galaxies at high redshift. This may explain why our median result is too low but the observations lay within the scatter of our histogram and this is likely to improve as we observe more galaxies at high redshifts. Indeed, the histogram reveals that the scatter in our model and the observations matches particularly well at all redshifts.

The 2D histogram also reveals information about the evolution of the dust masses in our model galaxies, with the transition from low to high dust masses clearly visible when galaxies begin to be dominated by the grain growth in molecular clouds process. At $z=0$, we see that the scatter in our model across this transition matches the observations from [Rémy-Ruyer et al. \(2015\)](#) relatively well.

6.2 Dust to gas and dust to metal ratios

While the stellar-dust mass relation is an important and interesting test of our model, perhaps a better one is how well the model compares with observations of the dust-to-gas and dust-to-metal ratio. These quantities not only test our dust model but also the underlying SAM. In this section, we explore how these ratios vary with stellar mass and with metallicity.

6.2.1 Dust to gas ratios

The dust to gas mass ratio (hereafter DTG) describes the ratio between the total dust content of a galaxy and the total cold gas mass. We compare this to two different properties, first, to see how the DTG ratio varies with stellar mass in [Figure 6.2](#), and secondly

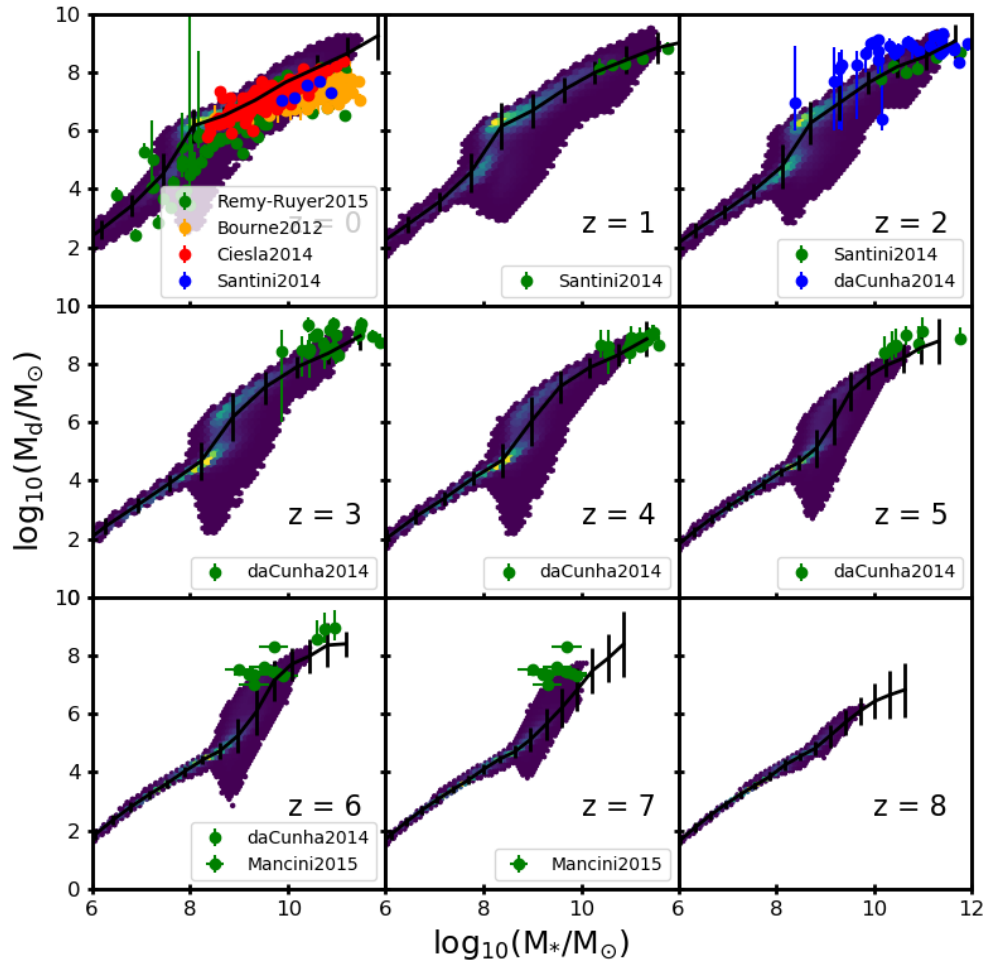


Figure 6.1: The stellar-dust mass relation for redshifts $z=0-8$. The purple points show a 2D histogram of individual galaxies in our model and the black line shows the median. Red, green, orange and blue points show the observational constraints from Ciesla et al. (2014), Rémy-Ruyer et al. (2015), Bourne et al. (2012) and Santini et al. (2014) respectively.

how the DTG ratio varies with oxygen abundance, as seen in Figure 6.3.

Unfortunately, there are not many observational constraints available to compare our model with, especially at $z > 0$, in part due to the difficulty in measuring hydrogen at high redshift. In Figure 6.2, we compare the DTG ratio of our model with observations from Rémy-Ruyer et al. (2015). We find that the median value of our model fits the observations relatively well, particularly above $10^8 M_\odot$, though we appear to have less scatter in our model than we see in the observations at $z=0$. At the low mass end, the scatter in the observations is huge, but may be suggesting a much steeper increase in normalisation than we see in the model as stellar mass increases. We do however see an increased scatter at the low mass end at higher redshifts, but this has gone by $z=0$.

The relationship between the DTG ratio and the oxygen abundance in Figure 6.3 shows the first time we have compared the gas, metals and dust in one plot. Once again, only the Rémy-Ruyer et al. (2015) observations are available to us at $z=0$, with no constraints available at higher redshifts. We find that the model can match the shape and normalisation for $6 < 12 + \log(\text{O}/\text{H}) < 8.5$, but that for very high oxygen abundance, we see that we have too much dust. This agrees with the stellar-dust relation showing that we have too much dust in massive galaxies at $z=0$. We also see much less scatter in the model than the observations at $z=0$.

At higher redshifts we see the bimodal relation we first saw in Figure 6.1, where we see galaxies transitioning to higher normalisations once the grain growth mechanism begins. As time progresses, we see the median value switch from favouring the lower relation to the higher one, as more galaxies begin growing more dust. By $z=0$, grain growth totally dominates the relationship.

6.2.2 Dust to metal ratios

The dust-to-metal ratio (hereafter DTM) describes the ratio of the total dust mass and the total metal mass. The DTM ratio is an important test of our model, as metals are required in order to create dust. Though we keep our metals and dust as distinct quantities in our model, we include dust in the calculation of the metal mass in the DTM ratio, as this is what observers measure.

Figure 6.4 shows how the DTM ratio varies with stellar mass. The DTM ratio observations from Rémy-Ruyer et al. (2015) are converted from the oxygen abundances, assuming that $12 + \log(\text{O}/\text{H}) = 8.69$ corresponds to Z_\odot . This gas-phase metallicity is then converted into a metal mass by multiplying by the cold gas mass.

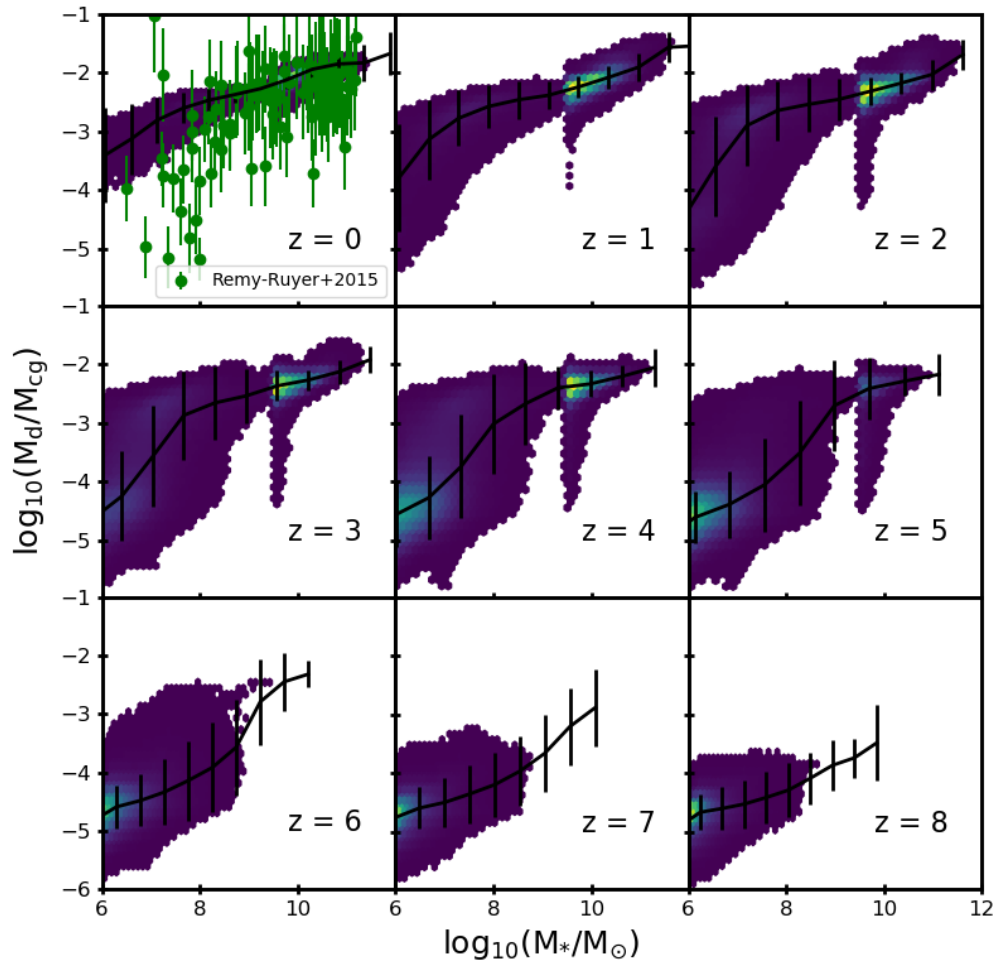


Figure 6.2: The dust-to-gas ratio as a function of stellar mass. The purple points show a 2D histogram of individual galaxies in our model and the black line shows the median. Green points show the observational constraints from [Rémy-Ruyer et al. \(2015\)](#).

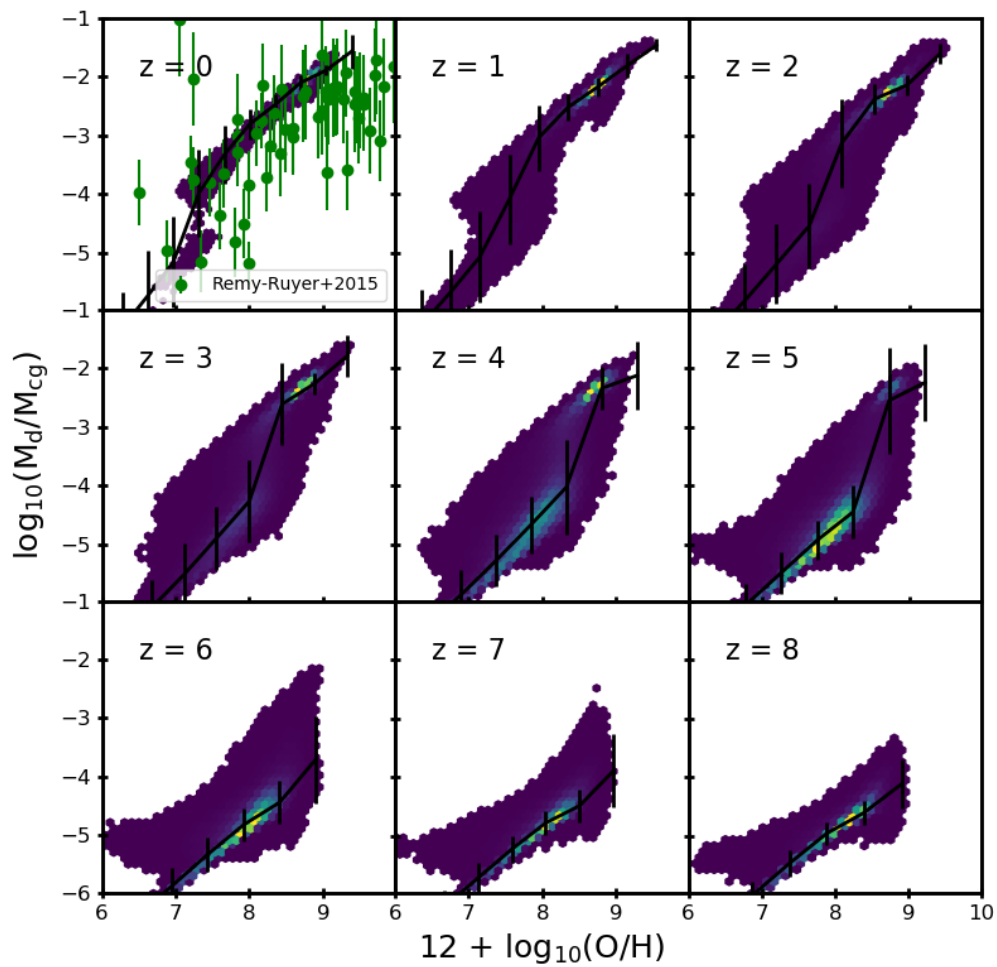


Figure 6.3: The dust-to-gas ratio as a function of oxygen abundance. The purple points show a 2D histogram of individual galaxies in our model and the black line shows the median. Green points show the observational constraints from [Rémy-Ruyer et al. \(2015\)](#).

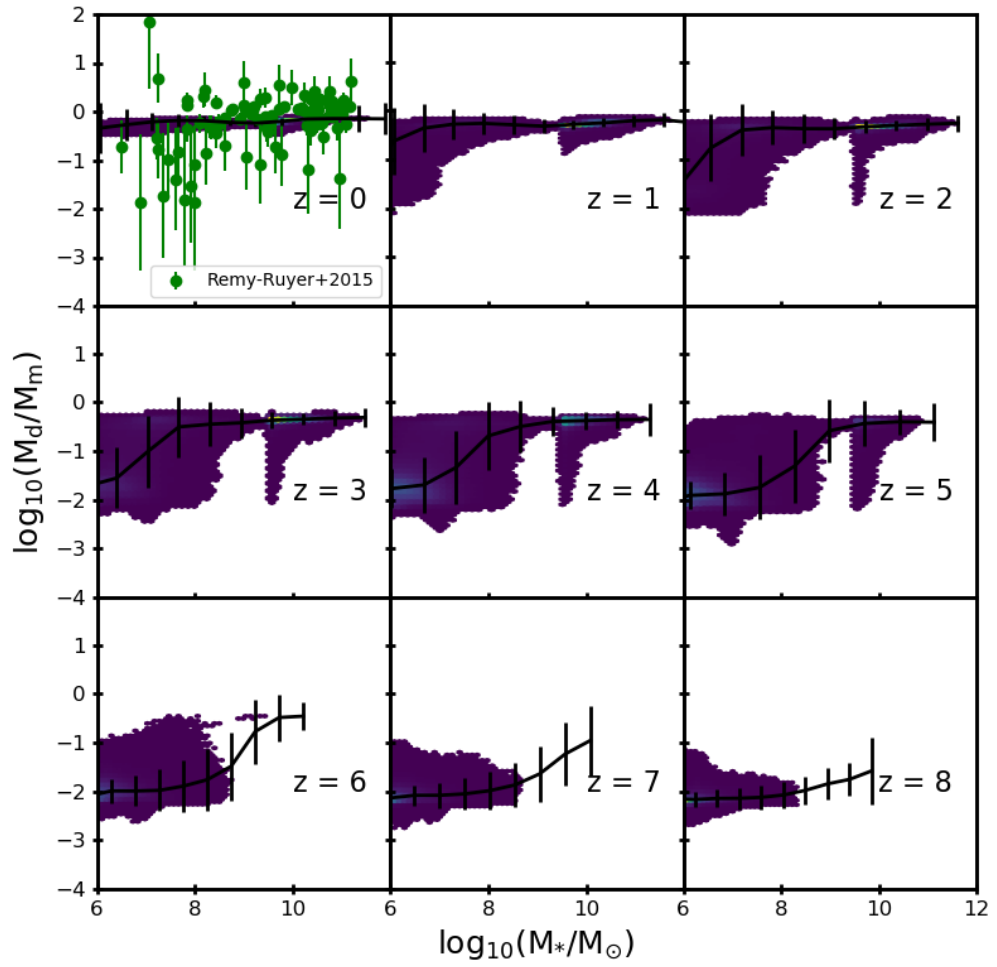


Figure 6.4: The dust-to-metal ratio as a function of stellar mass. The purple points show a 2D histogram of individual galaxies in our model and the black line shows the median. Green points show the observational constraints from [Rémy-Ruyer et al. \(2015\)](#).

The first thing to note is that the median model DTM ratio is very flat at $z=0$, showing no stellar mass dependence. This is also true for all but the lowest mass galaxies until $z=4$. At higher redshifts, we do see a stellar mass dependence in the relation, and what we are seeing is the switch on of the grain growth process in massive galaxies. We also see a slight increase in the normalisation with time. The underlying histogram also shows increased scatter at the low mass end, increasingly so as we go to higher redshifts up to $z=5$.

Interestingly, the observations show a scatter in the DTM ratio that covers over three orders of magnitudes, which is not something we see in the model at $z=0$. Instead we see a very flat relation with a very small scatter, though our model runs pretty much through the middle of the observations, which also show no stellar mass dependence.

Figure 6.5 shows the DTM ratio as a function of oxygen abundance. We compare with observations from Rémy-Ruyer et al. (2015) once again, but now also include measurements of the DTM ratio from gamma ray bursts (GRBs) at higher redshift (Wiseman et al., 2017). At $z=0$ we match the normalization of the observations in the range $7.5 < 12+\log(\text{O}/\text{H}) < 8.5$ but fail to match the shape. The observations show a very steep relation, where as the model shows a much flatter relation. At higher redshifts, we match the GRB observations well at $z=2$ and $z=4$, though at $z=3$ we find that our median values miss the observed galaxies but they are within the scatter shown by the underlying 2D histogram.

6.3 Dust formation rates

The detailed dust model we have built includes the modelling of several different dust production and destruction mechanisms that all contribute to the final dust properties of the galaxies in our model. As discussed previously in Chapter 4, in the literature it has long been argued how important each of the individual processes are in the production of dust in the Universe. One of the benefits of modelling these processes across all of time is that we can look at each one individually and see how they much they contribute to the final dust mass, and also look at how they evolve with time.

Figure 6.6 shows the dust production (or destruction) rate density in the ISM for galaxies in our model across a large redshift range. This plot only includes galaxies in the Millennium simulation, and so we impose a selection for galaxies to have a stellar mass $>10^9 M_{\odot}$ in order to remove galaxies below the mass resolution. We also plot the star formation rate density for comparison, and we can see that overall, the dust production

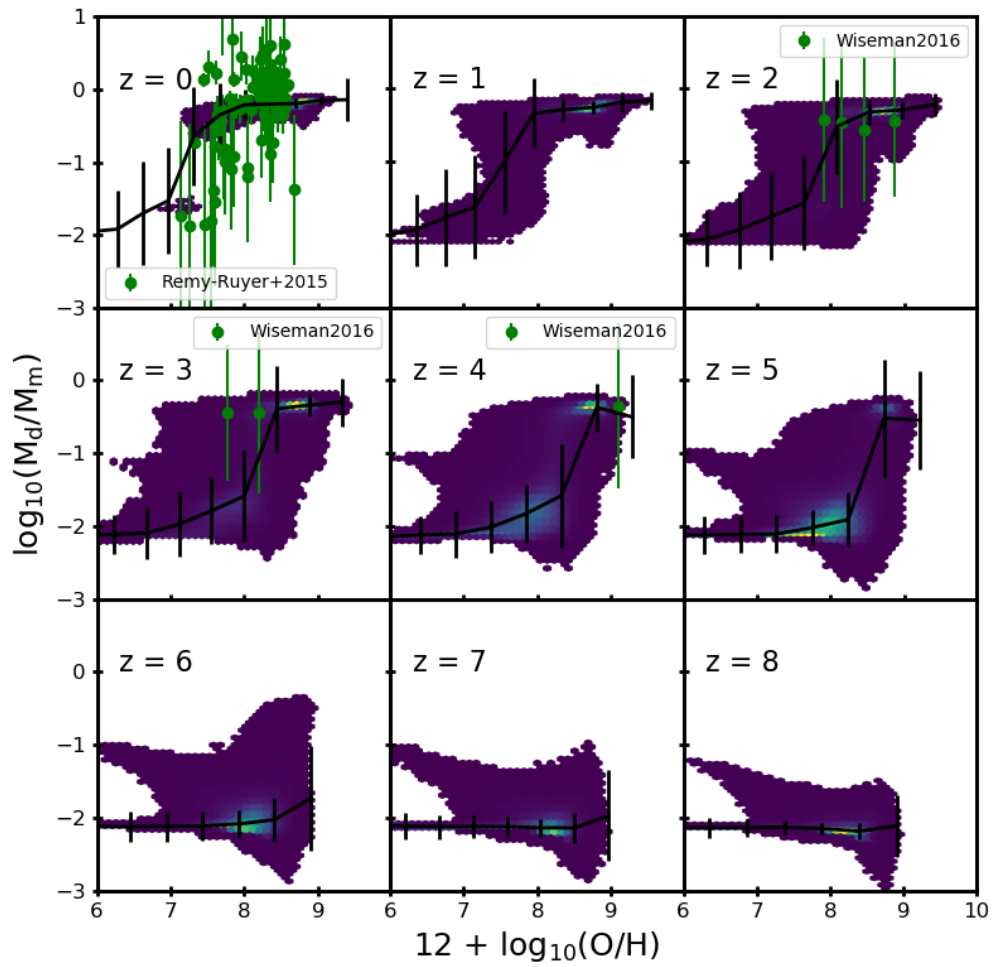


Figure 6.5: The dust-to-metal ratio as a function of oxygen abundance. The purple points show a 2D histogram of individual galaxies in our model and the black line shows the median. Green points show the observational constraints from [Rémy-Ruyer et al. \(2015\)](#).

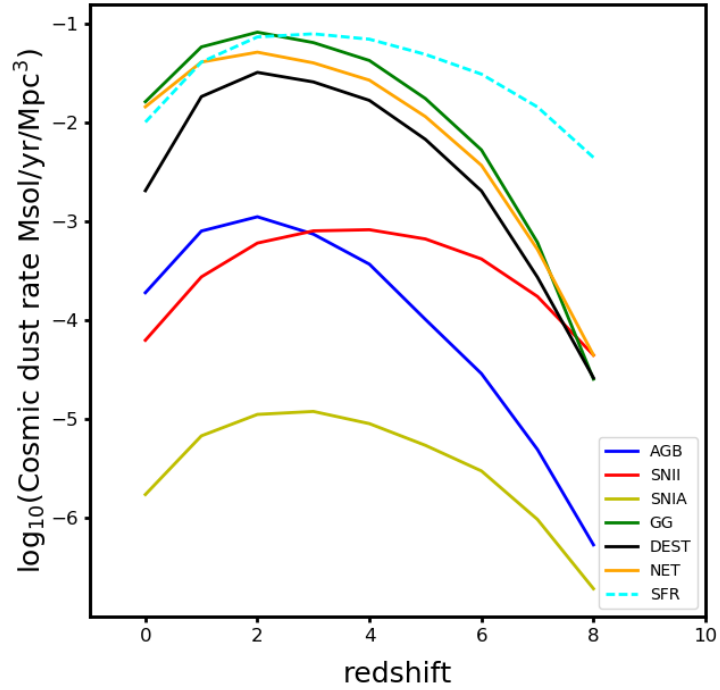


Figure 6.6: The production rate of dust through different mechanisms as a function of redshift. Red, blue and yellow lines show the contribution from stellar sources of dust production, type II supernovae, AGB stars and type Ia supernovae respectively. The green line shows the contribution from grain growth inside molecular clouds. The black line shows the dust destruction rate. The orange line shows the sum of all production processes and takes into account the destruction, and is thus the total dust production rate. We also plot the star formation rate density as a dashed cyan line for comparison.

rate follows the star formation rate in that it rises up to a peak at around $z \sim 2$, and then decreases down to $z=0$. Dust production following the star formation makes sense, as stars are needed to enrich their environments with the metals needed to produce dust.

We can see that grain growth in molecular clouds dominates the production of dust for almost all of time, over taking type II supernovae at $z=8$ and rapidly increasing towards its peak at $z=2$. We also find that we have a higher overall production rate of dust between $z=0$ and $z=1$ than we do for star formation. The destruction rate closely follows the net production rate, suggesting that any dust produced is recycled quickly. It is only at late times that the destruction rate starts to deviate from the net production rate, and that's due to a decrease in supernovae activity which are responsible for dust destruction.

If we look at the stellar contributions to the dust content, we see that they have production rates at least two orders of magnitude lower than that from grain growth at intermediate redshifts. Type II supernovae are found to dominate the stellar production at early times, but peaks at $z \sim 2$, closely following the shape of the star formation rate as you would expect. AGB stars rapidly ramp up their production from $z=8$ up to their peak at $z=2$ as more of the lower mass stars leave their main sequence hydrogen burning phase and begin contributing to the dust content. We find that they begin to dominate type II supernovae after $z=3$. Type Ia supernovae never have a significant impact on the dust production rate, though this may be hindered in our model by the majority of type Ia supernovae going off in the bulge, where we assume dust is immediately destroyed due to higher gas phase temperatures.

We can also look at how the dust production rates vary with stellar mass as well as redshift, and this is shown in Figure 6.7. In this plot, we see that the production of dust in low mass galaxies is always dominated by stellar production mechanisms, in particular type II supernovae, though the difference between type II supernovae and AGB stars decreases over time. In high mass galaxies, we find that the dust production rate is always dominated by grain growth, and increasingly down to intermediate mass galaxies as time progresses. Interestingly, both types of supernovae dominate the AGB dust production rate at $M_* < 10^7 M_\odot$, apart from at $z=0$, but AGB production is equal to, or surpasses, the supernovae rate for high mass galaxies after $z=3$.

6.4 Evolution

The evolution of these relations with time is another interesting thing we can look at. Figure 6.8 shows the evolution of the stellar-dust relation, DTG-stellar relation and the

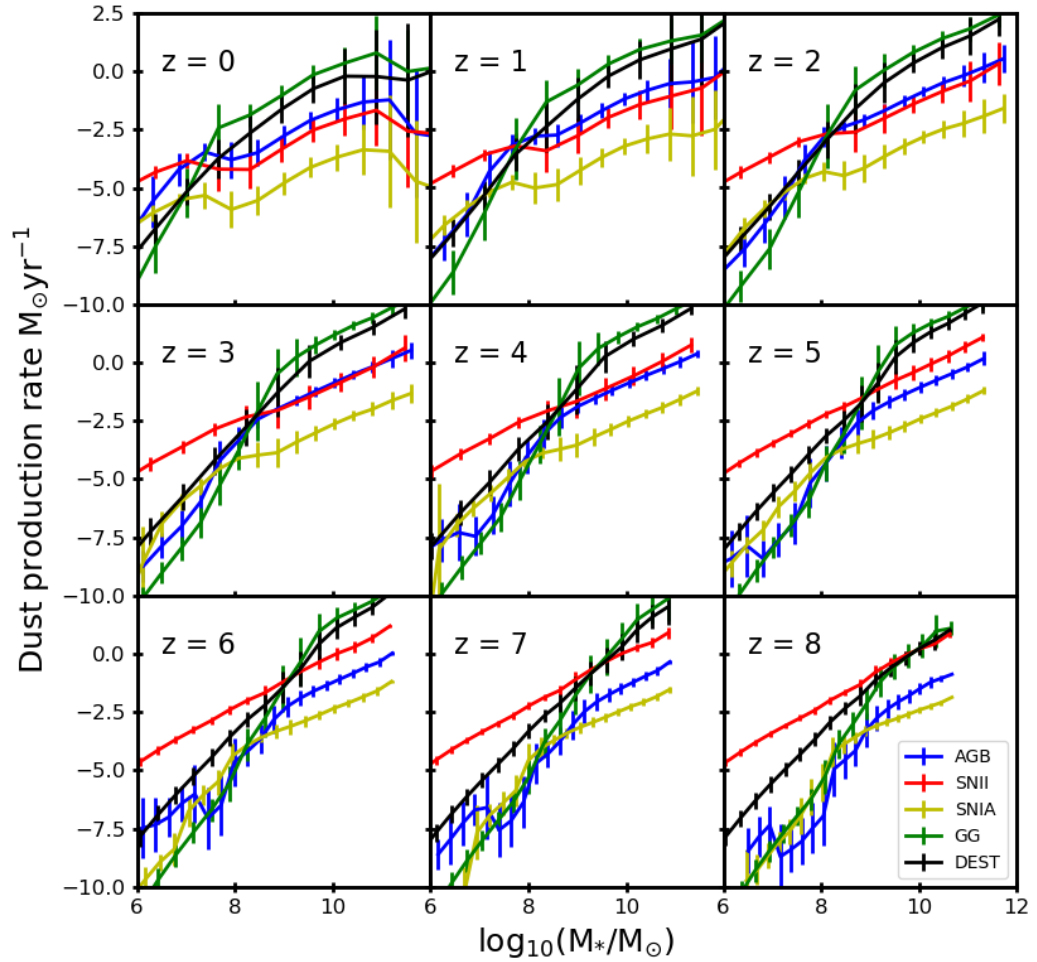


Figure 6.7: The production rate of different dust mechanisms as a function of stellar mass, shown at different redshifts $z=0-8$. Red, blue and yellow lines show the contribution from stellar sources of dust production, type II supernovae, AGB stars and type Ia supernovae respectively. The green line shows the contribution from grain growth inside molecular clouds. The black line shows the dust destruction rate.

DTM-stellar relation for redshifts $z=0-8$, as shown previously in Figures 6.1, 6.2 and 6.4 respectively.

Interestingly, the DTG-stellar relation and the stellar-dust mass relation (above $10^{10}M_{\odot}$) show no real evolution with time after $z=6$, with the median result from the stellar-dust relation is almost identical above 10^9M_{\odot} . Below this mass we see the ramp up in dust production once the grain growth mechanism starts to dominate, and this step in the relation shifts to lower masses as time goes on. We find much more evolution at low to intermediate masses for the DTG ratio with both relations showing a stellar mass dependence, with increasing dust mass, or increasing DTG ratio with increasing stellar mass.

We do see more evolution in the DTM-stellar mass relation, with a trend toward higher DTM ratios as time progresses, suggesting that more and more metals are converted into dust as time progresses. Interestingly, this relation is almost flat for high mass galaxies after $z=5$, suggesting little to no stellar mass dependence on the DTM ratio above $\sim 10^9M_{\odot}$.

Some observers have suggested (Santini et al., 2014) that the dust mass in galaxies could be a function of the physical properties of a galaxy alone, such as the stellar mass and star formation rate, and completely independent of time, which is something our model would agree with for the highest mass galaxies giving the evolution shown in Figure 6.8, once grain growth is well established in a galaxy. At lower masses, when stellar sources of dust production dominate, we tend to see much more evolution with time. It is also standard practice in the literature to make assumptions that the dust mass of a galaxy is a percentage of its total cold gas mass or total metal mass. We find that this is only a good approximation in galaxies with stellar masses greater than $10^{10}M_{\odot}$.

6.5 Dust mass function

The dust mass function compares how the number density of galaxies varies as a function of the galaxies dust mass, and you'd expect it to follow a similar relation to the stellar mass function, with galaxies with less dust more common than massive galaxies with a higher dust mass.

Figure 6.9 shows the dust mass function for redshifts $z=0-8$. The red line shows the results of the Millennium-II simulation, and the black line the Millennium simulation. We compare with observations from Vlahakis et al. (2005) and Clemens et al. (2013) at $z=0$. We find that the model provides a good fit to the Clemens et al. (2013) observations, but over predicts the number density when compared with Vlahakis et al. (2005). We see a

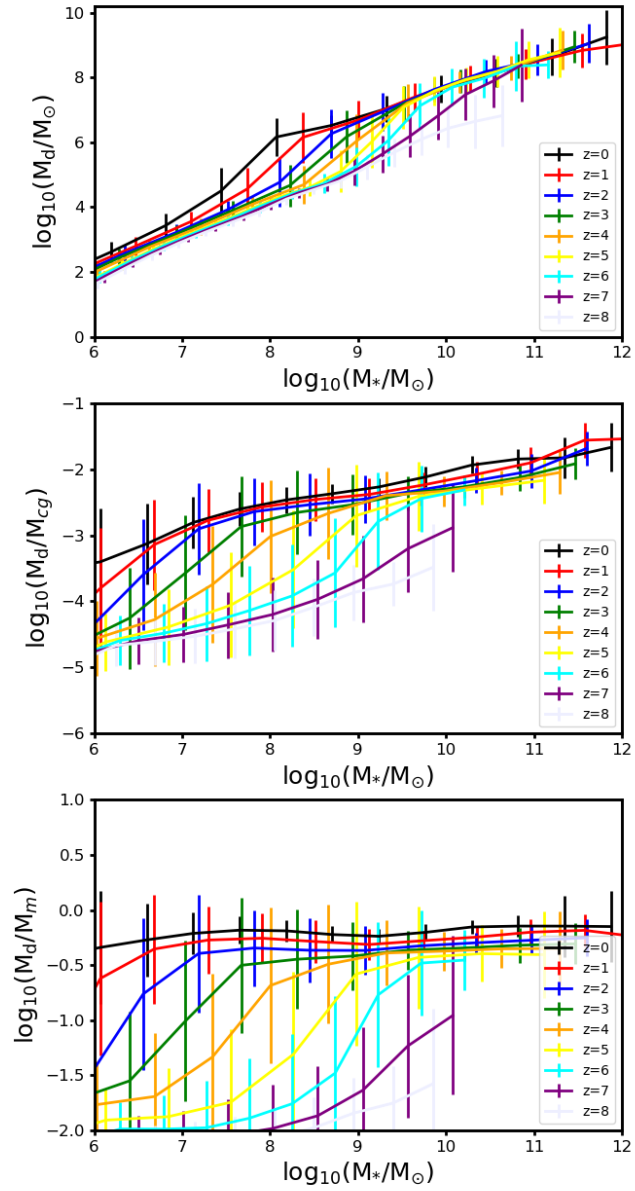


Figure 6.8: The evolution of the stellar-dust relation (top), DTG ratio (central) and DTM ratio (bottom) over a redshift range of $z=0$ -8. This plot combines the different redshift results from Figures 6.1, 6.2 and 6.4 for comparison.

strong evolution in the number density as time goes on, as you'd expect as more galaxies build up their dust content.

6.6 Comparison with other work

The only other comparable study that has implemented a detailed dust model to galaxy formation models on cosmological volumes is the work done by [Popping et al. \(2016\)](#) (hereafter: PS16) using the SANTACRUZ SAM [Somerville and Primack \(1999\)](#). In the same way that our supernovae dust production is based on the mass in metals of key elements returned by supernovae, the PS16 model does this for all stellar sources, including AGB stars rather than use the dust yield tables from [Ferrarotti and Gail \(2006\)](#) as we do. Both models use the [Zhukovska et al. \(2008\)](#) approach for grain growth, though we have a different derivation of the dust accretion timescale, leading to different values. Both models use the same dust destruction timescale from [McKee \(1989\)](#). One of the key differences is that in PS16 they assume that dust can survive outside of the ISM, and model the dust in other gas phases, including its ejection and accretion onto the galaxy from the hot halo. However, their model was run on a grid of haloes for a range of viral masses, where as our model uses the Millennium simulations and thus has a cosmological distribution of haloes with self-consistent histories.

PS16 found success in matching observations of the stellar-dust mass relation in both local and high-redshift galaxies, as well as the DTG ratio as a function of stellar mass, similar to our model. They did find that their stellar-dust mass relation does slowly decrease with time from $z=3$ to $z=0$ but remains constant at higher redshifts.

Where we don't consider the dust content in the CGM or ejected phases of galaxies, PS16 find that a significant reservoir of dust may exist in the CGM, which can be as large, or larger than the amount of dust in the ISM. Their models predict an even larger amount of dust can be ejected from galaxies.

6.7 The first galaxies

So far we have seen that, for the range of redshifts considered ($z=0-8$), that we require a very efficient dust production mechanism in order to match the observed dust properties of galaxies using our model, but also that the dust-to-gas ratio and the stellar-dust mass relation do not vary with redshift for most galaxies (Figure 6.8). In the previous chapter, we saw that stellar sources could not produce enough dust to match observed quantities

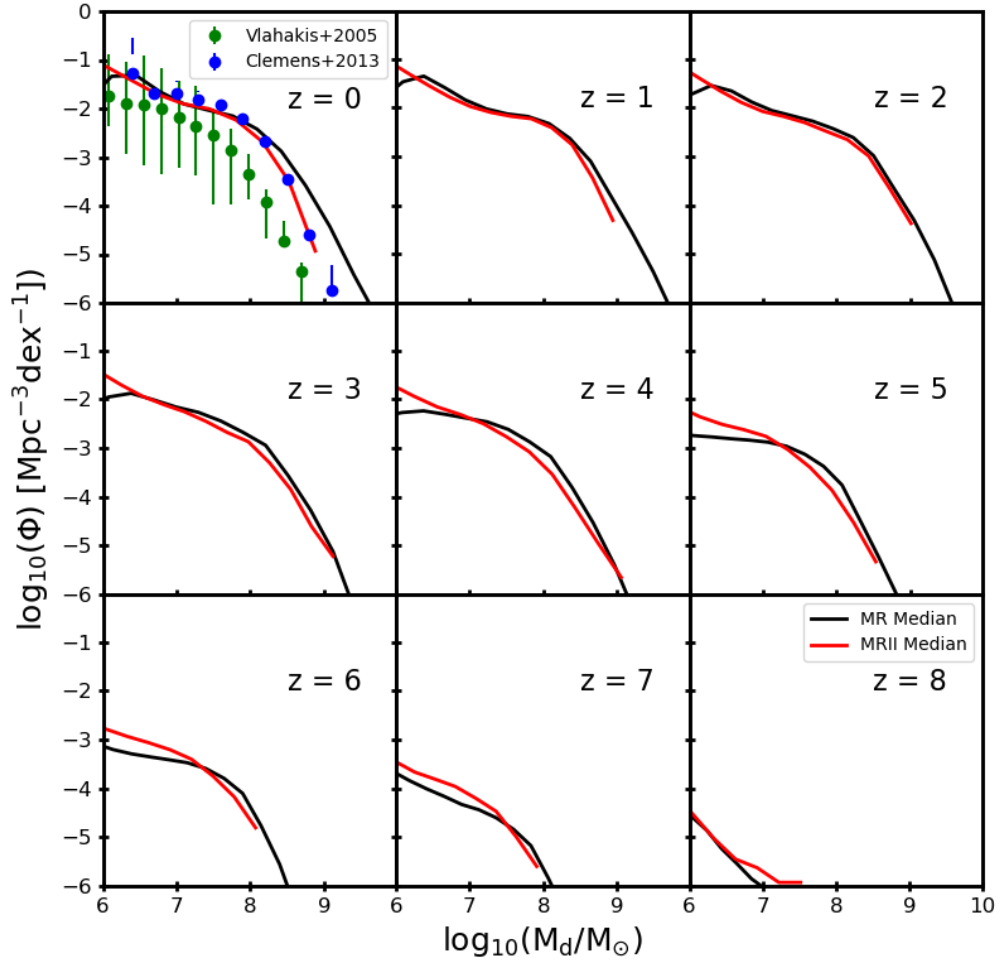


Figure 6.9: The Dust Mass Function (DMF) for redshifts $z=0-8$. The black line shows the prediction of our model using the underlying dark matter Millennium simulation, and the red line for Millennium-II. Observations are taken from [Vlahakis et al. \(2005\)](#) and [Clemens et al. \(2013\)](#) at $z=0$.

at any redshift. These statements all beg the question of what happens at even higher redshifts? Is there a time when stellar sources of dust production are the dominate production source? The first galaxies, which will hopefully be detected by the James Webb Space Telescope (JWST) in the next few years, could potentially have very different dust properties to the observations we have compared the model to so far.

Figure 6.10 shows the stellar-dust mass relation and the dust production rate from AGB stars, supernovae remnants and grain growth for galaxies in the model between $z=8$ and $z=15$. Here we see a slightly different relationship to what we saw in Figure 6.8. We see that type II supernovae dominates the production of dust at these very early times, with the rate of dust production by grain growth closing the difference by $z=8$. As stellar sources of dust dominate the production, we see a linear relationship between the stellar and dust masses for all galaxies, missing the ‘step’ up we saw in Figure 6.8 when the grain growth starts to dominate. This suggests that while the dust properties may vary depending on the stellar mass of a galaxy at later times, with stellar sources dominating low mass galaxies and grain growth dominating more massive galaxies, at these very early times we see that all galaxies are dominated by stellar sources.

As grain dominates the dust production at later times, we considered whether it was worthwhile simulating the stellar sources of dust production at all. While molecular clouds must first be seeded with stellar sources of dust to begin accretion processes, we could approximate this process to produce a simpler model. However, figure 6.10 suggests that modelling the stellar sources of dust is important when considered the very first galaxies.

6.8 Conclusions

In this chapter we have run a modified version of the L-GALAXIES semi-analytic model which includes a prescription of detailed dust modelling on the full Millennium and Millennium-II trees, and provided analysis on a variety of properties relevant to the dust production of galaxies. By combining both of the Millennium simulations we are able to make use of both the higher volume in order to find rarer objects, but also the higher mass resolution of Millennium-II to probe lower mass galaxies. Our conclusions are as follows:

- (i) We find a good fit to the shape and normalisation of the observations in the stellar-dust mass plot over a wide range of redshifts $z=0-7$. A minor inconsistency is the over prediction of dust masses in the highest mass galaxies at $z=0$. Our scatter at $z=0$ is less than that found in the observations (Figure 6.1).

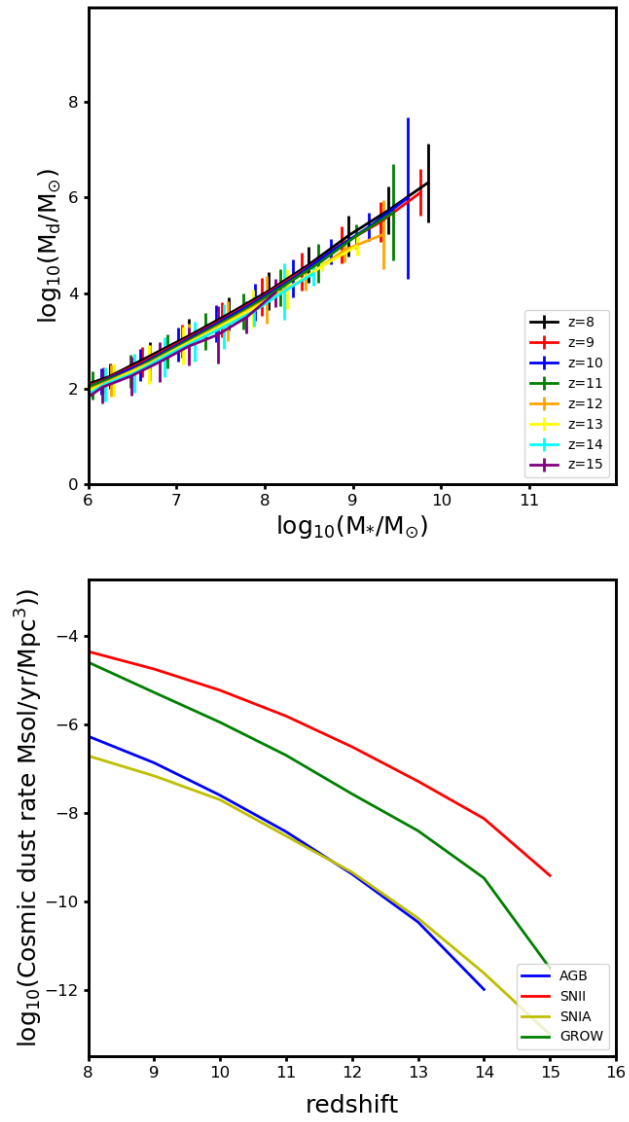


Figure 6.10: The stellar-dust relation (top panel) and the dust production rates (lower panel) for $z=15$ to $z=8$, the redshift range where we may potentially find the first galaxies using JWST.

- (ii) Despite a lack of observational constraints when analysing the dust-to-gas mass ratio, especially at higher redshift, we find a good fit to the shape and normalisation of the DTG ratio vs. stellar mass. The scatter in the observations is found to be larger than the scatter in our model at $z=0$, though the scatter in the model increases dramatically for low mass galaxies, increasingly so at higher redshifts (Figure 6.2).
- (iii) We match the normalisation of the dust-to-metal ratio at $z=0$ where we have observational constraints, though note that there's a much larger scatter in the observations than we have in the model. We also find that the DTM ratio is very flat, with seemingly little to no stellar mass dependence found in the median result. Though we do find increasing scatter in the low mass end, especially at higher redshifts (Figure 6.4).
- (iv) We find a poor fit to the shape of the dust-to-metal and dust-to-gas ratios when plot against the oxygen abundance. Though we tend to match the normalisation around $12+\log(\text{O}/\text{H}) = 8.0$, we see a much steeper relation in the observations than we do in the model (Figures 6.3 and 6.5).
- (v) We need a very efficient dust production mechanism in order to match the observed dust properties of observed high-redshift galaxies, and we get this from dust grain growth in molecular clouds. We also find that the dust destruction rate closely follows the grain growth production rate, suggesting prompt recycling of any dust content, which may explain the observed 'red and dead' dustless elliptical galaxy population at late times (Figure 6.6).
- (vi) We find that in high mass galaxies, there is little evolution in the stellar-dust mass relation, dust-to-gas and dust-to-metal mass ratios. However we do see a stellar mass dependence in the stellar-dust and dust-to-gas ratios, where as the dust-to-metal ratio is increasingly flat with time, and with stellar mass (Figure 6.8).
- (vii) At very early times ($z=8$ to $z=15$), where JWST will hopefully soon observe the first galaxies to form, we find that type II supernovae dominate the production of dust in these galaxies, and find a much stronger evolution in the stellar-dust mass relation with time, as opposed to being independent of redshift at later times (Figure 6.10).

Part IV

Conclusions

Chapter 7

Conclusions

The formation and evolution of galaxies is an interesting subject to study because it incorporates astrophysics from all scales, from the initial perturbations in the early universe creating the large scale structures that produce galaxies, right down to the evolution of stellar populations and their manipulation of the host galaxy. Simulations of galaxy formation allow us to test the various physical recipes against that which is observed in order to build a true and proper picture of what is happening in the real universe. The work presented in this thesis was done using L-GALAXIES, which is a semi-analytic model of galaxy formation built on top of the merger trees from the Millennium dark matter simulation, and is constrained to match certain key observations at low redshift by applying a Monte Carlo Markov Chain (MCMC) method to constrain the free parameters.

Although it lasts less than 0.8 Gyr, the period of the Universe between $z = 7$ and $z = 4$ is important to study because it defines an epoch of interesting galaxy formation and evolution activity. The start of this period marks the end of the epoch of reionization; galaxies are starting to ramp up their metal and dust production; and we are finding evidence of the first quasars. While astronomy is unique in allowing us to observe the Universe at these early times, theoretical modelling is required to interpret those observations in terms of an evolving galaxy population. The rapidly advancing observational constraints on the physical properties of galaxies in the early Universe provide an opportunity to further test and refine these galaxy formation model.

In the second part of this thesis, we used the L-GALAXIES semi-analytic model to make high-redshift predictions, something that was previously unexplored with this model. In Chapter 3, we presented the results of this analysis, showing key observables such as the stellar mass function, UV luminosity function, and star formation rate distribution function. We found that the model starts to deviate from observational constraints at the

highest redshifts, particularly in high mass galaxies. In the case of the UV luminosity function, this is because the current dust model is calibrated at low redshift and lacks sophistication in that it only depends on the cold gas mass and the density of metals. Despite attempts to modify this model, including altering the redshift dependence and replacing the metallicities of model galaxies to observed values, we struggled to find a dust extinction model that agreed with observations at all redshifts.

Motivated by this, we built and implemented a physically motivated dust model into the L-GALAXIES semi-analytic model, and this is explored in the latter parts of this thesis. Dust remains a problem in almost all areas of astronomy due to its obscuration of light throughout the Universe. Thus, understanding the physical properties of dust in galaxies is an important problem to solve. The new model includes prescriptions for the production of dust from all the sources thought to be significant contributors to the dust content in galaxies. These include implementing the mass and metallicity dependent dust yield tables for low mass stars, approximating the dust production in supernovae based on observations of local supernovae remnants, and an efficient grain growth mechanism that accretes metals onto dust grains inside molecular clouds. A model for dust destruction by shocks proportional to the supernovae rate was also implemented.

Our results show that we require a very efficient dust production mechanism on a relatively short timescale in order to match the observed dust properties of galaxies across cosmic time. Longer timescales for grain growth were able to reproduce observations at $z=0$ at the expense of matching the high-redshift observations. Surprisingly, reducing the mass of dust destroyed in the model had little effect on the results at lower redshifts, suggesting that any dust destroyed is rapidly converted back to dust via the grain growth mechanism. Increasing the mass of dust destroyed in the model was able to suppress the growth of dust grains. Models run with only stellar sources of dust production were unable to reproduce the dust content of galaxies at any redshift, often falling short of reproducing the observed dust masses by over two orders of magnitude.

We saw how the dust-to-gas mass ratio and stellar-dust relation did not evolve significantly with time, suggesting that the dust properties of a galaxy are more dependent on the stellar mass or star formation rate of a galaxy, and not a function of time, which agrees with what has been proposed in the literature. The dust-to-metal mass ratio is found to evolve with time, as more metals are accreted onto dust grains the ratio decreases as is expected, though we saw no stellar mass dependence on the dust-to-metal ratio.

We also discussed the dust production rate density as a function of redshift that showed

that the growth of dust grains in molecular clouds is by far the dominant production mechanism across almost all of time. Type II supernovae are shown to be only the dominant production mechanism at very high redshifts ($z > 8$), and closely follows the star formation rate density. AGB stars steadily ramp up their dust production over time, and become the dominant stellar production source at $z > 3$. Type Ia supernovae never have a significant impact on the dust content. Interestingly, we saw how stellar sources of dust production are always dominant in low mass galaxies, even at $z = 0$, but that grain growth is the dominant source of dust in intermediate and high mass galaxies.

7.1 Future Work

Spatial information

In a version of L-GALAXIES currently in development, galaxies are split into rings which each have their own stellar mass, star formation and gas content. It would be interesting to see if the dust model would provide any interesting information on the spatial distribution of dust in galaxies, whether specific production processes favour specific parts of a galaxy, or whether specific areas have different element abundances to elsewhere.

Tuning of the model with MCMC

Several of the free parameters in the dust model, such as the efficiency factor in converting supernovae metals into dust, or the dust accretion timescale, could be constrained with observations using MCMC. This could also include the chemical enrichment model, which was implemented before we considered the effects of dust, and as such, any free parameters could be constrained now considering the effects of the dust model.

Dust extinction

The original intention of the dust model was to use it to reconcile the high redshift luminosity function with observations. Extending the model described in this thesis to convert dust masses into dust extinction values is no easy task, and requires precise information on the distribution of dust inside (and indeed outside) galaxies, as well as assumptions made on the geometry of the dust grains.

A first instance approximation could be made by calculating a V-band attenuation in the same way that observers of gamma ray bursts do, with it being proportional to the dust-to-gas ratio and metallicity, and scaled with milky way values. This could then be

scaled to other wavelengths using a simple reddening law, such as the Calzetti dust law, and applied to the luminosity function.

Similarly, we could also use the new dust properties to produce far infra-red luminosity functions.

Bibliography

- Álvarez-Márquez, J., Burgarella, D., Heinis, S., Buat, V., Lo Faro, B., Béthermin, M., López-Fortín, C. E., Cooray, A., Farrah, D., Hurley, P., Ibar, E., Ilbert, O., Koekoer, A. M., Lemaux, B. C., Pérez-Fournon, I., Rodighiero, G., Salvato, M., Scott, D., Taniguchi, Y., Vieira, J. D., and Wang, L. (2016). Dust properties of Lyman-break galaxies at $z \sim 3$. *AAP*, 587:A122. [xvi](#), [49](#), [50](#)
- Angulo, R. E., Baugh, C. M., Frenk, C. S., and Lacey, C. G. (2014). Extending the halo mass resolution of N-body simulations. *MNRAS*, 442:3256–3265. [12](#)
- Angulo, R. E. and White, S. D. M. (2010). One simulation to fit them all - changing the background parameters of a cosmological N -body simulation. *MNRAS*, 154:143–154. [12](#)
- Arrigoni, M., Trager, S. C., Somerville, R. S., and Gibson, B. K. (2010). Galactic chemical evolution in hierarchical formation models - I. Early-type galaxies in the local Universe. *MNRAS*, 402:173–190. [58](#)
- Baldry, I. K., Driver, S. P., Loveday, J., Taylor, E. N., Kelvin, L. S., Liske, J., Norberg, P., Robotham, A. S. G., Brough, S., Hopkins, A. M., Bamford, S. P., Peacock, J. A., Bland-Hawthorn, J., Conselice, C. J., Croom, S. M., Jones, D. H., Parkinson, H. R., Popescu, C. C., Prescott, M., Sharp, R. G., and Tuffs, R. J. (2012). Galaxy And Mass Assembly (GAMA): the galaxy stellar mass function at $z < 0.06$. *MNRAS*, 421:621–634. [xiii](#), [33](#)
- Baldry, I. K., Glazebrook, K., and Driver, S. P. (2008). On the galaxy stellar mass function, the mass-metallicity relation and the implied baryonic mass function. *MNRAS*, 388:945–959. [xiii](#), [33](#)
- Baugh, C. M. (2006). A primer on hierarchical galaxy formation: the semi-analytical approach. *Reports on Progress in Physics*, 69:3101–3156. [7](#)

- Bautista, M. A., Depoy, D. L., Pradhan, A. K., Elias, J. H., Gregory, B., Phillips, M. M., and Suntzeff, N. B. (1995). Near infrared spectra of SN 1987A: Days 936 to 1445. *AJ*, 109:729–736. [59](#)
- Bernstein, R. A., Freedman, W. L., and Madore, B. F. (2002). The First Detections of the Extragalactic Background Light at 3000, 5500, and 8000 Å. I. Results. *APJ*, 571:56–84. [57](#)
- Bianchi, S. and Schneider, R. (2007). Dust formation and survival in supernova ejecta. *MNRAS*, 378:973–982. [61](#)
- Blitz, L. and Rosolowsky, E. (2006). The Role of Pressure in GMC Formation II: The H₂-Pressure Relation. *APJ*, 650:933–944. [80](#)
- Borkowski, K. J., Williams, B. J., Reynolds, S. P., Blair, W. P., Ghavamian, P., Sankrit, R., Hendrick, S. P., Long, K. S., Raymond, J. C., Smith, R. C., Points, S., and Winkler, P. F. (2006). Dust Destruction in Type Ia Supernova Remnants in the Large Magellanic Cloud. *APJ*, 642:L141–L144. [59](#)
- Bourne, N., Maddox, S. J., Dunne, L., Auld, R., Baes, M., Baldry, I. K., Bonfield, D. G., Cooray, A., Croom, S. M., Dariush, A., de Zotti, G., Driver, S. P., Dye, S., Eales, S., Gomez, H. L., González-Nuevo, J., Hopkins, A. M., Ibar, E., Jarvis, M. J., Lapi, A., Madore, B., Michałowski, M. J., Pohlen, M., Popescu, C. C., Rigby, E. E., Seibert, M., Smith, D. J. B., Tuffs, R. J., van der Werf, P., Brough, S., Buttiglione, S., Cava, A., Clements, D. L., Conselice, C. J., Fritz, J., Hopwood, R., Ivison, R. J., Jones, D. H., Kelvin, L. S., Liske, J., Loveday, J., Norberg, P., Robotham, A. S. G., Rodighiero, G., and Temi, P. (2012). Herschel-ATLAS/GAMA: a census of dust in optically selected galaxies from stacking at submillimetre wavelengths. *MNRAS*, 421:3027–3059. [xvii](#), [xviii](#), [88](#), [89](#), [90](#), [105](#)
- Bouwens, R. J., Aravena, M., Decarli, R., Walter, F., da Cunha, E., Labbé, I., Bauer, F. E., Bertoldi, F., Carilli, C., Chapman, S., Daddi, E., Hodge, J., Ivison, R. J., Karim, A., Le Fevre, O., Magnelli, B., Ota, K., Riechers, D., Smail, I. R., van der Werf, P., Weiss, A., Cox, P., Elbaz, D., Gonzalez-Lopez, J., Infante, L., Oesch, P., Wagg, J., and Wilkins, S. (2016). ALMA Spectroscopic Survey in the Hubble Ultra Deep Field: The Infrared Excess of UV-Selected $z = 2-10$ Galaxies as a Function of UV-Continuum Slope and Stellar Mass. *ApJ*, 833:72. [4](#)

- Bouwens, R. J., Illingworth, G. D., Franx, M., Chary, R.-R., Meurer, G. R., Conselice, C. J., Ford, H., Giavalisco, M., and van Dokkum, P. (2009). UV CONTINUUM SLOPE AND DUST OBSCURATION FROM $z = 6$ TO $z = 2$: THE STAR FORMATION RATE DENSITY AT HIGH REDSHIFT. *ApJ*, 705(1):936–961. [4](#)
- Bouwens, R. J., Illingworth, G. D., Franx, M., and Ford, H. (2007). UV Luminosity Functions at $z = 4, 5$, and 6 from the Hubble Ultra Deep Field and Other Deep Hubble Space Telescope ACS Fields: Evolution and Star Formation History. *APJ*, 670:928–958. [3](#)
- Bouwens, R. J., Illingworth, G. D., Franx, M., and Ford, H. (2008). $z = 7$ -10 Galaxies in the HUDF and GOODS Fields: UV Luminosity Functions. *ApJ*, 686:230–250. [3](#)
- Bouwens, R. J., Illingworth, G. D., González, V., Labbé, I., Franx, M., Conselice, C. J., Blakeslee, J., van Dokkum, P., Holden, B., Magee, D., Marchesini, D., and Zheng, W. (2010a). $z = 7$ GALAXY CANDIDATES FROM NICMOS OBSERVATIONS OVER THE HDF-SOUTH AND THE CDF-SOUTH AND HDF-NORTH GOODS FIELDS. *ApJ*, 725(2):1587–1599. [2](#), [3](#)
- Bouwens, R. J., Illingworth, G. D., Oesch, P., Franx, M., Labbé, I., Trenti, M., van Dokkum, P., Carollo, C. M., González, V., Smit, R., and Magee, D. (2012). UV-CONTINUUM SLOPES AT $z = 4$ -7 FROM THE HUDF09+ERS+CANDELS OBSERVATIONS: DISCOVERY OF A WELL-DEFINED UV COLOR-MAGNITUDE RELATIONSHIP FOR $z = 4$ STAR-FORMING GALAXIES. *ApJ*, 754(2):83. [4](#), [30](#)
- Bouwens, R. J., Illingworth, G. D., Oesch, P. A., Labbé, I., Trenti, M., van Dokkum, P., Franx, M., Stiavelli, M., Carollo, C. M., Magee, D., and Gonzalez, V. (2011). Ultraviolet Luminosity Functions from 132 $z = 7$ and $z = 8$ Lyman-break Galaxies in the Ultra-deep HUDF09 and Wide-area Early Release Science WFC3/IR Observations. *ApJ*, 737:90. [2](#), [3](#)
- Bouwens, R. J., Illingworth, G. D., Oesch, P. A., Labbé, I., van Dokkum, P. G., Trenti, M., Franx, M., Smit, R., Gonzalez, V., and Magee, D. (2014). UV-continuum Slopes of $\lambda_{4000} z = 4$ -8 Galaxies from the HUDF/XDF, HUDF09, ERS, CANDELS-South, and CANDELS-North Fields. *ApJ*, 793:115. [4](#)
- Bouwens, R. J., Illingworth, G. D., Oesch, P. a., Stiavelli, M., van Dokkum, P., Trenti, M., Magee, D., Labbé, I., Franx, M., Carollo, C. M., and Gonzalez, V. (2010b). DIS-

COVERY OF $z = 8$ GALAXIES IN THE HUBBLE ULTRA DEEP FIELD FROM ULTRA-DEEP WFC3/IR OBSERVATIONS. *ApJ*, 709(2):L133–L137. [3](#), [4](#)

- Bouwens, R. J., Illingworth, G. D., Oesch, P. A., Trenti, M., Labbé, I., Bradley, L., Carollo, M., van Dokkum, P. G., Gonzalez, V., Holwerda, B., Franx, M., Spitler, L., Smit, R., and Magee, D. (2015). UV Luminosity Functions at Redshifts $z \sim 4$ to $z \sim 10$: 10,000 Galaxies from HST Legacy Fields. *ApJ*, 803:34. [xv](#), [3](#), [44](#), [45](#), [46](#), [47](#), [48](#)
- Bower, R. G., Benson, A. J., Malbon, R., Helly, J. C., Frenk, C. S., Baugh, C. M., Cole, S., and Lacey, C. G. (2006). Breaking the hierarchy of galaxy formation. *MNRAS*, 370:645–655. [8](#)
- Bowler, R. A. A., Dunlop, J. S., McLure, R. J., McCracken, H. J., Milvang-Jensen, B., Furusawa, H., Taniguchi, Y., Le Fèvre, O., Fynbo, J. P. U., Jarvis, M. J., and Häußler, B. (2015). The galaxy luminosity function at $z \sim 6$ and evidence for rapid evolution in the bright end from $z \sim 7$ to 5. *MNRAS*, 452:1817–1840. [xv](#), [44](#), [45](#), [46](#)
- Bowler, R. A. A., Dunlop, J. S., McLure, R. J., Rogers, A. B., McCracken, H. J., Milvang-Jensen, B., Furusawa, H., Fynbo, J. P. U., Taniguchi, Y., Afonso, J., Bremer, M. N., and Le Fèvre, O. (2014). The bright end of the galaxy luminosity function at $z \sim 7$: before the onset of mass quenching? *MNRAS*, 440:2810–2842. [xv](#), [44](#), [45](#), [46](#)
- Boylan-Kolchin, M., Springel, V., White, S. D. M., Jenkins, A., and Lemson, G. (2009). Resolving cosmic structure formation with the Millennium-II Simulation. *MNRAS*, 398:1150–1164. [10](#), [11](#)
- Brandt, T. D., Tojeiro, R., Aubourg, É., Heavens, A., Jimenez, R., and Strauss, M. A. (2010). The Ages of Type Ia Supernova Progenitors. *AJ*, 140:804–816. [18](#), [19](#)
- Bruzual, G. and Charlot, S. (2003). Stellar population synthesis at the resolution of 2003. *MNRAS*, 344:1000–1028. [29](#)
- Bruzual A., G. and Charlot, S. (1993). Spectral evolution of stellar populations using isochrone synthesis. *APJ*, 405:538–553. [29](#)
- Bunker, A. J., Wilkins, S., Ellis, R. S., Stark, D. P., Lorenzoni, S., Chiu, K., Lacy, M., Jarvis, M. J., and Hickey, S. (2010). The contribution of high-redshift galaxies to cosmic reionization: new results from deep WFC3 imaging of the Hubble Ultra Deep Field. *MNRAS*, 409:855–866. [2](#), [3](#), [4](#)

- Calura, F., Recchi, S., Matteucci, F., and Kroupa, P. (2010). Effects of the integrated galactic IMF on the chemical evolution of the solar neighbourhood. *MNRAS*, 406:1985–1999. [61](#)
- Casey, C. M., Scoville, N. Z., Sanders, D. B., Lee, N., Cooray, A., Finkelstein, S. L., Capak, P., Conley, A., De Zotti, G., Farrah, D., Fu, H., Le Floch, E., Ilbert, O., Ivison, R. J., and Takeuchi, T. T. (2014). Are Dusty Galaxies Blue? Insights on UV Attenuation from Dust-selected Galaxies. *APJ*, 796:95. [xvi](#), [49](#), [50](#)
- Castellano, M., Sommariva, V., Fontana, A., Pentericci, L., Santini, P., Grazian, A., Amorin, R., Donley, J. L., Dunlop, J. S., Ferguson, H. C., Fiore, F., Galametz, A., Giallongo, E., Guo, Y., Huang, K.-H., Koekemoer, A., Maiolino, R., McLure, R. J., Paris, D., Schaerer, D., Troncoso, P., and Vanzella, E. (2014). Constraints on the star-formation rate of $z \sim 3$ LBGs with measured metallicity in the CANDELS GOODS-South field. *AAP*, 566:A19. [xvi](#), [50](#)
- Cernuschi, F. and Codina, S. (1967). Critical Considerations on the Theories of Formation of Carbon Cosmic Grains. *AJ*, 72:788. [58](#)
- Chabrier, G. (2003). Galactic Stellar and Substellar Initial Mass Function. *PASP*, 115:763–795. [8](#), [15](#), [28](#)
- Charlot, S. and Bruzual, A. G. (1991). Stellar population synthesis revisited. *APJ*, 367:126–140. [29](#)
- Ciesla, L., Boquien, M., Boselli, A., Buat, V., Cortese, L., Bendo, G. J., Heinis, S., Galametz, M., Eales, S., Smith, M. W. L., Baes, M., Bianchi, S., De Looze, I., di Serego Alighieri, S., Galliano, F., Hughes, T. M., Madden, S. C., Pierini, D., Rémy-Ruyer, A., Spinoglio, L., Vaccari, M., Viaene, S., and Vlahakis, C. (2014). Dust spectral energy distributions of nearby galaxies: an insight from the Herschel Reference Survey. *AAP*, 565:A128. [xvii](#), [xviii](#), [88](#), [89](#), [90](#), [101](#), [104](#), [105](#)
- Clay, S. J., Thomas, P. A., Wilkins, S. M., and Henriques, B. M. B. (2015). Galaxy formation in the Planck cosmology - III. The high-redshift universe. *MNRAS*, 451:2692–2702. [35](#)
- Clemens, M. S., Negrello, M., De Zotti, G., Gonzalez-Nuevo, J., Bonavera, L., Cosco, G., Guarese, G., Boaretto, L., Salucci, P., Baccigalupi, C., Clements, D. L., Danese, L., Lapi, A., Mandolesi, N., Partridge, R. B., Perrotta, F., Serjeant, S., Scott, D., and

- Toffolatti, L. (2013). Dust and star formation properties of a complete sample of local galaxies drawn from the Planck Early Release Compact Source Catalogue. *MNRAS*, 433:695–711. [xx](#), [115](#), [118](#)
- Cohen, M., Kuhl, L. V., and Barlow, M. J. (1975). Wolf-Rayet stars. VI - The nature of the optical and infrared continua. *AAP*, 40:291–302. [59](#)
- Cole, S., Lacey, C. G., Baugh, C. M., and Frenk, C. S. (2000). Hierarchical galaxy formation. *MNRAS*, 319:168–204. [8](#)
- Colless, M., Dalton, G., Maddox, S., Sutherland, W., Norberg, P., Cole, S., Bland-Hawthorn, J., Bridges, T., Cannon, R., Collins, C., Couch, W., Cross, N., Deeley, K., De Propriis, R., Driver, S. P., Efstathiou, G., Ellis, R. S., Frenk, C. S., Glazebrook, K., Jackson, C., Lahav, O., Lewis, I., Lumsden, S., Madgwick, D., Peacock, J. A., Peterson, B. A., Price, I., Seaborne, M., and Taylor, K. (2001). The 2dF Galaxy Redshift Survey: spectra and redshifts. *MNRAS*, 328:1039–1063. [12](#)
- Cowie, L. L. (1978). Refractory grain destruction in low-velocity shocks. *APJ*, 225:887–892. [60](#)
- Croton, D. J., Springel, V., White, S. D. M., De Lucia, G., Frenk, C. S., Gao, L., Jenkins, a., Kauffmann, G., Navarro, J. F., and Yoshida, N. (2006). The many lives of active galactic nuclei: cooling flows, black holes and the luminosities and colours of galaxies. *MNRAS*, 365(1):11–28. [8](#), [9](#), [22](#)
- Cucchiara, A., Veres, P., Corsi, A., Cenko, S. B., Perley, D. A., Lien, A., Marshall, F. E., Pagani, C., Toy, V. L., Capone, J. I., Frail, D. A., Horesh, A., Modjaz, M., Butler, N. R., Littlejohns, O. M., Watson, A. M., Kutyrev, A. S., Lee, W. H., Richer, M. G., Klein, C. R., Fox, O. D., Prochaska, J. X., Bloom, J. S., Troja, E., Ramirez-Ruiz, E., de Diego, J. A., Georgiev, L., González, J., Román-Zúñiga, C. G., Gehrels, N., and Moseley, H. (2015). Happy Birthday Swift: Ultra-long GRB 141121A and Its Broadband Afterglow. *APJ*, 812:122. [69](#)
- da Cunha, E., Charlot, S., and Elbaz, D. (2008). A simple model to interpret the ultraviolet, optical and infrared emission from galaxies. *MNRAS*, 388:1595–1617. [68](#)
- da Cunha, E., Groves, B., Walter, F., Decarli, R., Weiss, A., Bertoldi, F., Carilli, C., Daddi, E., Elbaz, D., Ivison, R., Maiolino, R., Riechers, D., Rix, H.-W., Sargent, M., and Smail, I. (2013). On the Effect of the Cosmic Microwave Background in High-redshift (Sub-)millimeter Observations. *APJ*, 766:13. [69](#)

- Danziger, I. J., Lucy, L. B., Bouchet, P., and Gouiffes, C. (1991). Molecules Dust and Ionic Abundances in Supernova 1987A. In Woosley, S. E., editor, *Supernovae*, page 69. [58](#)
- de Boer, K. S., Jura, M. A., and Shull, J. M. (1987). Diffuse and dark clouds in the interstellar medium. In Kondo, Y., editor, *Exploring the Universe with the IUE Satellite*, volume 129 of *Astrophysics and Space Science Library*, pages 485–515. [60](#)
- De Cia, A., Ledoux, C., Savaglio, S., Schady, P., and Vreeswijk, P. M. (2013). Dust-to-metal ratios in damped Lyman- α absorbers. Fresh clues to the origins of dust and optical extinction towards γ -ray bursts. *AAP*, 560:A88. [69](#)
- De Lucia, G. and Blaizot, J. (2007). The hierarchical formation of the brightest cluster galaxies. *MNRAS*, 375(1):2–14. [8](#), [9](#), [43](#)
- De Lucia, G., Kauffmann, G., and White, S. D. M. (2004). Chemical enrichment of the intracluster and intergalactic medium in a hierarchical galaxy formation model. *MNRAS*, 349(3):1101–1116. [8](#), [9](#), [14](#)
- Dekel, A. and Silk, J. (1986). The origin of dwarf galaxies, cold dark matter, and biased galaxy formation. *APJ*, 303:39–55. [21](#)
- Domínguez Sánchez, H., Pozzi, F., Gruppioni, C., Cimatti, A., Ilbert, O., Pozzetti, L., McCracken, H., Capak, P., Le Floch, E., Salvato, M., Zamorani, G., Carollo, C. M., Contini, T., Kneib, J.-P., Le Fèvre, O., Lilly, S. J., Mainieri, V., Renzini, A., Scodreggio, M., Bardelli, S., Bolzonella, M., Bongiorno, A., Caputi, K., Coppa, G., Cucciati, O., de la Torre, S., de Ravel, L., Franzetti, P., Garilli, B., Iovino, A., Kampczyk, P., Knobel, C., Kovač, K., Lamareille, F., Le Borgne, J.-F., Le Brun, V., Maier, C., Mignoli, M., Pelló, R., Peng, Y., Perez-Montero, E., Ricciardelli, E., Silverman, J. D., Tanaka, M., Tasca, L. A. M., Tresse, L., Vergani, D., and Zucca, E. (2011). The evolution of quiescent galaxies at high redshifts ($z \geq 1.4$). *MNRAS*, 417:900–915. [xiii](#), [33](#)
- Dowell, C. D., Conley, A., Glenn, J., Arumugam, V., Asboth, V., Aussel, H., Bertoldi, F., Béthermin, M., Bock, J., Boselli, A., Bridge, C., Buat, V., Burgarella, D., Cabrera-Lavers, A., Casey, C. M., Chapman, S. C., Clements, D. L., Conversi, L., Cooray, A., Dannerbauer, H., De Bernardis, F., Ellsworth-Bowers, T. P., Farrah, D., Franceschini, A., Griffin, M., Gurwell, M. A., Halpern, M., Hatziminaoglou, E., Heinis, S., Ibar, E., Ivison, R. J., Laporte, N., Marchetti, L., Martínez-Navajas, P., Marsden, G., Morrison,

- G. E., Nguyen, H. T., O'Halloran, B., Oliver, S. J., Omont, A., Page, M. J., Papageorgiou, A., Pearson, C. P., Petitpas, G., Pérez-Fournon, I., Pohlen, M., Riechers, D., Rigopoulou, D., Roseboom, I. G., Rowan-Robinson, M., Sayers, J., Schulz, B., Scott, D., Seymour, N., Shupe, D. L., Smith, A. J., Streblyanska, A., Symeonidis, M., Vaccari, M., Valtchanov, I., Vieira, J. D., Viero, M., Wang, L., Wardlow, J., Xu, C. K., and Zemcov, M. (2014). HerMES: Candidate High-redshift Galaxies Discovered with Herschel/SPIRE. *ApJ*, 780:75. [3](#)
- Draine, B. T. (1990). Evolution of interstellar dust. In Blitz, L., editor, *The Evolution of the Interstellar Medium*, volume 12 of *Astronomical Society of the Pacific Conference Series*, pages 193–205. [60](#)
- Draine, B. T. and Fraisse, A. A. (2009). Polarized Far-Infrared and Submillimeter Emission from Interstellar Dust. *APJ*, 696:1–11. [61](#)
- Duncan, K., Conselice, C. J., Mortlock, A., Hartley, W. G., Guo, Y., Ferguson, H. C., Davé, R., Lu, Y., Ownsworth, J., Ashby, M. L. N., Dekel, A., Dickinson, M., Faber, S., Giavalisco, M., Grogin, N., Kocevski, D., Koekemoer, A., Somerville, R. S., and White, C. E. (2014). The mass evolution of the first galaxies: stellar mass functions and star formation rates at $4 < z < 7$ in the CANDELS GOODS-South field. *MNRAS*, 444:2960–2984. [xiv](#), [xv](#), [2](#), [5](#), [36](#), [37](#), [38](#), [39](#), [44](#), [45](#), [46](#), [47](#), [48](#)
- Dunlop, J. S., Ade, P. A. R., Bock, J. J., Chapin, E. L., Cirasuolo, M., Coppin, K. E. K., Devlin, M. J., Griffin, M., Greve, T. R., Gundersen, J. O., Halpern, M., Hargrave, P. C., Hughes, D. H., Ivison, R. J., Klein, J., Kovacs, A., Marsden, G., Maukopf, P., Netterfield, C. B., Olmi, L., Pascale, E., Patanchon, G., Rex, M., Scott, D., Semisch, C., Smail, I., Targett, T. A., Thomas, N., Truch, M. D. P., Tucker, C., Tucker, G. S., Viero, M. P., Walter, F., Wardlow, J. L., Weiss, A., and Wiebe, D. V. (2010). The BLAST 250 μm -selected galaxy population in GOODS-South. *MNRAS*, 408:2022–2050. [3](#)
- Dunlop, J. S., McLure, R. J., Robertson, B. E., Ellis, R. S., Stark, D. P., Cirasuolo, M., and de Ravel, L. (2012). A critical analysis of the ultraviolet continuum slopes (β) of high-redshift galaxies: no evidence (yet) for extreme stellar populations at $z > 6$. *MNRAS*, 420:901–912. [4](#)
- Dwek, E. (1998). The Evolution of the Elemental Abundances in the Gas and Dust Phases of the Galaxy. *APJ*, 501:643. [59](#), [94](#)

- Dwek, E. and Arendt, R. G. (1992). Dust-gas interactions and the infrared emission from hot astrophysical plasmas. *ARAA*, 30:11–50. [60](#)
- Dwek, E., Galliano, F., and Jones, A. P. (2007). The Evolution of Dust in the Early Universe with Applications to the Galaxy SDSS J1148+5251. *APJ*, 662:927–939. [61](#)
- Dwek, E. and Scalo, J. M. (1980). The evolution of refractory interstellar grains in the solar neighborhood. *APJ*, 239:193–211. [60](#), [61](#)
- Dwek, E., Staguhn, J., Arendt, R. G., Kovacks, A., Su, T., and Benford, D. J. (2014). Dust Formation, Evolution, and Obscuration Effects in the Very High-redshift Universe. *APJ*, 788:L30. [61](#)
- Efstathiou, G. (1992). Suppressing the formation of dwarf galaxies via photoionization. *MNRAS*, 256:43P–47P. [20](#)
- Ellis, R. S., McLure, R. J., Dunlop, J. S., Robertson, B. E., Ono, Y., Schenker, M. A., Koekemoer, A., Bowler, R. A. A., Ouchi, M., Rogers, A. B., Curtis-Lake, E., Schneider, E., Charlot, S., Stark, D. P., Furlanetto, S. R., and Cirasuolo, M. (2013). The Abundance of Star-forming Galaxies in the Redshift Range 8.5-12: New Results from the 2012 Hubble Ultra Deep Field Campaign. *APJ*, 763:L7. [2](#)
- Ferrarotti, A. S. and Gail, H.-P. (2006). Composition and quantities of dust produced by AGB-stars and returned to the interstellar medium. *AAP*, 447:553–576. [62](#), [63](#), [75](#), [76](#), [117](#)
- Finkelstein, S. L., Papovich, C., Giavalisco, M., Reddy, N. A., Ferguson, H. C., Koekemoer, A. M., and Dickinson, M. (2010). On the Stellar Populations and Evolution of Star-forming Galaxies at $6.3 < z < 8.6$. *ApJ*, 719:1250–1273. [2](#), [3](#)
- Finkelstein, S. L., Papovich, C., Ryan, R. E., Pawlik, A. H., Dickinson, M., Ferguson, H. C., Finlator, K., Koekemoer, A. M., Giavalisco, M., Cooray, A., Dunlop, J. S., Faber, S. M., Grogin, N. A., Kocevski, D. D., and Newman, J. A. (2012a). CANDELS: The Contribution of the Observed Galaxy Population to Cosmic Reionization. *ApJ*, 758:93. [2](#)
- Finkelstein, S. L., Papovich, C., Salmon, B., Finlator, K., Dickinson, M., Ferguson, H. C., Giavalisco, M., Koekemoer, A. M., Reddy, N. A., Bassett, R., Conselice, C. J., Dunlop, J. S., Faber, S. M., Grogin, N. A., Hathi, N. P., Kocevski, D. D., Lai, K., Lee, K.-S.,

- McLure, R. J., Mobasher, B., and Newman, J. A. (2012b). Candelas: The Evolution of Galaxy Rest-frame Ultraviolet Colors from $z = 8$ to 4. *ApJ*, 756:164. [4](#)
- Finkelstein, S. L., Ryan, Jr., R. E., Papovich, C., Dickinson, M., Song, M., Somerville, R. S., Ferguson, H. C., Salmon, B., Giavalisco, M., Koekemoer, A. M., Ashby, M. L. N., Behroozi, P., Castellano, M., Dunlop, J. S., Faber, S. M., Fazio, G. G., Fontana, A., Grogin, N. A., Hathi, N., Jaacks, J., Kocevski, D. D., Livermore, R., McLure, R. J., Merlin, E., Mobasher, B., Newman, J. A., Rafelski, M., Tilvi, V., and Willner, S. P. (2015). The Evolution of the Galaxy Rest-frame Ultraviolet Luminosity Function over the First Two Billion Years. *ApJ*, 810:71. [xv](#), [2](#), [3](#), [44](#), [45](#), [46](#), [47](#), [48](#)
- Font, A. S., Bower, R. G., McCarthy, I. G., Benson, A. J., Frenk, C. S., Helly, J. C., Lacey, C. G., Baugh, C. M., and Cole, S. (2008). The colours of satellite galaxies in groups and clusters. *MNRAS*, 389:1619–1629. [8](#)
- Furlong, M., Bower, R. G., Theuns, T., Schaye, J., Crain, R. A., Schaller, M., Dalla Vecchia, C., Frenk, C. S., McCarthy, I. G., Helly, J., Jenkins, A., and Rosas-Guevara, Y. M. (2015). Evolution of galaxy stellar masses and star formation rates in the EAGLE simulations. *MNRAS*, 450:4486–4504. [6](#), [40](#)
- Fynbo, J. P. U., Prochaska, J. X., Sommer-Larsen, J., Dessauges-Zavadsky, M., and Møller, P. (2008). Reconciling the Metallicity Distributions of Gamma-Ray Burst, Damped Ly α , and Lyman Break Galaxies at $z = 3$. *APJ*, 683:321–328. [69](#)
- Gail, H. P. and Sedlmayr, E. (1987). Dust formation in stellar winds. III - Self-consistent models for dust-driven winds around C-stars. *AAP*, 171:197–204. [62](#)
- Gall, C., Andersen, A. C., and Hjorth, J. (2011). Genesis and evolution of dust in galaxies in the early Universe. I. Modelling dust evolution in starburst galaxies. *AAP*, 528:A13. [61](#)
- Gehrz, R. D. and Ney, E. P. (1990). Confirmation of Dust Condensation in the Ejecta of Supernova 1987a. *Proceedings of the National Academy of Science*, 87:4354–4357. [58](#)
- Gehrz, R. D., Truran, J. W., Williams, R. E., and Starrfield, S. (1998). Nucleosynthesis in Classical Novae and Its Contribution to the Interstellar Medium. *PASP*, 110:3–26. [59](#)
- Geisel, S. L., Kleinmann, D. E., and Low, F. J. (1970). Infrared Emission of Novae. *APJL*, 161:L101. [59](#)

- Geller, M. J. and Beers, T. C. (1982). Substructure within clusters of galaxies. *PASP*, 94:421–439. [12](#)
- Genel, S., Vogelsberger, M., Springel, V., Sijacki, D., Nelson, D., Snyder, G., Rodriguez-Gomez, V., Torrey, P., and Hernquist, L. (2014). Introducing the Illustris project: the evolution of galaxy populations across cosmic time. *MNRAS*, 445:175–200. [40](#)
- Girardi, L., Bressan, A., Bertelli, G., and Chiosi, C. (2000). Evolutionary tracks and isochrones for low- and intermediate-mass stars: From 0.15 to 7 M_{sun} , and from $Z=0.0004$ to 0.03. *AAPS*, 141:371–383. [29](#), [78](#)
- Gnedin, N. Y. (2000). Effect of Reionization on Structure Formation in the Universe. *APJ*, 542:535–541. [21](#)
- Gomez, H. L., Krause, O., Barlow, M. J., Swinyard, B. M., Owen, P. J., Clark, C. J. R., Matsuura, M., Gomez, E. L., Rho, J., Besel, M.-a., Bouwman, J., Gear, W. K., Henning, T., Ivison, R. J., Polehampton, E. T., and Sibthorpe, B. (2012). a Cool Dust Factory in the Crab Nebula: a Herschel Study of the Filaments. *ApJ*, 760(1):96. [61](#)
- González, V., Bouwens, R., Illingworth, G., Labbé, I., Oesch, P., Franx, M., and Magee, D. (2014). SLOW EVOLUTION OF THE SPECIFIC STAR FORMATION RATE AT $z > 2$: THE IMPACT OF DUST, EMISSION LINES, AND A RISING STAR FORMATION HISTORY. *ApJ*, 781(1):34. [8](#)
- González, V., Labbé, I., Bouwens, R. J., Illingworth, G., Franx, M., and Kriek, M. (2011). EVOLUTION OF GALAXY STELLAR MASS FUNCTIONS, MASS DENSITIES, AND MASS-TO-LIGHT RATIOS FROM $z = 7$ TO $z = 4$. *ApJ*, 735(2):L34. [xiv](#), [5](#), [37](#), [39](#)
- Greve, T. R., Bertoldi, F., Smail, I., Neri, R., Chapman, S. C., Blain, A. W., Ivison, R. J., Genzel, R., Omont, A., Cox, P., Tacconi, L., and Kneib, J.-P. (2005). An interferometric CO survey of luminous submillimetre galaxies. *MNRAS*, 359:1165–1183. [68](#)
- Guiderdoni, B. and Rocca-Volmerange, B. (1987). A model of spectrophotometric evolution for high-redshift galaxies. *AAP*, 186:1–21. [30](#)
- Guo, Q., White, S., Angulo, R. E., Henriques, B., Lemson, G., Boylan-Kolchin, M., Thomas, P., and Short, C. (2013). Galaxy formation in WMAP1 and WMAP7 cosmologies. *MNRAS*, 428:1351–1365. [8](#), [9](#)

- Guo, Q., White, S., Boylan-Kolchin, M., De Lucia, G., Kauffmann, G., Lemson, G., Li, C., Springel, V., and Weinmann, S. (2011). From dwarf spheroidals to cD galaxies: simulating the galaxy population in a Λ CDM cosmology. *MNRAS*, 413:101–131. [8](#), [9](#), [26](#), [27](#)
- Guo, Q. and White, S. D. M. (2009). High-redshift galaxy populations and their descendants. *MNRAS*, 396(1):39–52. [30](#), [43](#)
- Heinis, S., Buat, V., Béthermin, M., Aussel, H., Bock, J., Boselli, A., Burgarella, D., Conley, A., Cooray, A., Farrah, D., Ibar, E., Ilbert, O., Ivison, R. J., Magdis, G., Marsden, G., Oliver, S. J., Page, M. J., Rodighiero, G., Roehlly, Y., Schulz, B., Scott, D., Smith, A. J., Viero, M., Wang, L., and Zemcov, M. (2013). HERMES: unveiling obscured star formation - the far-infrared luminosity function of ultraviolet-selected galaxies at $z \sim 1.5$. *MNRAS*, 429:1113–1132. [xvi](#), [49](#), [50](#)
- Henriques, B. M. B., Thomas, P. A., Oliver, S., and Roseboom, I. (2009). Monte Carlo Markov Chain parameter estimation in semi-analytic models of galaxy formation. *MNRAS*, 396:535–547. [7](#)
- Henriques, B. M. B., White, S. D. M., Thomas, P. A., Angulo, R., Guo, Q., Lemson, G., Springel, V., and Overzier, R. (2015). Galaxy formation in the Planck cosmology - I. Matching the observed evolution of star formation rates, colours and stellar masses. *MNRAS*, 451:2663–2680. [8](#), [9](#), [12](#), [17](#), [31](#), [35](#), [54](#), [89](#)
- Henriques, B. M. B., White, S. D. M., Thomas, P. A., Angulo, R. E., Guo, Q., Lemson, G., and Springel, V. (2013). Simulations of the galaxy population constrained by observations from $z = 3$ to the present day: implications for galactic winds and the fate of their ejecta. *MNRAS*, 431:3373–3395. [8](#), [9](#), [40](#)
- Hoyle, F. and Wickramasinghe, N. C. (1970). Radio Waves from Grains in HII Regions. *NATURE*, 227:473–474. [58](#)
- Ilbert, O., McCracken, H. J., Le Fèvre, O., Capak, P., Dunlop, J., Karim, A., Renzini, M. A., Caputi, K., Boissier, S., Arnouts, S., Aussel, H., Comparat, J., Guo, Q., Hudelot, P., Kartaltepe, J., Kneib, J. P., Krogager, J. K., Le Floch, E., Lilly, S., Mellier, Y., Milvang-Jensen, B., Moutard, T., Onodera, M., Richard, J., Salvato, M., Sanders, D. B., Scoville, N., Silverman, J. D., Taniguchi, Y., Tasca, L., Thomas, R., Toft, S., Tresse, L., Vergani, D., Wolk, M., and Zirm, A. (2013). Mass assembly in quiescent and star-forming galaxies since $z \sim 4$ from UltraVISTA. *AAP*, 556:A55. [xiii](#), [33](#)

- Ilbert, O., Salvato, M., Le Floch, E., Aussel, H., Capak, P., McCracken, H. J., Mobasher, B., Kartaltepe, J., Scoville, N., Sanders, D. B., Arnouts, S., Bundy, K., Cassata, P., Kneib, J.-P., Koekemoer, A., Le Fèvre, O., Lilly, S., Surace, J., Taniguchi, Y., Tasca, L., Thompson, D., Tresse, L., Zamojski, M., Zamorani, G., and Zucca, E. (2010). Galaxy Stellar Mass Assembly Between $0.2 < z < 2$ from the S-COSMOS Survey. *ApJ*, 709:644–663. [xiii](#), [33](#)
- Jenkins, E. B. (2004). Evidence and Implications of Pressure Fluctuations in the ISM. *APSS*, 289:215–223. [60](#), [64](#)
- Jones, A. P., Tielens, A. G. G. M., and Hollenbach, D. J. (1996). Grain Shattering in Shocks: The Interstellar Grain Size Distribution. *APJ*, 469:740. [60](#), [64](#)
- Kampakoglou, M., Trotta, R., and Silk, J. (2008). Monolithic or hierarchical star formation? A new statistical analysis. *MNRAS*, 384:1414–1426. [7](#)
- Kanekar, N., Wagg, J., Chary, R. R., and Carilli, C. L. (2013). A Search for C II 158 μm Line Emission in HCM 6A, a Ly α Emitter at $z = 6.56$. *APJL*, 771:L20. [69](#)
- Kauffmann, G., Charlot, S., and White, S. D. M. (1996). Detection of strong evolution in the population of early-type galaxies. *MNRAS*, 283:L117–L122. [15](#)
- Kauffmann, G., Colberg, J. M., Diaferio, A., and White, S. D. M. (1999). Clustering of galaxies in a hierarchical universe - I. Methods and results at $z=0$. *MNRAS*, 303:188–206. [9](#), [15](#)
- Kauffmann, G., White, S. D. M., and Guiderdoni, B. (1993). The Formation and Evolution of Galaxies Within Merging Dark Matter Haloes. *MNRAS*, 264:201. [7](#)
- Kennicutt, Jr., R. C. (1998). The Global Schmidt Law in Star-forming Galaxies. *APJ*, 498:541–552. [15](#)
- Kitzbichler, M. G. and White, S. D. M. (2007). The high-redshift galaxy population in hierarchical galaxy formation models. *MNRAS*, 376(1):2–12. [30](#)
- Knebe, A., Pearce, F. R., Thomas, P. A., Benson, A., Blaizot, J., Bower, R., Carretero, J., Castander, F. J., Cattaneo, A., Cora, S. A., Croton, D. J., Cui, W., Cunnama, D., De Lucia, G., Devriendt, J. E., Elahi, P. J., Font, A., Fontanot, F., Garcia-Bellido, J., Gargiulo, I. D., Gonzalez-Perez, V., Helly, J., Henriques, B., Hirschmann, M., Lee, J., Mamon, G. A., Monaco, P., Onions, J., Padilla, N. D., Power, C., Pujol, A., Skibba,

- R. A., Somerville, R. S., Srisawat, C., Vega-Martínez, C. A., and Yi, S. K. (2015). nIFTy cosmology: comparison of galaxy formation models. *MNRAS*, 451:4029–4059. [8](#)
- Kong, X., Charlot, S., Brinchmann, J., and Fall, S. M. (2004). Star formation history and dust content of galaxies drawn from ultraviolet surveys. *MNRAS*, 349:769–778. [30](#)
- Kroupa, P. (2001). On the variation of the initial mass function. *MNRAS*, 322:231–246. [28](#)
- Krühler, T., Malesani, D., Fynbo, J. P. U., Hartoog, O. E., Hjorth, J., Jakobsson, P., Perley, D. A., Rossi, A., Schady, P., Schulze, S., Tanvir, N. R., Vergani, S. D., Wiersema, K., Afonso, P. M. J., Bolmer, J., Cano, Z., Covino, S., D’Elia, V., de Ugarte Postigo, A., Filgas, R., Friis, M., Graham, J. F., Greiner, J., Goldoni, P., Gomboc, A., Hammer, F., Japelj, J., Kann, D. A., Kaper, L., Klose, S., Levan, A. J., Leloudas, G., Milvang-Jensen, B., Nicuesa Guelbenzu, A., Palazzi, E., Pian, E., Piranomonte, S., Sánchez-Ramírez, R., Savaglio, S., Selsing, J., Tagliaferri, G., Vreeswijk, P. M., Watson, D. J., and Xu, D. (2015). GRB hosts through cosmic time. VLT/X-Shooter emission-line spectroscopy of 96 γ -ray-burst-selected galaxies at $0.1 < z < 3.6$. *AAP*, 581:A125. [69](#)
- Labbé, I., González, V., Bouwens, R. J., Illingworth, G. D., Oesch, P. A., van Dokkum, P. G., Carollo, C. M., Franx, M., Stiavelli, M., Trenti, M., Magee, D., and Kriek, M. (2010). Ultradeep Infrared Array Camera Observations of Sub- L_* $z = 7$ and $z = 8$ Galaxies in the Hubble Ultra Deep Field: the Contribution of Low-Luminosity Galaxies to the Stellar Mass Density and Reionization. *APJL*, 708:L26–L31. [5](#)
- Lacey, C. G., Baugh, C. M., Frenk, C. S., Benson, A. J., Bower, R. G., Cole, S., Gonzalez-Perez, V., Helly, J. C., Lagos, C. D. P., and Mitchell, P. D. (2016). A unified multi-wavelength model of galaxy formation. *MNRAS*, 462:3854–3911. [8](#)
- Larson, R. B. (1974). Effects of supernovae on the early evolution of galaxies. *MNRAS*, 169:229–246. [21](#)
- Lejeune, T., Cuisinier, F., and Buser, R. (1997). Standard stellar library for evolutionary synthesis. I. Calibration of theoretical spectra. *AAPS*, 125. [29](#)
- Li, C. and White, S. D. M. (2009). The distribution of stellar mass in the low-redshift Universe. *MNRAS*, 398:2177–2187. [xiii](#), [33](#)
- Lorenzoni, S., Bunker, A. J., Wilkins, S. M., Caruana, J., Stanway, E. R., and Jarvis,

- M. J. (2013). Constraining the bright-end of the UV luminosity function for $z \approx 7-9$ galaxies: results from CANDELS/GOODS-South. *MNRAS*, 429:150–158. [2](#)
- Lorenzoni, S., Bunker, A. J., Wilkins, S. M., Stanway, E. R., Jarvis, M. J., and Caruana, J. (2011). Star-forming galaxies at $z \approx 8-9$ from Hubble Space Telescope/WFC3: implications for reionization. *MNRAS*, 414:1455–1466. [2](#), [3](#)
- Magorrian, J., Tremaine, S., Richstone, D., Bender, R., Bower, G., Dressler, A., Faber, S. M., Gebhardt, K., Green, R., Grillmair, C., Kormendy, J., and Lauer, T. (1998). The Demography of Massive Dark Objects in Galaxy Centers. *AJ*, 115:2285–2305. [23](#)
- Maiolino, R., Carniani, S., Fontana, A., Vallini, L., Pentericci, L., Ferrara, A., Vanzella, E., Grazian, A., Gallerani, S., Castellano, M., Cristiani, S., Brammer, G., Santini, P., Wagg, J., and Williams, R. (2015). The assembly of normal galaxies at $z \sim 7$ probed by ALMA. *MNRAS*, 452:54–68. [69](#)
- Maiolino, R., Nagao, T., Grazian, A., Cocchia, F., Marconi, A., Mannucci, F., Cimatti, A., Pipino, A., Ballero, S., Calura, F., Chiappini, C., Fontana, A., Granato, G. L., Matteucci, F., Pastorini, G., Pentericci, L., Risaliti, G., Salvati, M., and Silva, L. (2008). AMAZE. I. The evolution of the mass-metallicity relation at $z > 3$. *AAP*, 488:463–479. [44](#)
- Maiolino, R., Schneider, R., Oliva, E., Bianchi, S., Ferrara, A., Mannucci, F., Pedani, M., and Roca Sogorb, M. (2004). A supernova origin for dust in a high-redshift quasar. *NATURE*, 431:533–535. [61](#)
- Mancini, M., Schneider, R., Graziani, L., Valiante, R., Dayal, P., Maio, U., Ciardi, B., and Hunt, L. K. (2015). The dust mass in $z > 6$ normal star-forming galaxies. *MNRAS*, 451:L70–L74. [61](#), [69](#)
- Mannucci, F., Salvaterra, R., and Campisi, M. A. (2011). The metallicity of the long GRB hosts and the fundamental metallicity relation of low-mass galaxies. *MNRAS*, 414:1263–1268. [69](#)
- Maoz, D., Sharon, K., and Gal-Yam, A. (2010). The Supernova Delay Time Distribution in Galaxy Clusters and Implications for Type-Ia Progenitors and Metal Enrichment. *APJ*, 722:1879–1894. [19](#)
- Maraston, C. (2005). Evolutionary population synthesis: models, analysis of the ingredients and application to high- z galaxies. *MNRAS*, 362:799–825. [29](#)

- Marchenko, S. V., Moffat, A. F. J., St-Louis, N., and Fullerton, A. W. (2006). The Origin of Structures in Wolf-Rayet Winds: FUSE Observations of WR 135. *APJ*, 639:L75–L78. [63](#)
- Marchesini, D., van Dokkum, P. G., Förster Schreiber, N. M., Franx, M., Labbé, I., and Wuyts, S. (2009). The Evolution of the Stellar Mass Function of Galaxies from $z = 4.0$ and the First Comprehensive Analysis of its Uncertainties: Evidence for Mass-Dependent Evolution. *ApJ*, 701:1765–1796. [xiii](#), [33](#)
- Marchesini, D., Whitaker, K. E., Brammer, G., van Dokkum, P. G., Labbé, I., Muzzin, A., Quadri, R. F., Kriek, M., Lee, K.-S., Rudnick, G., Franx, M., Illingworth, G. D., and Wake, D. (2010). The Most Massive Galaxies at $3.0 \leq z < 4.0$ in the Newfirm Medium-band Survey: Properties and Improved Constraints on the Stellar Mass Function. *ApJ*, 725:1277–1295. [xiii](#), [33](#)
- Marigo, P. (2001). Chemical yields from low- and intermediate-mass stars: Model predictions and basic observational constraints. *AAP*, 370:194–217. [xiii](#), [18](#), [19](#)
- Martindale, H., Thomas, P. A., Henriques, B. M., and Loveday, J. (2016). A consistent model for both the HI and stellar mass functions of galaxies. *ArXiv e-prints*. [80](#)
- Mathis, J. S., Mezger, P. G., and Panagia, N. (1983). Interstellar radiation field and dust temperatures in the diffuse interstellar matter and in giant molecular clouds. *AAP*, 128:212–229. [30](#)
- Mattsson, L. (2015). The sudden appearance of dust in the early Universe. *ArXiv e-prints*. [61](#), [62](#)
- Mattsson, L., De Cia, a., Andersen, a. C., and Zafar, T. (2014). On the (in)variance of the dust-to-metals ratio in galaxies. *MNRAS*, 440(2):1562–1570. [61](#)
- McKee, C. F. (1989). Photoionization-regulated star formation and the structure of molecular clouds. *APJ*, 345:782–801. [64](#), [80](#), [117](#)
- McLure, R. J., Dunlop, J. S., Bowler, R. A. A., Curtis-Lake, E., Schenker, M., Ellis, R. S., Robertson, B. E., Koekemoer, A. M., Rogers, A. B., Ono, Y., Ouchi, M., Charlot, S., Wild, V., Stark, D. P., Furlanetto, S. R., Cirasuolo, M., and Targett, T. A. (2013). A new multifield determination of the galaxy luminosity function at $z = 7-9$ incorporating the 2012 Hubble Ultra-Deep Field imaging. *MNRAS*, 432:2696–2716. [2](#), [3](#)

- McLure, R. J., Dunlop, J. S., Cirasuolo, M., Koekemoer, a. M., Sabbi, E., Stark, D. P., Targett, T. a., and Ellis, R. S. (2010). Galaxies at $z=6-9$ from the WFC3/IR imaging of the Hubble Ultra Deep Field. *MNRAS*, 403(2):960–983. [2](#)
- McLure, R. J., Dunlop, J. S., de Ravel, L., Cirasuolo, M., Ellis, R. S., Schenker, M., Robertson, B. E., Koekemoer, A. M., Stark, D. P., and Bowler, R. A. A. (2011). A robust sample of galaxies at redshifts $6.0 < z < 8.7$: stellar populations, star formation rates and stellar masses. *MNRAS*, 418:2074–2105. [2](#)
- Meurer, G. R., Heckman, T. M., and Calzetti, D. (1999). Dust Absorption and the Ultraviolet Luminosity Density at $z = 3$ as Calibrated by Local Starburst Galaxies. *APJ*, 521:64–80. [xvi](#), [4](#), [49](#), [50](#)
- Michałowski, M. J. (2015). Dust production 680-850 million years after the Big Bang. *AAP*, 577:A80. [61](#)
- Mihos, J. C. and Hernquist, L. (1996). Gasdynamics and Starbursts in Major Mergers. *APJ*, 464:641. [15](#)
- Mo, H. J., Mao, S., and White, S. D. M. (1998). The formation of galactic discs. *MNRAS*, 295:319–336. [15](#)
- Murray, N. and Rahman, M. (2010). Star Formation in Massive Clusters Via the Wilkinson Microwave Anisotropy Probe and the Spitzer Glimpse Survey. *APJ*, 709:424–435. [79](#)
- Muzzin, A., Marchesini, D., Stefanon, M., Franx, M., McCracken, H. J., Milvang-Jensen, B., Dunlop, J. S., Fynbo, J. P. U., Brammer, G., Labbé, I., and van Dokkum, P. G. (2013). The Evolution of the Stellar Mass Functions of Star-forming and Quiescent Galaxies to $z = 4$ from the COSMOS/UltraVISTA Survey. *ApJ*, 777:18. [xiii](#), [33](#)
- Obreschkow, D., Croton, D., De Lucia, G., Khochfar, S., and Rawlings, S. (2009). Simulation of the Cosmic Evolution of Atomic and Molecular Hydrogen in Galaxies. *APJ*, 698:1467–1484. [80](#)
- Oesch, P. a., Bouwens, R. J., Illingworth, G. D., Carollo, C. M., Franx, M., Labbé, I., Magee, D., Stiavelli, M., Trenti, M., and van Dokkum, P. G. (2010). $z = 7$ GALAXIES IN THE HUDF: FIRST EPOCH WFC3/IR RESULTS. *ApJ*, 709(1):L16–L20. [2](#), [3](#)
- Oesch, P. A., Bouwens, R. J., Illingworth, G. D., Labbé, I., Trenti, M., Gonzalez, V., Carollo, C. M., Franx, M., van Dokkum, P. G., and Magee, D. (2012). Expanded

Search for $z = 10$ Galaxies from HUDF09, ERS, and CANDELS Data: Evidence for Accelerated Evolution at $z > 8$? *ApJ*, 745:110. [2](#)

Oesch, P. A., Brammer, G., van Dokkum, P. G., Illingworth, G. D., Bouwens, R. J., Labbé, I., Franx, M., Momcheva, I., Ashby, M. L. N., Fazio, G. G., Gonzalez, V., Holden, B., Magee, D., Skelton, R. E., Smit, R., Spitler, L. R., Trenti, M., and Willner, S. P. (2016). A Remarkably Luminous Galaxy at $z=11.1$ Measured with Hubble Space Telescope Grism Spectroscopy. *ApJ*, 819:129. [4](#)

Oesch, P. A., Carollo, C. M., Stiavelli, M., Trenti, M., Bergeron, L. E., Koekemoer, A. M., Lucas, R. A., Pavlovsky, C. M., Beckwith, S. V. W., Dahlen, T., Ferguson, H. C., Gardner, J. P., Lilly, S. J., Mobasher, B., and Panagia, N. (2009). The UDF05 Follow-Up of the Hubble Ultra Deep Field. II. Constraints on Reionization from Z-Dropout Galaxies. *ApJ*, 690:1350–1357. [3](#)

Okamoto, T., Gao, L., and Theuns, T. (2008). Mass loss of galaxies due to an ultraviolet background. *MNRAS*, 390:920–928. [21](#)

Ota, K., Walter, F., Ohta, K., Hatsukade, B., Carilli, C. L., da Cunha, E., González-López, J., Decarli, R., Hodge, J. A., Nagai, H., Egami, E., Jiang, L., Iye, M., Kashikawa, N., Riechers, D. A., Bertoldi, F., Cox, P., Neri, R., and Weiss, A. (2014). ALMA Observation of $158 \mu\text{m}$ [C II] Line and Dust Continuum of a $z = 7$ Normally Star-forming Galaxy in the Epoch of Reionization. *APJ*, 792:34. [69](#)

Oteo, I., Ivison, R. J., Dunne, L., Smail, I., Swinbank, A. M., Zhang, Z.-Y., Lewis, A., Maddox, S., Riechers, D., Serjeant, S., Van der Werf, P., Biggs, A. D., Bremer, M., Cigan, P., Clements, D. L., Cooray, A., Dannerbauer, H., Eales, S., Ibar, E., Messias, H., Michałowski, M. J., Pérez-Fournon, I., and van Kampen, E. (2016). Witnessing the Birth of the Red Sequence: ALMA High-resolution Imaging of [C II] and Dust in Two Interacting Ultra-red Starbursts at $z = 4.425$. *ApJ*, 827:34. [4](#)

Ouchi, M., Ellis, R., Ono, Y., Nakanishi, K., Kohno, K., Momose, R., Kurono, Y., Ashby, M. L. N., Shimasaku, K., Willner, S. P., Fazio, G. G., Tamura, Y., and Iono, D. (2013). An Intensely Star-forming Galaxy at $z = 7$ with Low Dust and Metal Content Revealed by Deep ALMA and HST Observations. *APJ*, 778:102. [61](#), [69](#)

Ouchi, M., Mobasher, B., Shimasaku, K., Ferguson, H. C., Fall, S. M., Ono, Y., Kashikawa, N., Morokuma, T., Nakajima, K., Okamura, S., Dickinson, M., Giavalisco, M., and Ohta,

- K. (2009). Large Area Survey for $z = 7$ Galaxies in SDF and GOODS-N: Implications for Galaxy Formation and Cosmic Reionization. *ApJ*, 706:1136–1151. [3](#)
- Overzier, R., Lemson, G., Angulo, R. E., Bertin, E., Blaizot, J., Henriques, B. M. B., Marleau, G.-D., and White, S. D. M. (2013). The Millennium Run Observatory: first light. *MNRAS*, 428:778–803. [31](#)
- Pavesi, R., Riechers, D. A., Capak, P. L., Carilli, C. L., Sharon, C. E., Stacey, G. J., Karim, A., Scoville, N. Z., and Smolčić, V. (2016). ALMA Reveals Weak [N ii] Emission in “Typical” Galaxies and Intense Starbursts at $z = 5-6$. *ApJ*, 832:151. [3](#)
- Planck Collaboration, Ade, P. A. R., Aghanim, N., Alves, M. I. R., Armitage-Caplan, C., Arnaud, M., Ashdown, M., Atrio-Barandela, F., Aumont, J., Aussel, H., and et al. (2014). Planck 2013 results. I. Overview of products and scientific results. *A&A*, 571:A1. [8](#)
- Popping, G., Somerville, R. S., and Galametz, M. (2016). The dust content of galaxies from $z = 0$ to $z = 9$. *ArXiv e-prints*. [69](#), [94](#), [117](#)
- Portinari, L., Chiosi, C., and Bressan, A. (1998). Galactic chemical enrichment with new metallicity dependent stellar yields. *AAP*, 334:505–539. [xii](#), [xiii](#), [17](#), [18](#), [19](#), [75](#), [78](#)
- Press, W. H. and Schechter, P. (1974). Formation of Galaxies and Clusters of Galaxies by Self-Similar Gravitational Condensation. *ApJ*, 187:425–438. [6](#)
- Quadri, R. F., Williams, R. J., Lee, K.-S., Franx, M., van Dokkum, P., and Brammer, G. B. (2008). A Confirmation of the Strong Clustering of Distant Red Galaxies at $2 < z < 3$. *APJ*, 685:L1. [30](#)
- Rémy-Ruyer, A., Madden, S. C., Galliano, F., Lebouteiller, V., Baes, M., Bendo, G. J., Boselli, A., Ciesla, L., Cormier, D., Cooray, A., Cortese, L., De Looze, I., Doublier-Pritchard, V., Galametz, M., Jones, A. P., Karczewski, O. L., Lu, N., and Spinoglio, L. (2015). Linking dust emission to fundamental properties in galaxies: the low-metallicity picture. *AAP*, 582:A121. [xvii](#), [xviii](#), [xix](#), [68](#), [88](#), [89](#), [90](#), [104](#), [105](#), [106](#), [107](#), [108](#), [109](#), [110](#), [111](#)
- Riechers, D. a., Bradford, C. M., Clements, D. L., Dowell, C. D., Pérez-Fournon, I., Ivison, R. J., Bridge, C., Conley, a., Fu, H., Vieira, J. D., Wardlow, J., Calanog, J., Cooray, a., Hurley, P., Neri, R., Kamenetzky, J., Aguirre, J. E., Altieri, B., Arumugam, V., Benford, D. J., Béthermin, M., Bock, J., Burgarella, D., Cabrera-Lavers, a., Chapman,

- S. C., Cox, P., Dunlop, J. S., Earle, L., Farrah, D., Ferrero, P., Franceschini, a., Gavazzi, R., Glenn, J., Solares, E. a. G., Gurwell, M. a., Halpern, M., Hatziminaoglou, E., Hyde, a., Ibar, E., Kovács, a., Krips, M., Lupu, R. E., Maloney, P. R., Martinez-Navajas, P., Matsuhara, H., Murphy, E. J., Naylor, B. J., Nguyen, H. T., Oliver, S. J., Omont, a., Page, M. J., Petitpas, G., Rangwala, N., Roseboom, I. G., Scott, D., Smith, a. J., Staguhn, J. G., Streblyanska, a., Thomson, a. P., Valtchanov, I., Viero, M., Wang, L., Zemcov, M., and Zmuidzinas, J. (2013). A dust-obscured massive maximum-starburst galaxy at a redshift of 6.34. *Nature*, 496(7445):329–33. [3](#), [48](#), [61](#)
- Robertson, B. E., Ellis, R. S., Dunlop, J. S., McLure, R. J., and Stark, D. P. (2010). Early star-forming galaxies and the reionization of the Universe. *Nature*, 468:49–55. [3](#)
- Rogers, A. B., McLure, R. J., and Dunlop, J. S. (2013). The unbiased measurement of ultraviolet spectral slopes in low-luminosity galaxies at $z \approx 7$. *MNRAS*, 429:2456–2468. [4](#)
- Rowlands, K., Gomez, H. L., Dunne, L., Aragón-Salamanca, A., Dye, S., Maddox, S., da Cunha, E., and van der Werf, P. (2014). The dust budget crisis in high-redshift submillimetre galaxies. *MNRAS*, 441:1040–1058. [61](#)
- Salmon, B., Papovich, C., Finkelstein, S. L., Tilvi, V., Finlator, K., Behroozi, P., Dahlen, T., Davé, R., Dekel, A., Dickinson, M., Ferguson, H. C., Giavalisco, M., Long, J., Lu, Y., Mobasher, B., Reddy, N., Somerville, R. S., and Wechsler, R. H. (2015). The Relation between Star Formation Rate and Stellar Mass for Galaxies at $3.5 < z < 6.5$ in CANDELS. *ApJ*, 799:183. [xiv](#), [40](#), [41](#)
- Salpeter, E. E. (1955). The Luminosity Function and Stellar Evolution. *APJ*, 121:161. [28](#)
- Santini, P., Maiolino, R., Magnelli, B., Lutz, D., Lamastra, A., Li Causi, G., Eales, S., Andreani, P., Berta, S., Buat, V., Cooray, A., Cresci, G., Daddi, E., Farrah, D., Fontana, A., Franceschini, A., Genzel, R., Granato, G., Grazian, A., Le Floc’h, E., Magdis, G., Magliocchetti, M., Mannucci, F., Menci, N., Nordon, R., Oliver, S., Popesso, P., Pozzi, F., Riguccini, L., Rodighiero, G., Rosario, D. J., Salvato, M., Scott, D., Silva, L., Tacconi, L., Viero, M., Wang, L., Wuyts, S., and Xu, K. (2014). The evolution of the dust and gas content in galaxies. *AAP*, 562:A30. [xvii](#), [xviii](#), [68](#), [69](#), [88](#), [89](#), [90](#), [105](#), [115](#)
- Savage, B. D. and Sembach, K. R. (1996). Interstellar Gas-Phase Abundances and Physical Conditions toward Two Distant High-Latitude Halo Stars. *APJ*, 470:893. [60](#)

- Schaerer, D., Boone, F., Zamojski, M., Staguhn, J., Dessauges-Zavadsky, M., Finkelstein, S., and Combes, F. (2015). New constraints on dust emission and UV attenuation of $z = 6.5-7.5$ galaxies from millimeter observations. *AAP*, 574:A19. [69](#)
- Schaye, J., Crain, R. A., Bower, R. G., Furlong, M., Schaller, M., Theuns, T., Dalla Vecchia, C., Frenk, C. S., McCarthy, I. G., Helly, J. C., Jenkins, A., Rosas-Guevara, Y. M., White, S. D. M., Baes, M., Booth, C. M., Camps, P., Navarro, J. F., Qu, Y., Rahmati, A., Sawala, T., Thomas, P. A., and Trayford, J. (2015). The EAGLE project: simulating the evolution and assembly of galaxies and their environments. *MNRAS*, 446:521–554. [6](#), [40](#)
- Schreiber, S. J. (2017). A dynamical trichotomy for structured populations experiencing positive density-dependence in stochastic environments. *ArXiv e-prints*. [4](#)
- Scott, K. S., Lupu, R. E., Aguirre, J. E., Auld, R., Aussel, H., Baker, A. J., Beelen, A., Bock, J., Bradford, C. M., Brisbin, D., Burgarella, D., Carpenter, J. M., Chanical, P., Chapman, S. C., Clements, D. L., Conley, A., Cooray, A., Cox, P., Dowell, C. D., Eales, S., Farrah, D., Franceschini, A., Frayer, D. T., Gavazzi, R., Glenn, J., Griffin, M., Harris, A. I., Ibar, E., Ivison, R. J., Kamenetzky, J., Kim, S., Krips, M., Maloney, P. R., Matsuhara, H., Mortier, A. M. J., Murphy, E. J., Naylor, B. J., Neri, R., Nguyen, H. T., Oliver, S. J., Omont, A., Page, M. J., Papageorgiou, A., Pearson, C. P., Pérez-Fournon, I., Pohlen, M., Rawlings, J. I., Raymond, G., Riechers, D., Rodighiero, G., Roseboom, I. G., Rowan-Robinson, M., Scott, D., Seymour, N., Smith, A. J., Symeonidis, M., Tugwell, K. E., Vaccari, M., Vieira, J. D., Vigroux, L., Wang, L., Wright, G., and Zmuidzinas, J. (2011). Redshift Determination and CO Line Excitation Modelling for the Multiply Lensed Galaxy HLSW-01. *APJ*, 733:29. [68](#)
- Seab, C. G. (1987). Grain destruction, formation, and evolution. In Hollenbach, D. J. and Thronson, Jr., H. A., editors, *Interstellar Processes*, volume 134 of *Astrophysics and Space Science Library*, pages 491–512. [64](#)
- Sedlmayr, E. (1989). Dust Condensation in Stellar Outflows. In Allamandola, L. J. and Tielens, A. G. G. M., editors, *Interstellar Dust*, volume 135 of *IAU Symposium*, page 467. [59](#)
- Shamshiri, S., Thomas, P. A., Henriques, B. M., Tojeiro, R., Lemson, G., Oliver, S. J., and Wilkins, S. (2015). Galaxy formation in the Planck cosmology - II. Star-formation

- histories and post-processing magnitude reconstruction. *MNRAS*, 451:2681–2691. [16](#), [35](#)
- Shu, X. W., Elbaz, D., Bourne, N., Schreiber, C., Wang, T., Dunlop, J. S., Fontana, A., Leiton, R., Pannella, M., Okumura, K., Michałowski, M. J., Santini, P., Merlin, E., Buitrago, F., Bruce, V. A., Amorin, R., Castellano, M., Derriere, S., Comastri, A., Cappelluti, N., Wang, J. X., and Ferguson, H. C. (2016). Identification of $z > 2$ Herschel 500 μM Sources Using Color Deconfusion. *APJS*, 222:4. [3](#)
- Shull, J. M. (1978). Disruption and sputtering of grains in intermediate-velocity interstellar clouds. *APJ*, 226:858–862. [60](#)
- Silk, J. and Mamon, G. A. (2012). The current status of galaxy formation. *Research in Astronomy and Astrophysics*, 12:917–946. [xiii](#), [20](#), [21](#)
- Smit, R., Bouwens, R. J., Franx, M., Illingworth, G. D., Labbé, I., Oesch, P. a., and van Dokkum, P. G. (2012). THE STAR FORMATION RATE FUNCTION FOR REDSHIFT $z = 4-7$ GALAXIES: EVIDENCE FOR A UNIFORM BUILDUP OF STAR-FORMING GALAXIES DURING THE FIRST 3 Gyr OF COSMIC TIME. *ApJ*, 756(1):14. [xiv](#), [4](#), [36](#), [38](#)
- Smit, R., Bouwens, R. J., Franx, M., Oesch, P. A., Ashby, M. L. N., Willner, S. P., Labbé, I., Holwerda, B., Fazio, G. G., and Huang, J.-S. (2015). High-precision Photometric Redshifts from Spitzer/IRAC: Extreme [3.6] - [4.5] Colors Identify Galaxies in the Redshift Range $z \sim 6.6 - 6.9$. *APJ*, 801:122. [xvi](#), [50](#)
- Smit, R., Bouwens, R. J., Labbé, I., Zheng, W., Bradley, L., Donahue, M., Lemze, D., Moustakas, J., Umetsu, K., Zitrin, A., Coe, D., Postman, M., Gonzalez, V., Bartelmann, M., Benítez, N., Broadhurst, T., Ford, H., Grillo, C., Infante, L., Jimenez-Teja, Y., Jouvel, S., Kelson, D. D., Lahav, O., Maoz, D., Medezinski, E., Melchior, P., Meneghetti, M., Merten, J., Molino, A., Moustakas, L. A., Nonino, M., Rosati, P., and Seitz, S. (2014). Evidence for Ubiquitous High-equivalent-width Nebular Emission in $z = 7$ Galaxies: Toward a Clean Measurement of the Specific Star-formation Rate Using a Sample of Bright, Magnified Galaxies. *ApJ*, 784:58. [37](#)
- Smith, N. and Owocki, S. P. (2006). On the Role of Continuum-driven Eruptions in the Evolution of Very Massive Stars and Population III Stars. *APJL*, 645:L45–L48. [63](#)
- Somerville, R. S., Gilmore, R. C., Primack, J. R., and Domínguez, A. (2012). Galaxy

- properties from the ultraviolet to the far-infrared: A cold dark matter models confront observations. *MNRAS*, 423:1992–2015. [8](#)
- Somerville, R. S., Hopkins, P. F., Cox, T. J., Robertson, B. E., and Hernquist, L. (2008). A semi-analytic model for the co-evolution of galaxies, black holes and active galactic nuclei. *MNRAS*, 391:481–506. [8](#)
- Somerville, R. S., Lemson, G., Sigad, Y., Dekel, A., Kauffmann, G., and White, S. D. M. (2001). Non-linear stochastic galaxy biasing in cosmological simulations. *MNRAS*, 320:289–306. [15](#)
- Somerville, R. S. and Primack, J. R. (1999). Semi-analytic modelling of galaxy formation: the local Universe. *MNRAS*, 310:1087–1110. [8](#), [117](#)
- Spiegel, D. N., Verde, L., Peiris, H. V., Komatsu, E., Nolte, M. R., Bennett, C. L., Halpern, M., Hinshaw, G., Jarosik, N., Kogut, A., Limon, M., Meyer, S. S., Page, L., Tucker, G. S., Weiland, J. L., Wollack, E., and Wright, E. L. (2003). First-Year Wilkinson Microwave Anisotropy Probe (WMAP) Observations: Determination of Cosmological Parameters. *ApJ*, 148:175–194. [12](#)
- Spitzer, Jr., L. and Morton, W. A. (1976). Components in interstellar molecular hydrogen. *APJ*, 204:731–749. [60](#)
- Springel, V., White, S. D. M., Jenkins, A., Frenk, C. S., Yoshida, N., Gao, L., Navarro, J., Thacker, R., Croton, D., Helly, J., Peacock, J. A., Cole, S., Thomas, P., Couchman, H., Evrard, A., Colberg, J., and Pearce, F. (2005). Simulations of the formation, evolution and clustering of galaxies and quasars. *Nature*, 435:629–636. [6](#), [8](#), [9](#), [10](#), [11](#)
- Springel, V., White, S. D. M., Tormen, G., and Kauffmann, G. (2001). Populating a cluster of galaxies - I. Results at $z=0$. *MNRAS*, 328:726–750. [8](#), [9](#), [12](#)
- Stanway, E. R., McMahon, R. G., and Bunker, A. J. (2005). Near-infrared properties of i-drop galaxies in the Hubble Ultra Deep Field. *MNRAS*, 359:1184–1192. [4](#)
- Stark, D. P., Ellis, R. S., Bunker, A., Bundy, K., Targett, T., Benson, A., and Lacy, M. (2009). the Evolutionary History of Lyman Break Galaxies Between Redshift 4 and 6: Observing Successive Generations of Massive Galaxies in Formation. *ApJ*, 697(2):1493–1511. [5](#)

- Steidel, C. C., Shapley, A. E., Pettini, M., Adelberger, K. L., Erb, D. K., Reddy, N. A., and Hunt, M. P. (2004). A Survey of Star-forming Galaxies in the $1.4 < Z < 2.5$ Redshift Desert: Overview. *APJ*, 604:534–550. [30](#)
- Sugerman, B. E. K., Ercolano, B., Barlow, M. J., Tielens, A. G. G. M., Clayton, G. C., Zijlstra, A. A., Meixner, M., Speck, A., Gledhill, T. M., Panagia, N., Cohen, M., Gordon, K. D., Meyer, M., Fabbri, J., Bowey, J. E., Welch, D. L., Regan, M. W., and Kennicutt, R. C. (2006). Massive-Star Supernovae as Major Dust Factories. *Science*, 313:196–200. [61](#)
- Sutherland, R. S. and Dopita, M. A. (1993). Cooling functions for low-density astrophysical plasmas. *APJs*, 88:253–327. [13](#)
- Tacconi, L. J., Neri, R., Chapman, S. C., Genzel, R., Smail, I., Ivison, R. J., Bertoldi, F., Blain, A., Cox, P., Greve, T., and Omont, A. (2006). High-Resolution Millimeter Imaging of Submillimeter Galaxies. *APJ*, 640:228–240. [68](#)
- Thielemann, F.-K., Argast, D., Brachwitz, F., Hix, W. R., Höflich, P., Liebendörfer, M., Martinez-Pinedo, G., Mezzacappa, A., Panov, I., and Rauscher, T. (2003). Nuclear cross sections, nuclear structure and stellar nucleosynthesis. *Nuclear Physics A*, 718:139–146. [xiii](#), [18](#), [19](#)
- Tinsley, B. M. (1980). Relations between nucleosynthesis rates and the metal abundance. *AAP*, 89:246–248. [17](#)
- Tomczak, A. R., Quadri, R. F., Tran, K.-V. H., Labbé, I., Straatman, C. M. S., Papovich, C., Glazebrook, K., Allen, R., Brammer, G. B., Kacprzak, G. G., Kawinwanichakij, L., Kelson, D. D., McCarthy, P. J., Mehtens, N., Monson, A. J., Persson, S. E., Spitler, L. R., Tilvi, V., and van Dokkum, P. (2014). Galaxy Stellar Mass Functions from ZFOURGE/CANDELS: An Excess of Low-mass Galaxies since $z = 2$ and the Rapid Buildup of Quiescent Galaxies. *ApJ*, 783:85. [xiii](#), [33](#)
- Trakhtenbrot, B., Lira, P., Netzer, H., Cicone, C., Maiolino, R., and Shemmer, O. (2017). ALMA Observations Show Major Mergers Among the Host Galaxies of Fast-growing, High-redshift#8203 Supermassive#8203 Black Holes. *ApJ*, 836:8. [3](#)
- Trumpler, R. J. (1930). Absorption of Light in the Galactic System. *PASP*, 42:214. [58](#)
- Valiante, R., Schneider, R., Bianchi, S., and Andersen, A. C. (2009). Stellar sources of dust in the high-redshift Universe. *MNRAS*, 397:1661–1671. [59](#)

- Valiante, R., Schneider, R., Salvadori, S., and Bianchi, S. (2011). The origin of the dust in high-redshift quasars: the case of SDSS J1148+5251. *MNRAS*, 416:1916–1935. [61](#)
- van der Hucht, K. A. (2006). New Galactic Wolf-Rayet stars, and candidates. An annex to The VIIth Catalogue of Galactic Wolf-Rayet Stars. *AAP*, 458:453–459. [63](#)
- Vlahakis, C., Dunne, L., and Eales, S. (2005). The SCUBA Local Universe Galaxy Survey - III. Dust along the Hubble sequence. *MNRAS*, 364:1253–1285. [xx](#), [115](#), [118](#)
- Vogelsberger, M., Genel, S., Springel, V., Torrey, P., Sijacki, D., Xu, D., Snyder, G., Bird, S., Nelson, D., and Hernquist, L. (2014). Properties of galaxies reproduced by a hydrodynamic simulation. *Nature*, 509:177–182. [6](#), [40](#)
- Wang, Y. and Mukherjee, P. (2006). Robust Dark Energy Constraints from Supernovae, Galaxy Clustering, and 3 yr Wilkinson Microwave Anisotropy Probe Observations. *APJ*, 650:1–6. [59](#)
- Watson, D., Christensen, L., Knudsen, K. K., Richard, J., Gallazzi, A., and Michałowski, M. J. (2015). A dusty, normal galaxy in the epoch of reionization. *NATURE*, 519:327–330. [69](#)
- White, S. D. M. and Frenk, C. S. (1991). Galaxy formation through hierarchical clustering. *APJ*, 379:52–79. [13](#)
- White, S. D. M. and Rees, M. J. (1978). Core condensation in heavy halos - A two-stage theory for galaxy formation and clustering. *MNRAS*, 183:341–358. [7](#), [21](#)
- Wilkins, S. M., Bouwens, R. J., Oesch, P. A., Labbé, I., Sargent, M., Caruana, J., Wardlow, J., and Clay, S. (2016). Quantifying the UV-continuum slopes of galaxies to $z \sim 10$ using deep Hubble+Spitzer/IRAC observations. *MNRAS*, 455:659–667. [4](#)
- Wilkins, S. M., Bunker, A., Coulton, W., Croft, R., Matteo, T. D., Khandai, N., and Feng, Y. (2013a). Interpreting the observed UV continuum slopes of high-redshift galaxies. *MNRAS*, 430:2885–2890. [xvi](#), [4](#), [5](#), [37](#), [49](#), [50](#)
- Wilkins, S. M., Bunker, A. J., Ellis, R. S., Stark, D., Stanway, E. R., Chiu, K., Lorenzoni, S., and Jarvis, M. J. (2010). Probing L_* Lyman-break galaxies at $z = 7$ in GOODS-South with WFC3 on Hubble Space Telescope. *MNRAS*, 403:938–944. [2](#)
- Wilkins, S. M., Bunker, A. J., Lorenzoni, S., and Caruana, J. (2011a). New star-forming galaxies at $z \approx 7$ from Wide Field Camera Three imaging. *MNRAS*, 411:23–36. [2](#)

- Wilkins, S. M., Bunker, A. J., Stanway, E., Lorenzoni, S., and Caruana, J. (2011b). The ultraviolet properties of star-forming galaxies - I. HST WFC3 observations of very high redshift galaxies. *MNRAS*, 417:717–729. [3](#), [4](#)
- Wilkins, S. M., Coulton, W., Caruana, J., Croft, R., Matteo, T. D., Khandai, N., Feng, Y., Bunker, A., and Elbert, H. (2013b). Theoretical predictions for the effect of nebular emission on the broad-band photometry of high-redshift galaxies. *MNRAS*, 435:2885–2895. [xvi](#), [49](#), [50](#)
- Wilkins, S. M., Gonzalez-Perez, V., Lacey, C. G., and Baugh, C. M. (2012). Predictions for the intrinsic UV continuum properties of star-forming galaxies and the implications for inferring dust extinction. *MNRAS*, 424:1522–1529. [3](#), [4](#)
- Williams, P. M., van der Hucht, K. A., and The, P. S. (1987). Variable dust emission from Wolf-Rayet stars. *QJRAS*, 28:248–253. [59](#)
- Wiseman, P., Schady, P., Bolmer, J., Krühler, T., Yates, R. M., Greiner, J., and Fynbo, J. P. U. (2017). Evolution of the dust-to-metals ratio in high-redshift galaxies probed by GRB-DLAs. *AAP*, 599:A24. [69](#), [110](#)
- Yan, H., Finkelstein, S. L., Huang, K.-H., Ryan, R. E., Ferguson, H. C., Koekemoer, A. M., Grogin, N. A., Dickinson, M., Newman, J. A., Somerville, R. S., Davé, R., Faber, S. M., Papovich, C., Guo, Y., Giavalisco, M., Lee, K.-s., Reddy, N., Cooray, A. R., Siana, B. D., Hathi, N. P., Fazio, G. G., Ashby, M., Weiner, B. J., Lucas, R. A., Dekel, A., Pentericci, L., Conselice, C. J., Kocevski, D. D., and Lai, K. (2012). Luminous and High Stellar Mass Candidate Galaxies at $z = 8$ Discovered in the Cosmic Assembly Near-Infrared Deep Extragalactic Legacy Survey. *ApJ*, 761:177. [5](#)
- Yates, R. M., Henriques, B., Thomas, P. A., Kauffmann, G., Johansson, J., and White, S. D. M. (2013). Modelling element abundances in semi-analytic models of galaxy formation. *MNRAS*, 435:3500–3520. [xii](#), [xiii](#), [9](#), [16](#), [17](#), [19](#), [20](#), [22](#), [48](#), [55](#), [58](#), [73](#)
- Yates, R. M., Kauffmann, G., and Guo, Q. (2012). The relation between metallicity, stellar mass and star formation in galaxies: an analysis of observational and model data. *MNRAS*, 422:215–231. [xiii](#), [20](#)
- Zhukovska, S. (2014). Dust origin in late-type dwarf galaxies: ISM growth vs. type II supernovae. *AAP*, 562:A76. [61](#), [78](#), [79](#)

Zhukovska, S., Gail, H.-P., and Trieloff, M. (2008). Evolution of interstellar dust and stardust in the solar neighbourhood. *AAP*, 479:453–480. [60](#), [61](#), [63](#), [67](#), [72](#), [77](#), [78](#), [94](#), [117](#)

Zubko, V., Dwek, E., and Arendt, R. G. (2004). Interstellar Dust Models Consistent with Extinction, Emission, and Abundance Constraints. *APJS*, 152:211–249. [68](#)